NORTHWESTERN UNIVERSITY

Effects Of Divalent Ions On Langmuir Monolayers: Synchrotron X-ray Scattering Studies

A DISSERTATION

SUBMITTED TO THE GRADUATE SCHOOL
IN PARTIAL FULFILLMENT OF THE REQUIREMENTS

for the degree

DOCTOR OF PHILOSOPHY

Field of Physics and Astronomy

By

Jan Kmetko

EVANSTON, ILLINOIS

December 2002

ABSTRACT

Effects Of Divalent Ions On Langmuir Monolayers:
Synchrotron X-ray Scattering Studies

Jan Kmetko

Thin films of organic molecules floating on aqueous substrates, when transferred onto solid substrates, can be potentially used in optoelectronics, molecular electronics, and biosensors. They can also be used as molecular templates for controlled nucleation of inorganic compounds (a model biomineralization process). These (and other) practical applications almost always involve preparation of Langmuir monolayers on salt solutions. Although structures of Langmuir monolayers on *pure* water have been well-characterized, only little is known about the effects of even the simplest metal salts on the crystalline structure of these monolayers. We have used grazing incidence synchrotron x-ray diffraction to study how the structure of fatty acid monolayers is affected by 1) alkaline water (no divalent ions), 2) dilute solutions of divalent salts and 3) supersaturated solutions of divalent salts.

Our results show that dilute solutions of both mono- and divalent ions change the structure of the Langmuir monolayer, but in different ways. Increasing pH in the subphase (and thus adding a monovalent ion) causes the monolayer to become more disordered. On the other hand, dissolving divalent metal salts (and raising pH) has the opposite effect: the monolayer becomes better ordered. All divalent ions effectively compress the monolayer into a tightly packed, untilted structure. Furthermore, some ions interact with the headgroups so strongly that the organic film buckles, with a periodic out-of-plane (superlattice) density modulation.

In supersaturated solutions, inorganic crystals begin to grow at the organic template (model biomineralization). Our studies reveal that barium and strontium fluoride grow preferentially oriented to the surface of the Langmuir monolayer. Barium fluoride has a contracted unit-cell at the initial stage of growth, and the organic molecules rearrange in such a way that the interfacial lattices are commensurate. Such registry at an organic-inorganic interface has long been suspected, and now has been directly confirmed. The concept of organic-inorganic structural matching plays an important precursor role in controlled biomineralization and organic-matrix-mediated materials synthesis.

Acknowledgements

I am grateful to those who collaborated with me on the experiments, for their work, help, discussions and encouragements. Many thanks to my advisor and mentor, Professor Pulak Dutta, for his guidance and infinite patience, and to my colleagues, Alokmay Datta, for being a role model and a source of intellectual inspiration, Chungjong Yu, Guennadi Evmenenko, Andrew Richter and Sumit Kewalramani, for taking night shifts and providing constructive feedback. Grateful acknowledgement is made to the scientists and staff at synchrotron beamlines, Nadia Leyarovska, Jianming Bai, Jin Wang, Suresh Narayanan, Peter Lee and Holger Tostmann for helping make the perfect beam every time. Special thanks to Linda Wildey and Michael Sarmiento, for being wonderful friends and providing a constant stream of moral support. I am most indebted to my family, and especially to my parents, Jan Kmetko and Maria Kmetkova, for their understanding, for their unselfish love, for taking the risk of sending their son on his quest and allowing him to pursue his dream. To them I dedicate this thesis with great love.

Contents

List of Tables

List of Figures

Introduction

Thin organic films on aqueous substrates (*Langmuir films*) are used in many applications: 1) they are precursors to films on solid substrates (*Langmuir-Blodgett films* or *LB films*); 2) they serve as theoretical models of two-dimensional systems; and 3) they control oriented growth of minerals from aqueous salts, a model biomineralization process. Often, these and other practical applications involve incorporation of non-organic complexes into the organic film. Although structural properties of monolayers of simple organic molecules, for example, of the homologous series of fatty acids on pure water are well characterized, effects of even the simplest metal ions on the structure of the organic monolayers have not been so far adequately understood. We will explore the effects of aqueous metal salts on the structure of Langmuir monolayers under a variety of experimental conditions.

Langmuir films range from simple saturated fatty acids to complicated networks of protein matrices floating on water. The inorganic complexes, usually metal salts, are dissolved in the aqueous subphase and allowed to interact with the weakly acidic headgroups of the organic molecule at the water surface. Generally, when ions are present in the subphase, the monolayer becomes much better ordered [**4**], changes its viscoelastic response [**5**], and transfers more easily to a solid substrate [**6**]. Some ions stabilize the organic film on the solid substrate very well, yet others have weak or no effect. Studying the ion-induced structures in the precursor Langmuir films helps understanding the macroscopic properties of the LB-films.

Organic films on aqueous solutions of metal salts are not only interesting from an applied, but also from a fundamental point of view. Theoretical calculations [**7**] treat the organic film and ions as a two dimensional model of an electrochemical double layer, and provide analytical expressions for the electrostatic potential and ions concentration at the surface. However, in such theoretical considerations, the fact that ions do not bind to the organic monolayers from a vacuum, but from an aqueous solution, is often overlooked. Systematically varying thermodynamic and kinetic parameters in the aqueous subphase, such as temperature, pH, and ion concentration, changes the hydrolysis and hydration state of ions, and thus, the nature of bonds of the aqueous ions with the headgroups. It remains to be seen whether the simple picture of electrostatic ion-headgroup interactions is adequate or whether water assists formation of complex oxo-hydroxo bridges at the organic-inorganic interface.

Finally, the organic films can be used, for example, as templates to grow oriented crystals from supersaturated aqueous salts [**8**]. They have been well-known to affect the structure, size, morphology, and orientation of inorganic crystals growing from the aqueous subphase. The organic-template-directed nucleation of salts presumably stems from a structural match between the interfacial lattices of the organic molecules and the metal atoms, but experimental evidence has been limited. The key question concerns the role of a geometrical match (epitaxy) at the organic-inorganic interface, and whether ordering of atoms can take place on a structured organic surface, and if so, how?

Grazing incidence synchrotron x-ray diffraction (GID) is the only surface sensitive technique that allows the determination of in-situ structures of both the organic monolayer as well as the inorganic counter-layers with an atomic resolution. We will use GID to study the effects on the organic-inorganic interface of: i) pH alone (no divalent ions), ii) monovalent ions, iii) divalent ions (dilute and supersaturated concentrations), and iv) the oriented crystal nucleation.

CHAPTER 1

Brief review of previous work on Langmuir monolayers

1.1. On pure water

Langmuir films consist of amphiphilic molecules: one part of the molecule is hydrophilic ("likes" water), while the other part is hydrophobic ("dislikes" water). Hydrophilic groups, for example, carboxylic acid, sulphates, amines and alcohols are attracted to polar media such as water. Hydrophobic groups, for example, hydrocarbon chains, fats and lipids are highly insoluble in water. Amphiphilic molecules float at the water surface because they posses two different types of bonding within one molecular structure. A proper balance between the hydrophilic (coulomb type) and hydrophobic (van der Waal's type) forces traps the molecules at the surface. If the hydrophobic part is too short, the molecule will "drown" into the subphase, and if, on the other hand, the hydrophobic part is too large, the molecules will not form a monolayer, but collapse into multi-layers and micelles.

Langmuir monolayers have first been studied by making isotherm measurements, that is, by observing changes in the surface pressure as a function of the area at constant temperature [**9, 10**]. Structural phase transitions in the monolayer are manifested as "kinks" in the isotherm. Other techniques have been developed to study the macroscopic properties of these films in the past couple of decades: Brewster angle microscopy[**11, 12**] and polarized fluorescence microscopy[**13**] give information on the texture; second-harmonic generation[**14, 15, 16**] and infrared sum-frequency generation[**17**] give information on the average orientation of the headgroups; and viscosity measurements and quasi-elastic light scattering[**18**] give information on the mechanical properties.

The information about the structure of phases on an atomic scale was revealed only recently through the use of highly collimated and brilliant synchrotron radiation sources[**19, 20, 21, 22, 23, 24, 25, 2, 26**]. The X-rays reveal that the phase transitions involve a high degree of orientational and translational ordering of centers of masses of the molecules. The phase transitions are classified in terms of the tilt of the molecule relative to the water plane, the tilt azimuth (nearest neighbor "NN," next nearest neighbor "NNN," or intermediate), the orientation of its short axis (backbone plane), and the orientation of the head group[**27**].

In chapter 3, we will present results of grazing incidence X-ray diffraction studies concerning the effect of pH (and thus, of headgroup dissociation) on Langmuir monolayers of fatty acids on pure water. An increase in pH transforms the distorted-hexagonal S phase first to the partially disordered *Rotator-I* phase with less distortion, and then to the completely disordered *Rotator-II* phase with an undistorted hexagonal structure. The *S-Rotator-I* and *Rotator-I-Rotator-II* transitions are pushed to lower temperatures with increase in pH. The fact that the effects of pH increase are almost identical to the effects of increasing temperature indicates the important role of headgroup-headgroup interactions in these monolayer phases.

1.2. On dilute salt solutions

Dissolving salts in the aqueous subphase effects the structure of Langmuir monolayers. The role of metal ions has been extensively studied in organic films at air-solid interfaces (i.e., in LB films) as well as at the air-water interface[**4, 6, 28, 29, 30**]. The area per molecular headgroup of the specific fatty acid salt at the solid interface has been correlated with Pauling's electronegativity of the corresponding counterion, and a determination of the degree of the covalent or ionic nature of the bond has been made[**6**]. Surface potential measurements on monolayers at the air-water interface[**28**] showed that the alkaline earth metals (Ba, Ca, and Mg) make electrostatic bonds with the headgroups and Pb, Cd, and Co interact by covalent bonding. In an infrared reflection-absorption spectrometry on Langmuir monolayers[**29**], Cd and Pb induced a formation of more ordered structures than Ca did. This effect was again explained by varying degree of ionic or covalent bonding: covalent for Cd and Pb and ionic for Ca.

The effect of divalent metal ions on Langmuir monolayers was also recently studied with grazing incidence diffraction (GID) of synchrotron X-rays. This study[**31**] divided the interactions into two categories. The first kind of interaction produces high pressure monolayer phases at low surface pressure, i.e., creates an "effective high pressure" by attracting the headgroups closer together. As this phenomenon has been observed with electropositive metals such as calcium[**32**], a radially symmetric screened Coulomb type interaction is assumed to be involved[**27**]. The second category of headgroup-ion forces is seen with more electronegative ions such as cadmium[**3**]. This interaction produces an entirely new phase with an asymmetrically distorted, i.e., chiral lattice of the monolayer. More interestingly, it also produces a number of weak diffraction peaks that have been indexed as a supercell of the monolayer lattice. This superlattice is claimed to be due to a monolayer of cadmium or, as suggested by reflectivity data[**3**], $CdOH^+$ ions forming a two-dimensional lattice. The formation of this new structure is presumed to be due to an anisotropic, polar-bond forming interaction between a weak acid and an electronegative metal ion.

In chapter 4, we will show that divalent ions dissolved in the aqueous subphase of fatty acid Langmuir monolayers have two types of effects on the structure of the organic film. The first and more familiar effect is to induce a structure similar to the high-pressure "S" phase on pure water, even at low pressures; ions of the first type include $Ni^{2+}(aq)$, $Ba^{2+}(aq)$, $Co^{2+}(aq)$, and $Cu^{2+}(aq)$. The presence of ions of the second type results in the appearance of superlattice structures: we see a 1×2 superlattice with $Mn^{2+}(aq)$ and a 2×2 superlattice with $Mg^{2+}(aq)$, and it is known that $Cd^{2+}(aq)$ and $Pb^{2+}(aq)$ also cause the formation of superlattices. Out-of-plane (Bragg rod) scans indicate that $Mn^{2+}(aq)$ and $Mg^{2+}(aq)$ interact with the headgroups so strongly that the organic film buckles, with a periodic out-of-plane density modulation (amplitude ∼2.5 Å). In addition, a thin (∼4 Å) ordered inorganic layer forms in the subphase under the Langmuir film.

We will also use anomalous x-ray scattering to figure out the physical origin of the "superlattices." Our studies of fatty acid monolayers spread on a dilute aqueous solution of lead ions indicate that a ∼5 Å thick ordered layer is formed in the subphase. The lattice is commensurate with the organic lattice and has 14 times the unit cell area. It is unlikely that lead ions alone would form such a large repeat unit; indeed, using anomalous X-ray scattering, we detect no evidence of lead within the ordered layer. Thus, the interfacial superlattice is not simply an array of lead ions but may consist of lead hydrolysis products and water molecules.

1.3. On supersaturated salt solutions – biomineralization

In many biologically controlled ("organic-matrix-mediated") processes, macromolecular substrates direct the nucleation of crystalline biological components, for example, of skeletal materials[**33, 34**]. Langmuir monolayers are often used as templates to grow oriented crystals from dissolved salts, a model biomineralization process[**35, 8, 36, 37, 38, 39**]. The weakly acidic headgroups of the organic molecules attract supersaturated aqueous ions of metal salts to the water surface, where the ions aggregate in large concentrations and grow into crystals. The organic film acts as the nucleation catalyst; it lowers the activation energy for cluster formation and allows the metal salt to nucleate. In contrast to the spontaneous, uncontrolled precipitation of a salt from an aqueous solution in a "beaker", the crystallization of a salt under the organic monolayer proceeds in a controlled manner: the crystallites grow preferentially oriented to the plane of the organic template, and have specific morphology and size. These "orientation phenomena" have been studied in matrix-mediated-growth of crystals such as $CaCO_3$ [**40, 41, 42, 43, 44**], CaC_2O_4 [**45**], $BaSO_4$ [**46, 47, 48**], KH_2PO_4 [**49**], BaF_2 [**50, 51**], CdS [**52**], and PbS [**53, 54**], mostly by various methods ex-situ – the crystals are collected out of the solution and examined by optical, transmission electron, scanning electron, Brewster angle, and atomic force microscopies; x-ray photonelectron spectroscopy; energy-dispersive x-ray analysis; and in-house electron and x-ray diffraction. A wealth of information has been accumulated about the choice of an organic film suited for nucleation of a particular mineral and about the precursor subphase conditions, such as the level of ion supersaturation and pH, necessary for the face-selective nucleation of a particular polymorph. None of these studies, however, provide experimental information about the mechanism that drives these phenomena at the microscopic (atomistic) level.

The current explanation for the preferentially oriented inorganic nucleation at the organic template is based on a popular (and a reasonable) assumption that the face-selective nucleation stems from a match between the interfacial lattices of the organic molecules and inorganic molecules. A search for such interfacial organic-inorganic registry has recently begun using grazing incidence diffraction (GID). Although previous GID studies on dilute solutions of aqueous salts [**55, 56, 57**] found diffraction spots from superlattices, these peaks could not be assigned to any known structures of bulk compounds. Such salts, for example, manganese, magnesium, cadmium, or lead chloride, either did not grow at the interface beyond the first monolayer, or grew as non-oriented powders at supersaturated concentrations. GID studies have also been done on oriented crystal growth of glycine under Langmuir monolayers of α-amino acids [**58**], and on growth of oriented ice under alcohol monolayers [**59**]. When nucleating glycine crystals, the evidence for epitaxy was that the monolayer of α-amino acid molecules of a single handedness selectively induced formation of the enantiomeric crystal face composed of molecules of the opposite handedness. In the case of ice nucleation, an approximate (within 0.5 Å) lattice match between arrangements of the oxygen atoms in the layer of hexagonal ice and of the oxygen atoms in the alcohol molecules was observed. In either case, no precise linear relationship between the basis vectors of the organic and inorganic lattices has been determined. The results described in chapter 5 do indeed show, for the first time, that a registry at an organic-inorganic interface exists, and so experimentally validate the popular assumptions about the role of epitaxy in organic-matrix-mediated nucleation of inorganic compounds. Not only do we show that atomistic ordering processes can take place on a structured organic surface, but we also observe how this happens.

CHAPTER 2

Techniques and methodology

2.1. Surface x-ray diffraction

The low flux of laboratory sources, coupled with the low scattering cross section for x-rays, mean that in-house x-ray diffraction is not usually used to study thin films on the monolayer scale, and in fact, cannot be used to obtain information on the crystalline packing arrangement of Langmuir monolayers. It is only recently, with the advent of intense and well collimated X-ray beams of tunable wavelength from synchrotron sources, that it has become possible to obtain direct structural information on the packing of these films via X-ray surface methods.

2.1.1. Evanescent wave

When x-rays fall on the sample at an incidence angle α_i smaller than the critical angle α_c for total external reflection, the penetration depth of the incident x-ray beam is only a few tens of angstroms. The refracted beam (the evanescent wave) cannot travel further inside the medium. The intensity of evanescent waves decays exponentially (rather than sinusoidally) with distance from the interface at which they are formed. In such grazing incidence geometry, the x-rays are said to be “surface sensitive”; that is, the evanescent wave only probes the crystalline structure in the vicinity of the surface. The undesired scattering from the bulk material, e.g. water in the case of Langmuir monolayer, is thus minimized.

Total reflection is a process that occurs when Snell's law $n_1 \cos\alpha = n_2 \cos\alpha'$ for refraction can no longer be solved for real angles. For most materials, the index of refraction is slightly less than unity at x-ray wavelengths. The index of refraction may be written as $n = 1 - \delta - i\beta$ where $\delta = \frac{r_e \rho \lambda^2}{2\pi}$ and β is related to photo-electric absorption. If $\delta > 0$ and $\beta \approx 0$, and the incident x-rays are propagating in air (for which $n_1 = 1$), then by Snell's law x-rays will undergo total external reflection for angle $\alpha < \alpha_c$, where $\cos alpha_c = 1 - \delta$. Thus $\alpha_c \approx \sqrt{2\delta} \approx 0.00164\lambda[\text{Å}]\sqrt{\rho[g/cm^3]}$. For water, $\rho = 1g/cm^3$, the critical angle for total external reflection of x-rays at energy 8KeV ($\lambda = 1.5498$ Å) is $\alpha_c = 2.5$ mrad.

It is desirable that the maximum flux of photons impinges on the water surface at a well defined incidence angle because the photons that fall on the sample at a higher than the critical angle for total external reflection will refract deep into the water and the scattering will be overwhelmed by the background noise from the bulk. The precise incidence angle can only be defined by a well-collimated beam provided by synchrotron radiation.

2.1.2. The structure factor

The sample is irradiated by a plane wave of x-rays with incident wave vector $\vec{k_i}$. In elastic scattering, scattered radiation with wave vector $\vec{k_f}$ will be observed. Instead of $\vec{k_f}$, the direction of observation is specified by $\vec{K} = (\vec{k_f} - \vec{k_i})$, the so called momentum transfer vector. The intensity I_{hkl} of reflection hkl is proportional to the square of the structure factor F_{hkl}. The structure factor can be expressed as a summation of waves scattered from every infinitesimal volume element dV by the expression:

$$F(\vec{K}) = \int_{\text{cell}} \rho(\vec{r}) e^{2\pi i \vec{K}\cdot\vec{r}} d^3\vec{r} \tag{2.1}$$

where $\rho(\vec{r})$ is the electron density at position $\vec{r} = (x, y, z)$, and $\vec{K}$ is the scattering vector (hkl). If we introduce the atomic scattering factor f_j, the integral reduces to a sum over the atoms j in the unit cell, and the structure factor can be expressed as

$$F(\vec{K}) = \sum_i f_j(\vec{K}) e^{(2\pi i \vec{r_j}\cdot\vec{K})} \tag{2.2}$$

where $\vec{r_j}$ describes the coordinates of the jth atom.

2.2. Surface crystallography

The momentum transfer vector in the reciprocal space is given by $\vec{K_{hk}} = h\vec{a^*} + k\vec{b^*}$, where $\vec{a^*}$ and $\vec{b^*}$ are the primitive translation vectors of the reciprocal lattice. In the real space, it is convenient to express the vectors $\vec{r_j}$ (positions of atoms within a unit cell) in terms of components along the unit cell vectors $\vec{a_1}\vec{a_2}$ by means of fractional coordinates x_j, y_j which are numbers between zero and unity, so that

$$\vec{r_j} = x_j\vec{a} + y_j\vec{b} \tag{2.3}$$

It turns out that the intensity I (the square of the structure factor, Eq.2.2) will be maximum whenever two conditions (the Laue equations) are simultaneously satisfied:

$$\vec{K} \cdot \vec{a} = 2h\pi \tag{2.4}$$

$$\vec{K} \cdot \vec{b} = 2k\pi \tag{2.5}$$

For an hk reflection, we are interested in the value of the structure factor when the Bragg law is satisfied. Equation 2.2 becomes

$$F_{hkl} = \sum_j f_j e^{2\pi i(hx_j + ky_j + lz_j)} \tag{2.6}$$

If we define the vectors of the unit-cell of the reciprocal lattice as follows:

$$\vec{a^*} = \frac{\vec{b} \times \hat{n}}{\vec{a} \cdot \vec{b} \times \hat{n}} \tag{2.7}$$

$$\vec{b^*} = \frac{\hat{n} \times \vec{a}}{\vec{a} \cdot \vec{b} \times \hat{n}}, \tag{2.8}$$

where $\hat{n} = \frac{\vec{a} \times \vec{b}}{|\vec{a} \times \vec{b}|}$ is a unit vector normal to the plane of the 2-D unit cell, we find that equations 2.4 and 2.5 above are satisfied.

Most monolayers have a distorted hexagonal structure. We define the real space primitive unit-cell per one molecule as a parallelogram outlined by vectors $\vec{a}$ and $\vec{b}$, with an obtuse angle γ between them. Once the magnitude of the momentum transfer vector of the reciprocal space is determined from the diffraction measurement, and using $|\vec{K}_{hk}| = 2\pi/d_{hk}$, we can use the definitions 2.7 and 2.8 to figure out the unit-cell parameters in the real space:

$$\frac{1}{d_{hk}^2} = \frac{1}{\sin^2 \gamma} \left(\frac{h^2}{a^2} + \frac{k^2}{b^2} - \frac{2hk}{ab} \cos \gamma \right) \tag{2.9}$$

and the area $A = ab \sin \gamma$.

Because Langmuir monolayers are powders in the plane, the in-plane components K_x and K_y cannot be determined individually, but only as a combination $K_{xy} = \sqrt{K_x^2 + K_y^2}$, and as a consequence, some peaks with different (hk) may overlap in the diffraction pattern. For example, if the monolayer molecules pack in a hexagonal arrangement ($|\vec{a}| = |\vec{b}|$ and $\gamma = 120\,^\circ$), only one first-order peak will be observed (triply degenerate) and indexed as $(01)+(10)+(1\bar{1})$. Or, if the monolayer unit-cell is symmetrically distorted ($|\vec{a}| = |\vec{b}|$ and $\gamma \neq 120\,^\circ$), two first-order peaks will be observed: one non-degenerate (10) and one doubly degenerate $(01) + (1\bar{1})$ of twice the intensity. Finally, if the molecules pack in a structure with an oblique unit-cell of the least symmetry ($\vec{a} \neq \vec{b}$ and $\gamma \neq 120\,^\circ$), three non-degenerate peak will be observed. The indexing scheme is usually guessed for the low-order peaks at first and verified by the positions of higher-order peaks later.

In a real-space two-dimensional lattice of point particles, there is no periodicity in the direction normal to the lattice plane, and thus, there is no condition to be satisfied by the out-of-plane $\vec{K_z}$ component of the diffracted wave vector. An out-of-plane scan of this (fictitious) lattice, while holding $\vec{K_{xy}}$ fixed such that the 2-D Bragg condition is met, will reveal a curve of constant intensity. In other words, in the reciprocal space, the lattice will consist of a two-dimensional array of vertical "lines," or as they are called, "rods" that extend infinitely in the direction normal to the plane of lattice points.

Molecules of the Langmuir monolayer are not, of course, point particles. A fatty acid molecule consists of a headgroup and an aliphatic chain, and it can be treated as a rigid rod with a noncircular cross section. The molecular degrees of freedom are tilt, orientation of the molecular backbones, and the orientation of the headgroup. Depending on the surface pressure and temperature, the molecules can thus undergo a variety of structural phase transition characterized by the extent of tilt, the tilt azimuth, the distortion azimuth of the unit-cell, and the direction of the crystallization wave. Depending on the structure, features of Bragg rods can then be calculated from the structure factor, Eq. 2.1.

When the molecules pack in a tilted structure, some of the peaks (depending on the azimuth of the tilt) will move out-of-plane. Measuring how far the peaks move out-of-plane helps determining the amount of tilt. A set of elegant equations for determination of the tilt parameters (tilt magnitude θ and direction β, respectively), and other lattice parameters (area A, unit-cell distortion magnitude ξ, and unit-cell distortion azimuth ω) are described in ref. [**60**], and are presented here without derivation. The peaks are arbitrarily labeled 1,2, and 3, with degenerate peaks labeled twice. The two azimuths ω and β are then given with respect to the average NN direction closest to peak 1. First the lattice parameters are calculated in term of the three in-plane peak coordinates K_{xy}, together with two auxiliary parameters κ and χ:

$$
\begin{aligned}
\xi &= \sqrt{2}\frac{\sqrt{\langle (K^2 - \langle K^2 \rangle)^2 \rangle}}{\langle K^2 \rangle}, \\
A &= \frac{8\pi^2}{\sqrt{3}\langle K^2 \rangle \sqrt{1-\xi^2}}, \\
\kappa &= \sqrt{2}\frac{\langle (K^2 - \langle K^2 \rangle)^3 \rangle}{(\langle (K^2 - \langle K^2 \rangle)^2 \rangle)^{3/2}}, \\
\omega &= \frac{\pi}{3}(l-1) + \frac{1}{6} \cdot (-1)^{(s-l+3)\mathrm{mod}3} \cos^{-1}\kappa, \\
\chi &= \xi e^{2i\omega}/(1+\sqrt{1-\xi^2}),
\end{aligned}
\tag{2.10}
$$

where l is the label of the peak with largest K_{xy} and s that of the smallest, and corner brackets represent averages of the enclosed expressions with K set equal to values K_{1xy}, K_{2xy}, and K_{3xy} of the three peaks.

Substituting the total wave vector lengths $K = \sqrt{K_{xy}^2 + K_z^2}$ for K_{xy} in the above equations gives the corresponding parameters A', ξ', κ', ω', and χ' for the lattice in the plane normal to the chain axes. Then τ, the complex tilt parameter, defined in terms of the tilt magnitude θ and azimuth as $\tau = \tan^2(\theta/2)\exp 2i\beta$, is given by $\tau = (\chi' - \chi)/(1 - \chi'\chi^*)$.

2.3. Bragg rods

Calculating the tilt directly from the structure factor (Eq. 2.1) has an advantage over the previous method (Eq. 2.10) if information is needed about the thickness of the film. For simplicity, we assume that the electron density can be described by a cylindrical rod of length L, and define the unit vector $\hat{L}$ that points along the rod. The structure factor (Eq. 2.1) can be simplified to a line integral:

$$F(\vec{K}) = \left| \int_{-\frac{L}{2}}^{\frac{L}{2}} e^{-ix\vec{K}\cdot\hat{L}} dx \right|^2 = \frac{\sin \frac{1}{2}\vec{K} \cdot L\hat{L}}{\frac{1}{2}\vec{K} \cdot L\hat{L}} \tag{2.11}$$

This function is peaked when $\frac{1}{2}\vec{K} \cdot L\hat{L} = 0$, which will lead to off-plane diffraction ($\vec{K}_z \neq 0$) whenever $\hat{L}$ is tilted from the surface normal (that is, when $\hat{L}$ has a non-zero horizontal component). Note that the "vertical" width of the diffraction peak is determined by the length, L, of the molecule.

In our studies, we will encounter a situation where the fatty-acid molecules pack in a way that some of the aliphatic chains protrude over those of others. The film gets buckled such that the protrusions actually form a periodic array. In that case, the intensity profile as a function of a Bragg rod can be calculated from the molecular structure factor (Eq. 2.2) as:

$$F(\mathbf{K}_{hk}; K_z) = \sum_j f_j e^{i(\mathbf{K}_{hk}\cdot\mathbf{r}_j + K_z\cdot z_j)} \tag{2.12}$$

where each atom j has an atomic form factor f_j and is at position $\mathbf{r}_j + z_j \cdot \hat{\mathbf{n}}$, and where $\mathbf{r}_j = (x_j/a)\mathbf{a} + (y_j/b)\mathbf{b}$ and x_j, y_j, and z_j are the coordinates of the jth atom within the unit cell. Unlike in the 3-D crystal, a contribution to the structure factor is obtained in the out-of-plane direction even when $K_z \cdot z \neq 2\pi l$, where l is an integer, since a monolayer has no periodicity in the z-direction. The intensity profile is proportional to $|F|^2$ and is also corrected for geometrical effects ($\propto 1/\sin(2\theta_{hk})$), Lorentz ($\propto 1/\sin(2\theta_{hk})$), and polarization ($= \cos^2(2\theta_{hk})$) factors[**61**], where $2\theta_{hk}$ is the horizontal angle between the incident and the diffracted beam at reflections (hk). When the monolayer is in an untilted phase, the heneicosanoic molecule can be approximated by an upright cylindrical rod with N carbons of equal spacing of d and each with an atomic form factor f_c, and hence in a unit cell with one organic molecule (arbitrarily placed at the origin in the x-y plane, that is, $r_j = 0$):

$$F_{hk}(K_z) = f_c \sum_{j=0}^{N-1} e^{2\pi i(0) + i\cdot d\cdot j\cdot K_z} = f_c \frac{e^{i\cdot d\cdot N\cdot K_z} - 1}{e^{i\cdot d\cdot K_z} - 1} \tag{2.13}$$

$$I_{hk}(K_z) = |F|^2 = f_c^2 \frac{\sin^2(d\cdot N\cdot K_z/2)}{\sin^2(d\cdot K_z/2)} \tag{2.14}$$

The length of the molecule, $L = d \cdot N$ (this is also the thickness of the film in the untilted phase), can thus be easily found from the fit to the profile of Bragg rods at in-plane peaks from the organic film. When there are ordered subphase atoms present under the organic film, they must be included in the structure factor as well. If a nonprimitive unit cell contains m organic molecules (cylindrical rods) and n ordered subphase atoms, the structure factor can be rewritten as

$$\begin{aligned} F_{hk}(K_z) = f_c \frac{e^{i \cdot d \cdot N \cdot K_z} - 1}{e^{i \cdot d \cdot K_z} - 1} \sum_m e^{2\pi i (h \cdot x_m/a + k \cdot y_m/b)} + \\ + \sum_n f'_n e^{2\pi i (h \cdot x'_n/a' + k \cdot y'_n/b') + i \cdot K_z \cdot z'_n} \end{aligned} \tag{2.15}$$

where the entire heneicosanoic molecule is at fractional position coordinates x_m/a and y_m/b and f'_n is the atomic form factor of the nth subphase atom at fractional coordinates x'_n/a' and y'_n/b' and at coordinate z'_n, whose direction is positive upward with zero defined at the headgroup of the organic molecule. Because lattice fluctuations cause the peak intensities to decay rapidly with increasing K_{xy}, in-plane peaks at $\sin\theta/\lambda > 0.3$ are not observable, and the available diffraction data are not sufficient to perform structural analysis in a classical crystallography sense. The type, number, and positions of subphase atoms under the Langmuir monolayer are not known. Therefore, we do not follow the usual methods of the 3-D crystallography for the structure refinement such as the calculation of the reliability index[**62**]. We will show that the Bragg rods cannot be fitted without an ordered layer in the subphase. We will therefore include subphase "pseudo-atoms" representing the unknown atomic composition of the supercell, treat their positions and form factors as parameters, and search for a model that can simultaneously fit all Bragg rods by minimizing

$$\chi^2 \equiv \sum_{hk} \sum_{i=1}^{N_{data}^{hk}} \left(\frac{I_{hk,i}^{\mathrm{obs}} - I_{hk}^{\mathrm{calc}}(K_{z,i})}{\sigma_i} \right)^2 \tag{2.16}$$

where the sums run over all Bragg rods and for all data points in a particular Bragg rod, and σ_i is the estimated standard deviation of I^{obs}.

2.4. Peak-shifts and broadening

Diffraction peaks can shift from their usual positions and broaden because of lattice distortions due to defects. Lattice distortions in a crystal can be either uniform (macrostrain) or non-uniform (microstrain)[**63**]. The uniform lattice distortions are residual (unbalanced) stresses on the macroscale. The residual stress causes lattice spacings to expand or contract, and correspondingly, the diffraction peaks "shift" in the reciprocal space. In the case of non-uniform lattice distortions, the crystal does not have precise lattice spacings; instead, parts of the sample have spacings between $d - \Delta d$ and $d + \Delta d$ that diffract incoherently [**64**]. Such non-uniform lattice distortions cause broadening of the diffraction line shapes. The peak profiles will also be broadened due to the instrumental resolution, and due to the finite crystallite size. The objective of the analysis is to deconvolute the profiles of the broadening functions and separate out the contribution to the broadening from the effects of instrumental resolution, size, and strain. We use simplified integral breadth methods [**65**] to estimate information about the size of crystallites and the effect of microstrain, and work in terms of the convenient angular variable K_{xy}, where $K_{xy} = \frac{4\pi}{\lambda}\sin\theta_{xy}$. We label the integral breadths of the profiles from size, strain, and instrumental broadening as $(\delta K_{xy})^{\mathrm{S}}$, $(\delta K_{xy})^{\mathrm{D}}$, and $(\delta K_{xy})^{\mathrm{R}}$ respectively. The integral breadth, $W(K) = \frac{1}{I_p}\int I(K)d(K)$, is the width of a rectangle having the same area and peak height as the actual line profile. Furthermore, we assume a Gaussian shape for the functions of the various broadening effects, and so $(K_{xy})^2_{\mathrm{o}} = [(\delta K_{xy})^{\mathrm{S}}]^2 + [(\delta K_{xy})^{\mathrm{D}}]^2 + [(\delta K_{xy})^{\mathrm{R}}]^2$. According to the Scherrer formula, the pure integral line breadth resulting from small crystallite size is $(\delta 2\theta_{xy})^{\mathrm{S}} = \frac{C\lambda}{L\cos\theta_{xy}}$ or on the K_{xy} scale $(\delta K_{xy})^{\mathrm{S}} = \frac{2\pi}{L}$, where C has been set to 1 (for integral width). The integral profile breadth in K_{xy} units due to distortions (microstrain) alone may be expressed as $(\delta K_{xy})^{\mathrm{D}} = 8\pi e\frac{\sin\theta_{xy}}{\lambda} = 2eK_{xy}$, where K, θ, and λ, have their usual meanings and $e \simeq (\Delta d/\bar{d})_{hkl}$ is an approximate upper limit of the lattice distortions. The breadth for the instrumental resolution function $(\delta 2\theta_{xy})^{\mathrm{R}}$ was measured experimentally from a silicon powder standard, and it can be rewritten on the K_{xy} scale as $(\delta K_{xy})^{\mathrm{R}} = \frac{(\delta 2\theta_{xy})^{\mathrm{R}}}{2}\sqrt{\frac{16\pi^2}{\lambda^2} - K_{xy}^2}$. When both size and strain broadening are present, the overall broadening effect is thus $(\delta K_{xy})_{\mathrm{o}}^2 = \left(\frac{2\pi}{L}\right)^2 + (2eK_{xy})^2 + \left(\frac{(\delta 2\theta_{xy})^{\mathrm{R}}}{2}\sqrt{\frac{16\pi^2}{\lambda^2} - K_{xy}^2}\right)^2$. We plot $(\delta K_{xy})_{\mathrm{o}}$ against K_{xy} and obtain the mean crystallite dimension L and the "maximum" lattice distortion e as the parameters of the fit.

2.5. Data collection

2.5.1. Description of the Langmuir trough

A Langmuir trough consists of a shallow well that holds the subphase water (it should be shallow in order to minimize roughness caused by capillary waves). The trough we used was designed and built by Binhua Lin and modified by Mingchih Shih. It is described in both of their theses [**1, 66**]. Drawings of the trough appear in Figures 2.1 and 2.2. The trough is milled from aluminum, which provides rigidity and acceptable thermal conductivity for temperature control. All parts of the trough which come into contact with either the monolayer or its pure water subphase are coated with Halar, a fluoropolymer similar to Teflon, (or in the case of the barrier, made out of mylar). These include the 11in by 6in well which has 1/4 inch high surrounding walls. These walls are cut down to 1/32 in at the front

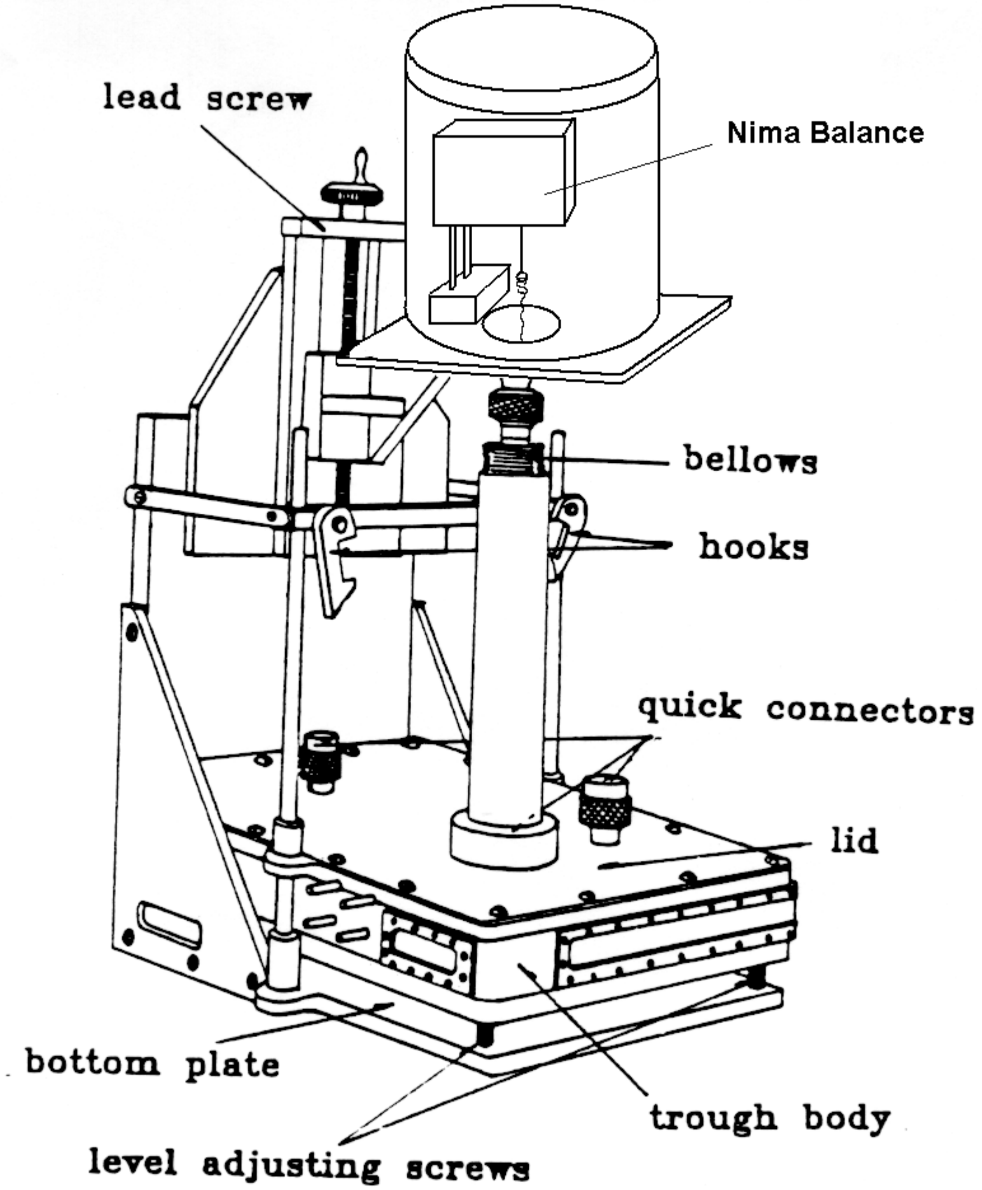

Figure 2.1. Schematic diagram of the trough set-up for diffraction experiments. The trough is modified from that of ref [**1**].

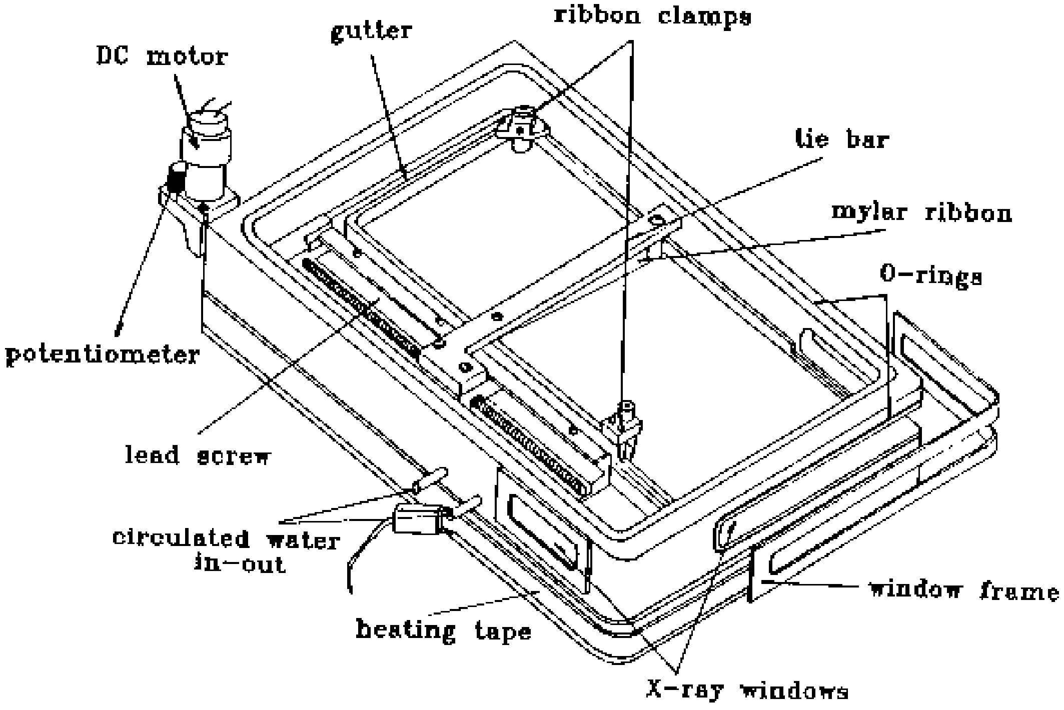

Figure 2.2. Detailed sketch of the trough body, taken from ref [**1**].

of the trough so that the X-rays can enter and exit without being blocked. At this position, the water is held in place only by the surface tension of its inverted meniscus (the meniscus is inverted because clean Halar is hydrophobic).

The trough has channels just beneath the Halar coated well. Heated or cooled water is pushed through these channels by a VWR 1155 circulator in order to maintain constant temperature. Temperature is measured using a platinum Resistance Temperature Detector (RTD from Omega Engineering) embedded in glass and inserted into the aluminum body of the trough. Temperature is controlled to $\pm 1°$C by an Omega 6000 microprocessor-based unit which drives the 110V heater in the circulator through a 45-amp solid-state relay.

The trough is designed with O-rings such that after monolayer preparation the lid can be lowered and the entire environment made airtight. This allows us to reduce vibrations due to air-circulation. We also maintain a slight over-pressure of Helium in order to minimize radiation damage and air-scattering of the X-rays. Heated or cooled water is driven through the trough lid by a separate circulator, so that the entire monolayer environment is temperature controlled. The water in the lid is maintained at roughly 2.5 °C above the set temperature of the trough in order to prevent condensation (which might drip down and contaminate the monolayer).

A ribbon barrier made of Teflon or Mylar controls the monolayer area per molecule. The ribbon is held at the back-right corner and the front-left corner of the trough well by Teflon knobs, and threads through a Halar coated aluminum tie bar which can be moved from ∼1 in shy of the back of the trough to ∼2 in shy of the front. This changes the area available to the monolayer from ∼60 in^2 to ∼12 in^2 (a 5:1 compression ratio). The barrier skims the water surface, allowing the water to flow beneath it, but forcing molecules which are constrained to the surface closer together. The motion is accomplished by way of a 10in travel capacity linear translator (from Unislide) coupled to a DC motor. A potentiometer records the motion of the barrier; this reading can be used to calculate the total area permitted to the monolayer.

To ensure a high level of purity, one typically starts with a trough either made from or coated with a fluoropolymer that can be easily and thoroughly cleaned. Our trough is cleaned using the following procedures: Once or twice a year it is soaked in Nitric acid and then copiously rinsed with purified water to remove metallic impurities. Once or twice a week it is rinsed and scrubbed with high grade acetone and methanol to remove organic impurities and the remains of previous lipid films. Before each new film, it is rinsed at least twice with purified water. We purify our water with a four-cartridge Barnstead Nanopure II system, using a pretreatment cartridge, an ultra-pure ion exchange cartridge, a high capacity ion exchange cartridge, an organic-free cartridge, and a hollow fiber 0.2μ final filter. For temporary storage and transport, we use Teflon-coated polyethylene bottles. We clean glassware (including volumetric flasks for spreading solutions, as well as beakers and flasks that held cleaning solvents) by soaking it in Nochromix (an oxidizer) mixed with sulfuric acid, then by rinsing with pure water and methanol, and finally by sonicating with acetone.

2.5.2. Preparation of a Langmuir monolayer

Although any surfactant can be used to prepare a Langmuir monolayer, we work with heneicosanoic acid, a saturated fatty acid. A thin organic film is prepared by 'spreading' the organic molecules at the water surface. First, the amphiphilic compound is dissolved in a suitable organic solvent. For fatty-acids, chloroform is a good solvent. Second, a small amount $(60 - 100\mu L)$ of the solution is drawn into a micro syringe. Third, small drops are allowed to fall from the syringe while it is held a few millimeters above the subphase. The solvent evaporates, leaving only the monolayer of organic molecules at the surface.

We measure the surface pressure using the Wilhelmy plate technique. A small square of chromatography paper (2cm x 1cm) makes physical contact with the water while hanging from the arm of a tensiometer. Changes in the surface tension are recorded as slight changes in the force on the tensiometer arm. The reading of the tensiometer (ST9000, Nima Technology) just before the film is spread is taken to be the zero point (i.e., the surface tension of pure water). Deviations of this value during compression are measured as a voltage and converted into a 2D pressure (units of dynes/cm). The surface tension can also serve as a test for trough cleanliness. The pressure is measured as the barrier is moved forward or back. Any significant deviations from the zero point indicate that there are surface active impurities which must be removed before a film is spread.

2.5.3. Description of the diffraction apparatus

The experimental geometry is shown in Figure 2.3. Because the scattering is elastic, the magnitude of the incoming and outgoing wave vectors are $|\vec{k_f}| = |\vec{k_i}| = \frac{2\pi}{\lambda}$ where λ is the x-ray wavelength. The scintillation detector moves on a circle in the horizontal plane (in the plane of water). It can also move up and down, and tilt in the vertical plane. The position of the detector is given by the angle 2θ in the horizontal plane, and the height h and tilt α in the vertical plane, as shown in Figure 2.3b. Instead of the angular variables in the real space, it is convenient to track the position of the detector in terms of the momentum transfer vector $\vec{K} = \vec{k_f} - \vec{k_i}$ in the reciprocal space. Magnitudes of the components of $\vec{K}$ are

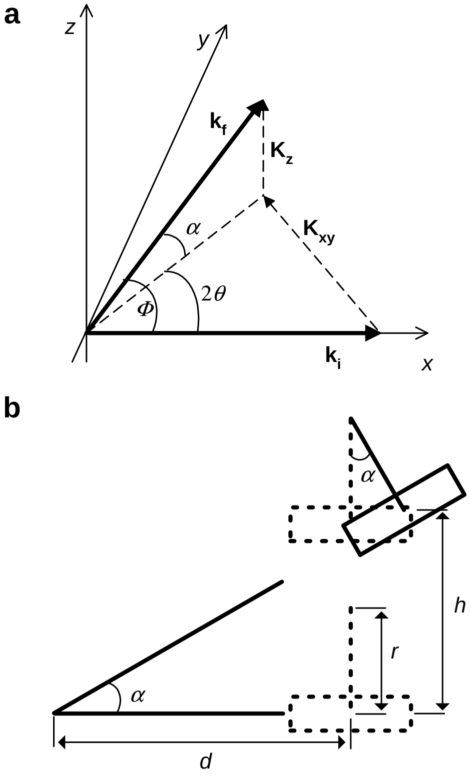

Figure 2.3. Schematic diagram of the scattering geometry. (a) The incident beam is represented by its wave vector $\vec{k_i}$, and the scattered beam by $\vec{k_f}$. The in-plane and out-of-plane components of the momentum transfer vector $\vec{K} = \vec{k_f} - \vec{k_i}$ are shown as $\vec{K_{xy}}$ and $\vec{K_z}$ respectively. (b) Cross-section containing the plane defined by $\vec{k_f}$ and $\vec{K_z}$. The detector is schematically shown as a rectangle. Dashed lines outline the position of the detector before it is raised by h and tilted by α. See text for the description of other parameters.

related to the real space angles by:

$$|\vec{K_{xy}}|^2 = \left(\frac{2\pi}{\lambda}\right)^2 \times (1 + \cos^2\alpha - 2\cos\alpha\cos 2\theta) \tag{2.17}$$

$$|\vec{K_z}| = \frac{2\pi}{\lambda}\sin\alpha \tag{2.18}$$

The detector actually sits on a cradle, so when it tilts, the pivot point can be imagined above the detector as shown in Figure 2.3b. When the detector tilts by the angle α, it also needs to be raised to a height h:

$$h = d\tan\alpha + r\left(\frac{1}{\cos\alpha} - 1\right), \tag{2.19}$$

where d is the distance from the sample to a mark on the detector below the pivot point, and r is the distance from the pivot point to the detector (or in other words, r is the "radius" of the circular motion that the detector outlines as it tilts).

Stepper motors adjust the angle, tilt and height of the detector. The motors are controlled by a modular motion control system engineered by the Advanced Control Systems Corporation (ACS). The motion system is controlled by a window-based application (developed in Delphi by me) on a laptop. The communication between the computer and the motor indexer is accomplished via an RS-232 serial port. Photons are detected by NaI scintillation detectors, whose signal are run through an amplifier to a single channel analyzer (SCA). The SCA output is read by a Dual Counter and Timer (Ortec, Model 994) and the counts are relayed to the computer again via an RS-232 serial port. Since the intensity of synchrotron x-rays varies both randomly and systematically, the detector counts are normalized by the number of incident photons. This is accomplished by placing a monitoring detector beyond the trough that detects the photons specularly reflected from the water (i.e., not diffracted).

X-ray diffraction experiments were performed at the X-14A beamline, operated by the Oak Ridge National Laboratory, at the National Synchrotron Light Source of the Brookhaven National Laboratory and at station 1-BM-C of the SRI-CAT (Synchrotron Radiation Instrumentation - Collaborative Access Team) at Sector 1 of the Advanced Photon Source at Argonne National Laboratory. The beamline personnel adjust the optics of the beamline such that the beam is only a few hundred microns wide vertically and at least 2cm wide in the horizontal plane. The wide horizontal width of the beam is easily achieved at X-14 and 1-BM-C because they are both bending magnet (BM) beamlines (as opposed to insertion device (ID) beamlines). The incident beam is focused at 'infinity' horizontally in order to minimize the spatial divergence. Horizontal divergence of the incident beam is undesired because it contributes to the degradation of instrumental resolution of the in-plane scattering. The beam at SRI-CAT enters the hutch downward, but at X14A we use a platinum-coated quartz mirror to redirect the beam onto the horizontal water surface at a grazing incident angle of $\sim$1.8 mrad, which is below the critical angle for total external reflection from water at 8Kev. Because of this low incident angle, the beam leaves a large footprint on the water surface. The spatial resolution of scattering from a broad collimated beam is determined by a set of crossed Soller slits in front of the detector. The vertical Soller slits consist of a series of parallel vertical plates, and the horizontal slits of horizontal plates. These slits define a horizontal resolution of $\sim$0.01 Å^{-1} full width at half maximum (FWHM) for K_{xy} scans and a vertical resolution of $\sim$0.05 Å^{-1} FWHM for K_z scans. The vertical resolution is adequate because the molecules have typical lengths of 15 Å to 30 Å, leading to peak widths between $\sim$0.12 Å^{-1} and $\sim$0.24Å^{-1}.

CHAPTER 3

Effects of pH on Langmuir monolayers

3.1. On pure water

In Langmuir monolayers, headgroup-headgroup interactions can be manipulated through dissociation of the heads(COOH to COO^-H^+ in fatty acids) by increasing the pH of the aqueous subphase. The increase in pH requires addition of an alkali to the subphase which necessarily also introduces a monovalent cation (e.g., Na^+, K^+, $NH4^+$, etc). GID studies of fatty acid monolayers at high pH have generally been carried out with an additional divalent metal ion in the subphase, where this ion has either predominantly electrovalent (e.g., Ca^{2+} (ref. [**32**])) or covalent (e.g., Cd^{2+} (ref. [**3**])) bonding to the headgroup anion. Some early studies on the isotherms and surface potential measurements [**67, 68**] of fatty acid monolayers at high pH, without a divalent metal ion, have been performed. An amino acid monolayer has been studied through GID at high pH in the absence of divalent ions [**69**]. Fluorescence microscopy and theoretical calculations on phospholipid vesicles [**70**] indicated a nonmonotonic lowering of the solidliquid phase transition temperature with an increase in strength of the monovalent ion in the subphase. In aqueous solutions of soaps, i.e., alkali salts of long chain fatty acids, above pH 10 the headgroups are fully dissociated to yield the carboxylate ions (COO^-) (ref. [**71**]). Between pH values of 7.0 and 10.0 the heads are partially ionized, and the two kinds of headgroups ($COOH$ and COO^-) form a hydrogen-bonded complex known as an acid soap[**72**]. Below pH 7.0 there is very little headgroup dissociation and the soap is almost completely converted to free fatty acid [**71**]. Here we present the first systematic GID studies of the effect of pH on a fatty acid Langmuir monolayer in absence of any extraneous cations other than that in the alkali required for raising the pH. In particular, there are no divalent cations. It is seen that increase in pH increases disorder in the monolayer. We propose that the increase in disorder be due to the formation of acid soap, i.e., a mixture of the two kinds of headgroups in the monolayer.

3.1.1. Experimental details

A 0.87 mg/mL solution of C_{21} acid in chloroform was spread. The temperature was varied from 9 to 18 °C (±0.1 °C) and the pH from 10 to 12. The surface pressure for most measurements was 30 dyn/cm but data were also taken at 5 dyn/cm, with (0.5 dyn/cm accuracy. A slight overpressure of helium was maintained in the trough to reduce radiation damage and air scattering. A new film was used for each set of pH and surface pressure measurements. The film was allowed to remain at a steady temperature for more than 30 min. As the temperature controller takes about the same time to register a steady temperature, almost an hour separates the spreading of the film and the first compression. Each new film was compressed (well below collapse pressure), decompressed, and recompressed to check reproducibility of the isotherm. This recompression was carried to the required surface pressure, the film was held at that constant pressure and X-rays were made incident on the monolayer. The area occupied by the film was seen to be almost constant over the entire period of data collection for the set, which was about 3-4 h. We did not see any significant radiation damage of the films.

3.1.2. Results – pH-dependent changes in phase boundaries

The effect of pH on the monolayer is illustrated in Figure 3.1. It shows the diffracted intensity as a function of K_{xy} as the pH increases from 10.5 to 12 at 15 °C and at 30 dyn/cm surface pressure. The two diffraction peaks at pH $\sim$ 10.5 can be assigned to a centered rectangular lattice with two molecules per unit cell. The distortion of this lattice from a regular hexagonal lattice is given by $\delta = \sqrt{3} - b/a$, where b/a is the ratio of the lattice parameters and $b/a = \sqrt{3}$ for a regular hexagon. In Table 3.1 we have presented the distortion parameters and areas per molecule of the different high-pressure phases obtained in our study and also previously published data from the phases at pH $\sim$ 2, $\pi = 31$ dyn/cm (ref.

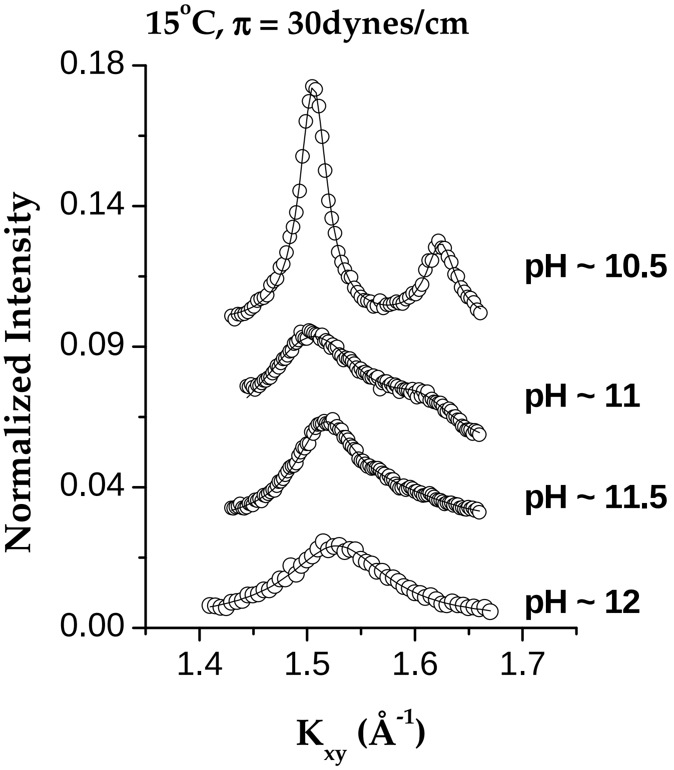

Figure 3.1. Diffracted intensity versus K_{xy}, the in-plane wavevector for a heneicosanoic monolayer at different pH values (at 15 °C and 30 dyn/cm surface pressure). Data were fitted to a superposition of two Lorentzians (solid lines). Scans have been shifted vertically by arbitrary amounts for clarity.

Table 3.1. Lattice Distortion Parameters $\delta = \sqrt{3} - b/a$ and Area Per Molecule ($\mathring{A}^2$) in a Centered Rectangular Basis for C_{21} at 30 dyn/cm as Functions of pH and Temperature[a]

temp	pH	2[2]	10.5	11	11.5	12
9.0				$\delta = 0.203 \pm 0.001$ $A = 19.07 \pm 0.02$ *S*	$\delta = 0.199 \pm 0.001$ $A = 19.07 \pm 0.02$ *S*	
10.0		$\delta = 0.225$ $A = 19.04$ *S*				
12.0		$\delta = 0.213$ $A = 19.10$ *S*		$\delta = 0.182 \pm 0.001$ $A = 19.17 \pm 0.02$ *S*	$\delta = 0.181 \pm 0.002$ $A = 19.16 \pm 0.03$ *S*	
14.0		$\delta = 0.199$ $A = 19.17$ *S*				
15.0			$\delta = 0.170 \pm 0.003$ $A = 19.16 \pm 0.03$ *S*	$\delta = 0.15 \pm 0.01$ $A = 19.34 \pm 0.12$ *Rotator-I*	$\delta = 0.11 \pm 0.02$ $A = 19.2 \pm 0.2$ *Rotator-I*	$\delta = 0$ $A = 19.54 \pm 0.02$ *Rotator-II*
16.0		$\delta = 0.182$ $A = 19.23$ *S*				
17.0		$\delta = 0.169$ $A = 19.31$ *S*				
18.0		$\delta = 0.149$ $A = 19.39$ *Rotator-I*	$\delta = 0.0$ $A = 19.65 \pm 0.02$ *Rotator-II*			
19.0		$\delta = 0.089$ $A = 19.63$ *Rotator-I*				
20.0		$\delta = 0.065$ $A = 19.69$ *Rotator-I*				
22.0		$\delta = 0.0$ $A = 19.73$ *Rotator-II*				

---

[a] The phase of the monolayer is indicated in italics.

[**2**]). The values at pH $\sim$ 10.5 are consistent with an S phase of the monolayer. This phase may be described as a one-dimensional crystal with the backbone planes of the hydrocarbon chains (tails) packed in a herringbone pattern [**73**]. However, a careful comparison shows that the value of δ with pH $\sim$ 10.5 at 15 °C is close to that at pH 2 at 17 °C. This comparison indicates a decrease in the lattice distortion at high pH. On the other hand the area per molecule with pH $\sim$ 10.5 at 15 °C is close to that with pH 2 at 14 °C. Both peaks at pH $\sim$ 10.5 correspond to a correlation length of $\sim$ 70 Å, somewhat less than is usually observed at low pH. At pH $\sim$ 11.0 and pH $\sim$ 11.5, the second peak at around 1.6 Å^{-1} is weakened drastically to the point that it cannot be seen as a maximum at all and we obtain a single, broad asymmetric peak. This result was reproduced on decompression and recompression of the monolayer, and also from a different C_{21} monolayer at the same pH. Following Shih et al.[**2**], this asymmetric peak can be fitted with two Lorentzians and the peak positions assigned to a centered rectangular basis with two molecules per unit cell. The distortion parameter and the area per molecule are given in Table 3.1. The broad peaks produced the larger errors in these parameters, as compared to those at pH $\sim$ 10.5, indicating a more disordered phase of the monolayer. The fwhm for the first Lorentzian, after deconvoluting the horizontal resolution, is about 0.12 Å^{-1} for pH $\sim$ 11 and 0.06 Å^{-1} for pH $\sim$ 11.5 while that of the second Lorentzian is about 0.08 Å^{-1} for pH $\sim$ 11 and 0.15 Å^{-1} for pH $\sim$ 11.5. These

values are quite similar to those of the *Rotator-I* phase observed at 19 °C in C_{21} acid monolayers at pH 2. This phase is formed by a partial disorder in herringbone packing of the backbone planes and is located between the S phase and the regular hexagonal, more disordered *Rotator-II* phase [**2**]. This phase still has a distorted hexagonal lattice, which can be represented equivalently by a centered rectangular lattice, and δ has a small but nonzero value. These phases are named according to analogous phases in lamellar n-parafins [**74**]. The onset of this disordered *Rotator-I* phase with increase in pH is different from the results of the amino acid monolayer where a more ordered two-dimensional crystalline phase formed as the pH was increased [**69**]. At pH ~ 12 we find that the single broad peak has become quite symmetric. It can be fitted with a single Lorentzian (deconvoluted fwhm about 0.113 Å^{-1}), i.e., it corresponds to an undistorted hexagonal lattice. The parameters of this lattice are shown in Table 3.1. This is consistent with completely backbone disordered *Rotator-II* phase observed at 22 °C with pH ~ 2 (ref. [**2**]). The *Rotator-I-Rotator-II* phase boundary has thus been pushed down to at least 15 °C by an increase of pH from 2 to 12. In Figure 3.2 we see the effect of temperature on the monolayer at high pH (11.5). It shows the K_{xy} plots of the diffracted intensity at 9, 12, and 15 °C ($\pi = 30$ dyn/cm). Comparison with the monolayer for pH 2 and at 10 and 12 °C from Table 3.1 shows that the areas per molecule are slightly larger whereas the distortion from the regular hexagonal lattice is

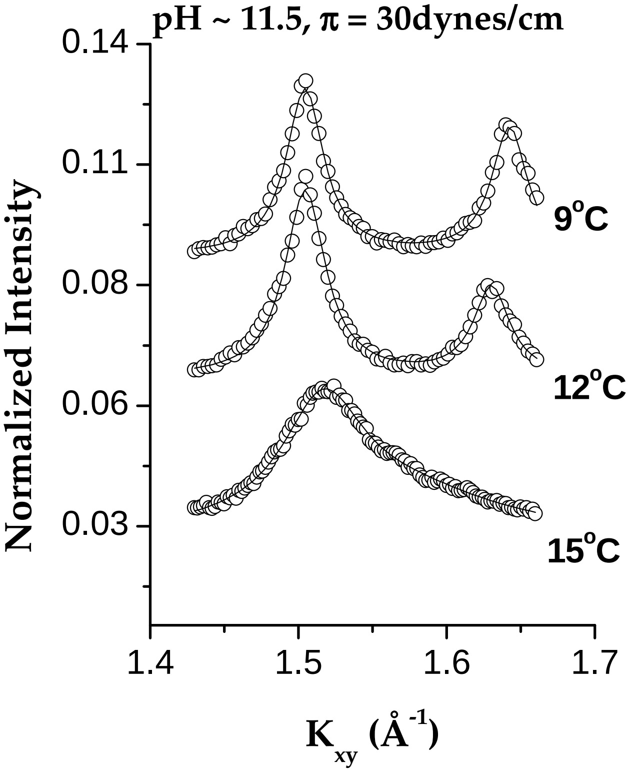

Figure 3.2. Diffracted intensity versus K_{xy}, the in-plane wavevector for a heneicosanoic monolayer at different temperatures (at pH 11.5 and 30 dyn/cm surface pressure). Data were fitted to a superposition of two Lorentzians (solid lines). Scans have been shifted vertically by arbitrary amounts for clarity.

reduced for pH 11.5. At 15 °C we find the *Rotator-I* phase. The *S-Rotator-I* phase boundary at 18 °C for pH 2 has thus been pushed down to at least 15 °C for pH 11.5. From Table 3.1 we see that there is almost no change in the temperature dependence at pH 11.0. For pH 10.5 we collected data at 15 and 18 °C. The *S* phase at 15 °C transforms to a *Rotator-II* phase (a regular hexagonal lattice) at 18 °C (refer to Table 3.1). From the table, it is thus obvious that the *Rotator-II* phase at high pH (10.5) appears at a lower temperature (18 °C) than for pH 2 (22 °C). Figure 3.3 shows the effect of lowering the surface pressure for pH 11.5 and 12 °C. As the pressure is lowered from 30 dyn/cm to 5 dyn/cm the monolayer goes from the *S* phase to a *Rotator-I* phase with a = 4.911Å, b = 8.317Å, a small distortion ($\delta = 0.038$) and a specific molecular area of 20.42 Å^2. This order-disorder transition is again opposite to what is obtained from the amino acid monolayer [**69**] where decreasing pressure creates more order. For measurements at the same pH and pressures at 9 °C, however, we do not see a transition to a *Rotator-I* phase. Lowering the surface pressure retains the *S* phase, and only reduces the distortion (δ goes from 0.197 to 0.183) while the surface area increases from 19.07Å^2 to 19.19Å^2. The *S* and both the *Rotator* phases all consist of untilted (vertical) hydrocarbon chains. This is a preliminary indication that phases of the monolayer with tilted tails are absent at high pH, consistent with studies on fatty acid monolayers in the presence of Ca ions in the subphase [**32**] and on

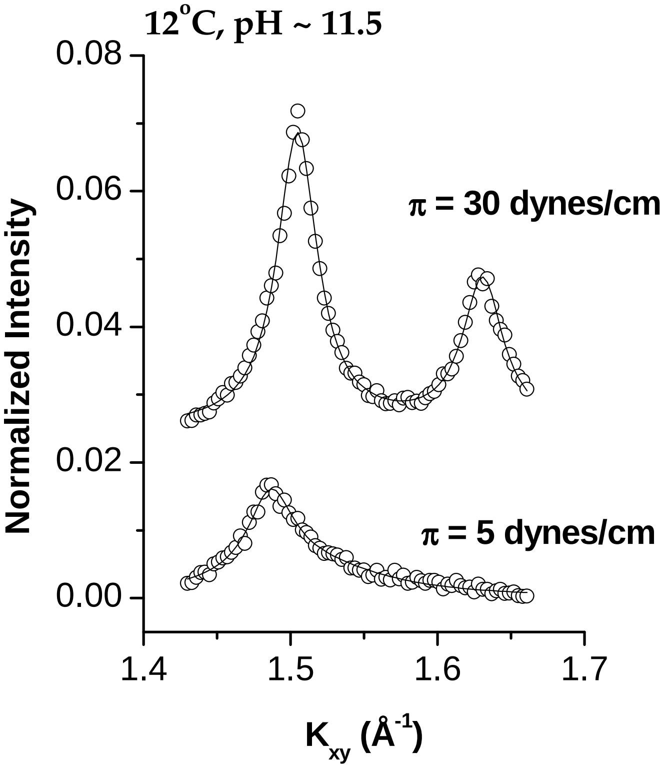

Figure 3.3. Diffracted intensity versus K_{xy}, the in-plane wavevector for a heneicosanoic monolayer at different surface pressures (at pH 11.5 and 12 °C). Data were fitted to a superposition of two Lorentzians (solid lines). Scans have been shifted vertically by arbitrary amounts for clarity.

the amino acid monolayers in the presence of K ions [**69**]. The results presented above show that there are three important effects of increase of subphase pH on monolayer structure, as observed in this work. At a fixed temperature, an increase in pH increases disorder and lowers distortion in the monolayer lattice; the *S* to *Rotator-I* and *Rotator-I* to *Rotator-II* transition temperatures are lowered with the pH increase, and preliminary evidence shows that, with an increase in pH, only those phases with untilted tails are present even at low surface pressure. In general, the *S-Rotator-I* and *Rotator-I-Rotator-II* transitions are brought about by increasing temperature or decreasing length of the tail, both of which would create disorder by affecting the tail-tail interaction. In contrast, increasing the subphase pH seems to create disorder through the dissociation of headgroups and, consequently, changing the head-head interaction. We suggest that this disorder arises out of mixing two types of headgroups (COOH and COO^{-}) at the pH range when the acid is partially dissociated. An increase in the entropy due to mixing may destabilize the monolayer lattice causing an order-disorder transition to take place at a lower temperature. However, an increase in temperature could cause more dissociation in the headgroups as well (as known from bulk weak electrolytes1 [**75**]), and thereby alter the head-head interactions. This consideration, along with the results obtained from this work, suggests that the head-head interaction is at least as significant as that between tails for these high-pressure monolayer phases.

The preliminary evidence about the absence of tilted phases at low surface pressure indicates that at high pH the monolayer behaves as if it is always at high surface pressure. This behavior means that high pH increases the attractive force between headgroups. The attraction between dissociated and undissociated headgroups can be due to hydrogen bonding, as is found in an acid soap. The packing in acid soap crystals is orthorhombic, i.e., having a centered rectangular basis [**76**], and the hydrocarbon chains are almost vertical [**77**]. It has been estimated [**67**] that the *pK* value of fatty acids at the water surface is higher than that in the bulk indicating a lower fraction of dissociated headgroups at a given bulk pH. But this estimate is valid only for large specific molecular areas [**67**], i.e., low surface pressures and low ion density. A situation where densely packed headgroups interact with a layer of Na^+ ions at the air-water interface is difficult to assess without resorting to characterization at the atomic level. However, the results from surface potential measurements suggest that at high pH there is a high degree of counterion binding to the monolayer [**67**], which is relevant to our work. The above considerations of role of head-head interactions, acid soap formation and structure, and disorder due to mixing lead us to suggest that the *Rotator-I* and *Rotator-II* phase formations with increase in pH are related to the formation of a two-dimensional analogue of an acid soap (with in-plane hydrogen bonds between the two kinds of headgroups) from a fatty acid monolayer. At this point we are unable to determine the proportion of acid and soap in the two-dimensional mixture, or the number of acid and soap molecules in the (centered rectangular) unit cell. We have summarized our results and compared them to the results obtained by Shih et al. [**2**] in a phase diagram (Figure 3.4).

3.2. On a dilute salt solution

The mechanical properties of a Langmuir monolayer of long chain fatty acid molecules are changed by the presence of divalent metallic cations in the aqueous subphase. This has been known for some time, and it is also known that the presence of such ions improves transfer of Langmuir-Blodgett (LB) films from the Langmuir monolayer and enhances the crystalline order in those LB films[**4, 30**]. It is therefore worthwhile to learn more about the nature of headgroup interactions in monolayers and how they are affected by metallic cations. Questions remain as to whether such clear categories of Coulomb versus covalent bonding interactions do exist (see section 1.2) and, even if they do, whether a system can be tuned to pass from one to the other. An answer to the first question requires comparative studies of various divalent metals with different values of Pauling electronegativity, especially ones that are close in the electronegativity values. The second involves a way to tune headgroupion interaction for the same ion, and the easiest way available is to change the subphase pH. In this paper, we present results of systematic

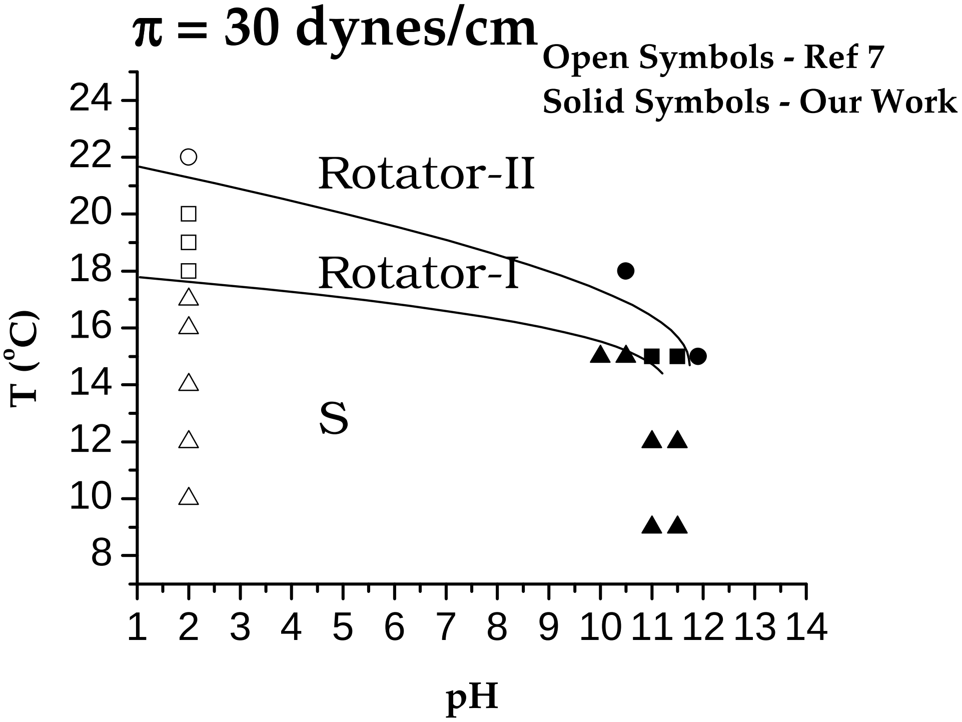

Figure 3.4. Subphase pH vs temperature (°C) phase diagram for heneicosanoic acid Langmuir monolayer as obtained from ref. [**2**] and this work.

GID studies of heneicosanoic acid ($COOH(CH_2)_{19}CH_3$, C_{21} acid) monolayers. The structures of different phases of these monolayers at close to zero surface pressure have been studied with cadmium and zinc, two different divalent metal cations with close values of electronegativity in the subphase, and with variations in subphase pH and temperature.

3.2.1. Experiment details

The salts zinc acetate ($Zn(Ac)_2$, Aldrich, quoted purity 99.999%) and cadmium chloride ($CdCl_2$, Aldrich, quoted purity 99.99+%) were used to produce the ions in the aqueous subphase. All chemicals were used without further purification. About 65 μL of a 0.87 mg/mL solution of C_{21} acid in chloroform was spread. Solutions of the barium and zinc salts with 5×10^{-4} M concentration and solutions of the cadmium salt with 10^{-4} M concentration were used as subphases. Temperature was varied from 9 to 22 °C (±0.1 °C) and the pH from 6 to 9.2 (±0.1). A new monolayer was used for each set of pH and surface pressure measurements. It was allowed to remain at a steady temperature for about 40 min and then compressed to a very small positive surface pressure which will be quoted as ~0 dyn/cm. Surface pressure (π) was measured with (0.5 dyn/cm accuracy. A slight overpressure of helium was maintained in the trough to reduce radiation damage and air scattering.

The monolayers still sustained radiation damage, however, and reproducible data were obtained only during the first 2 h of X-ray exposure.

3.2.2. Results – pH-dependet appearance of chiral structure

3.2.2.1. Variation with pH and temperature. We performed a check of consistency with the results of previous studies[**3**] (using monolayers of $COOH(CH_2)_{18}CH_3$, referred to here as C_{20} acid, with 10^{-3} M $CdCl_2$ in subphase, pH raised to 8.85 with ammonium hydroxide, at 9 °C) as a necessary first step. Unfortunately, we could not reproduce the previously published results with C_{21} acid using the same $CdCl_2$ concentration, with the pH raised to the prescribed value either with ammonium or sodium hydroxide, anywhere between 7 and 12 °C, but obtained a single, broad peak only. On the other hand, we could reproduce those results very closely when the concentration of the ions was 10^{-4} M, and we found that raising the pH by sodium or ammonium hydroxide gives identical diffraction patterns. We have therefore used this lower concentration for all measurements on $CdCl_2$ reported here, and used NaOH throughout to raise pH. The diffraction pattern was essentially invariant over a pH range of ∼7 to ∼9. In Figure 3.5 we show a typical wide K_{xy} scan taken at K_z) 0 for a pH value of 8.5. We see the strong triplet in the K_{xy} range of 1.45-1.70 Å^{-1} and the weak peaks at lower values of K_{xy} (0.65-1.45 Å^{-1}), just as has been reported with C_{20} acid [**32**]. Our assignment of $\{h, k\}$ indices to the

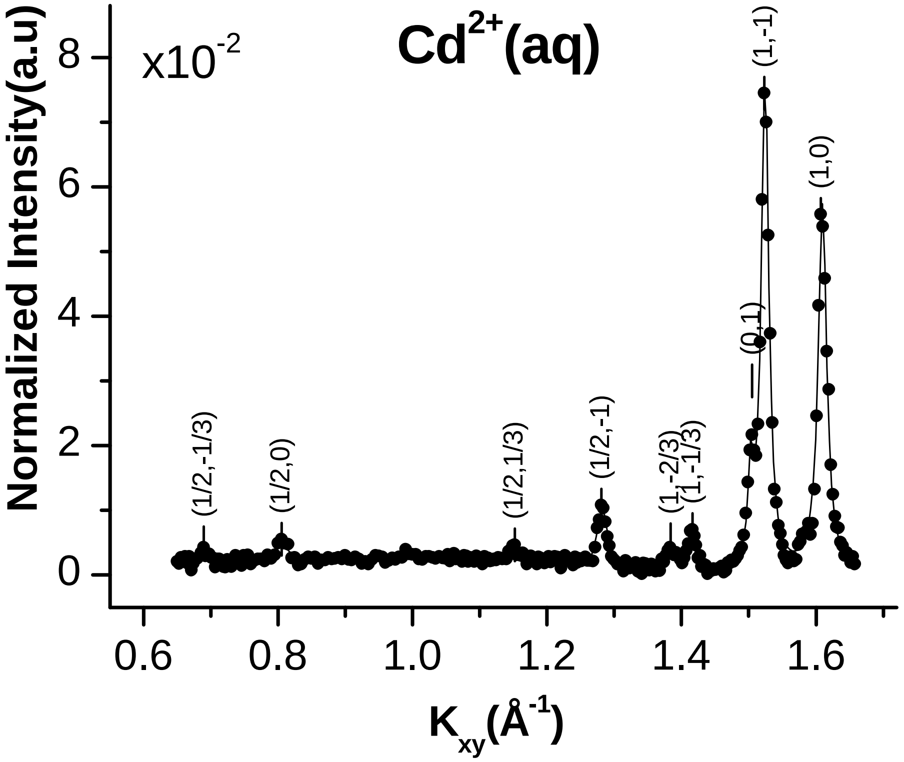

Figure 3.5. Normalized diffracted intensity (arbitrary units) versus K_{xy}, the in-plane component of momentum transfer vector (Å^{-1}), for a heneicosanoic acid Langmuir monolayer at 9.2 °C and ∼0 dyn/cm surface pressure, with 10^{-4} M $CdCl_2$ in the subphase and pH raised to 8.5 with NaOH. Data taken at $K_z = 0$. Peaks are indexed following the assignment described in text. These data are essentially identical to those reported in ref [**3**].

K_{xy} positions of these peaks follows that of ref [**3**] and are indicated in Figure 3.5. The primitive unit cell is oblique (corresponding to an asymmetrically distorted hexagonal or chiral lattice) with lattice parameters $a' = 4.56$Å, $b' = 4.89$Å, and $\gamma = 121.6\,°$C, while the peaks with the fractional indices gave a 2×3 superlattice of this oblique cell. Since two peaks of the triplet are nearly degenerate, we could determine an equivalent centered pseudo-rectangular unit cell (with two molecules per unit cell) through the transformations, $a = 2a' + b'$, $b = b'$. The values of the lattice parameters a, b, and A, the area per molecule in the horizontal plane (water surface) are given in Table 3.2. Since the headgroups always lie on this plane, A is the area per headgroup. The angle between a and b is 89.2 °C. In Figure 3.6a we show the intensity contours of a typical weak diffraction peak ('superlattice peak') from the scan of Figure 3.5 as a function of K_{xy} and K_z, while Figure 3.6b shows the contours for the strong triplet from the same scan. It is seen that the superlattice peak has its maximum at $K_z = 0$. Except for the contribution due to refraction close to the water surface from the maxima of the Vineyard function[**78**] at and near $K_z = 0$, all three peaks of the triplet are out-of-plane and all have sharp K_z maxima. Fits of the K_{xy} peaks with Lorentzian functions and the K_z peaks with Gaussian functions[**79**] gave the peak positions and widths. The peak positions were then used to obtain the tilt θ of the hydrocarbon chains from the vertical, the azimuth ϕ of the tilt, the area A' per molecule in the plane normal

Table 3.2. Variation of Structural Parameters with pH and Temperature[a]

$T(^\circ\mathrm{C})$	pH	$a(\text{Å})$	$b(\text{Å})$	$A(\text{Å}^2)$	$A'(\text{Å})$	ξ	$\theta(deg)$	ϕ
9.2	6.2	8.70	4.83	21.02	19.45	0.04	22	NN
9.2	8.5	7.77	4.89	19.00	18.75	0.09	8	~NNN
9.2	9.3	7.45	5.00	18.64	18.64	0.15	0	
18.0	8.5	7.83	4.86	19.02	19.02	0.07	0	
22.0	8.5	7.99	4.80	19.18	19.18	0.04	0	

[a] For C_{21} acid monolayer spread on $CdCl_2$ (10^{-4} M) in subphase at ~0 dyn/cm surface pressure. The lattice parameters a and b refer to a centered rectangular cell with two molecules per unit cell. A designates the area per molecule in the horizontal plane (area per headgroup) and A' designates the area per molecule in the plane normal to the hydrocarbon chains (area per chain). The distortion magnitude ξ is defined in ref (see text), θ is the tilt angle, and ϕ is the tilt azimuth (NN = nearest and NNN = next nearest neighbor).

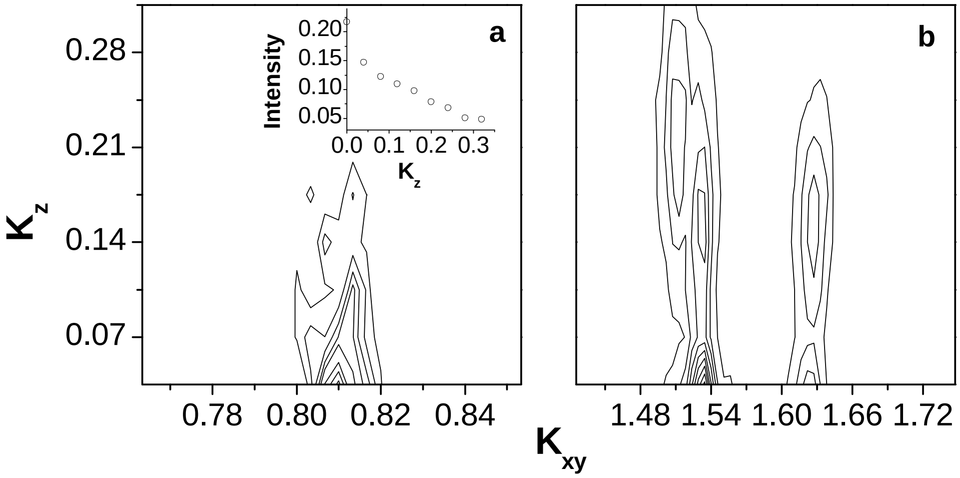

Figure 3.6. Intensity contours (arbitrary units) in the K_z/K_{xy} plane for the monolayer described in Figure 3.5: (a) a weak superlattice peak and (b) a strong triplet. K_z profile (Bragg rod) at the superlattice peak is shown in the inset.

to the chains, and ξ the distortion magnitude, following Kaganer et al.[**60**], where $\xi = (\alpha^2 - \beta^2)/(\alpha^2 + \beta^2)$, α and β being respectively the major and minor axes of the ellipse that passes through all six nearest neighbors of a given molecule. These values are given in Table3.2. The chains are found to be tilted almost along the longer (b) axis of the centered pseudo-rectangular unit cell, as also observed with C_{20} acid[**3**]. The amount of tilt, however, is less in C_{21} acid (it was about 11 °C for C_{20} acid). From fwhms of the K_z peaks fitted with a Gaussian function, we obtained, using Scherrers formula, an estimate of the thickness of the monolayer corresponding to the K_z profile (thickness= $0.9 \times 2\pi/fwhm$)[**27**]. For the triplet peaks, the thickness comes out to be ∼29 Å, consistent with the d-spacing in bulk crystals of fatty acid cadmium salts[**71**], while the "superlattice peak" (K_z profile along the K_{xy} peak shown in Figure 3.6a (inset)) appears to come from a layer of thickness ∼10 Å, which is about 4 times thicker than estimated for a monolayer of $CdOH^+$. Below and above the pH window 7-9, the monolayer underwent major structural changes as reflected in the three in plane ($K_z = 0$) scans shown in Figure 3.7. All scans were performed at 9.2 °C with $CdCl_2$ (10^{-4} M) in the subphase. Figure 3.7 (top) depicts the K_{xy} scan when no NaOH was added to the subphase to raise the pH. The pH of this subphase was measured to be ∼6.2, i.e., below the pH window. No superlattice peaks were observed. The K_z/K_{xy} contour plot of the scanned region in Figure 3.7 (top) is shown in Figure 3.8a. It shows an in-plane

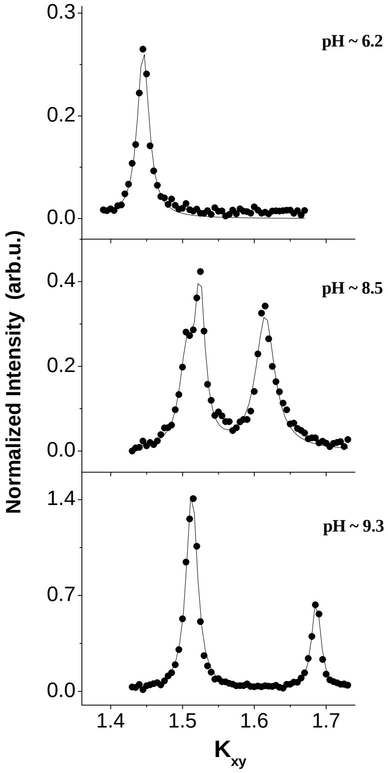

Figure 3.7. Normalized diffracted intensity (arbitrary units) versus K_{xy} for a heneicosanoic acid Langmuir monolayer at $\sim 9.2\,°\mathrm{C}$ and ~0 dyn/cm surface pressure, with 10^{-4} M $\mathrm{CdCl_2}$ in the subphase and different values of pH. Data taken at $K_z = 0$.

and an out-of-plane peak, and by fitting these peaks to obtain the K_z and K_{xy} positions we found the structural parameters for this phase (see Table 3.2). There is a centered rectangular unit cell (with two molecules per unit cell) with chains tilted toward a nearest neighbor by an angle of about 22.3 °C from the vertical. The lattice spacings are almost identical to those of the L_2 phase seen previously in monolayers of the pure acid[**79**]. This indicates that there is negligible interaction between the headgroups and the ions below the pH window. Figure 3.7 (middle) shows the monolayer within the window and we have already discussed the structure of this phase with its pseudo-rectangular cell and superlattice peaks (not shown in this figure). Figure 3.7 (bottom) shows the diffraction pattern from the monolayer above the window (pH ∼9.3). Only two peaks were observed between 0.65 and 1.7 Å^{-1} in K_{xy} which are shown in the scan. Both peaks were found to be in-plane, i.e., with maximum intensity at $K_z = 0$. Structural parameters are given in Table 3.2. This is again a centered rectangular unit cell (with two molecules per unit cell) with untilted chains which is very similar to the S phase observed in monolayers of pure C_{21} acid at the same temperature but at a much higher pressure of > 30 dyn/cm [**2**]. This similarity indicates an isotropic attractive force due to the divalent ions that compresses the organic monolayer. To check out the possibility that, at high values of subphase pH, the change in structure is due to the sodium hydroxide used to raise the pH rather than to any change in the

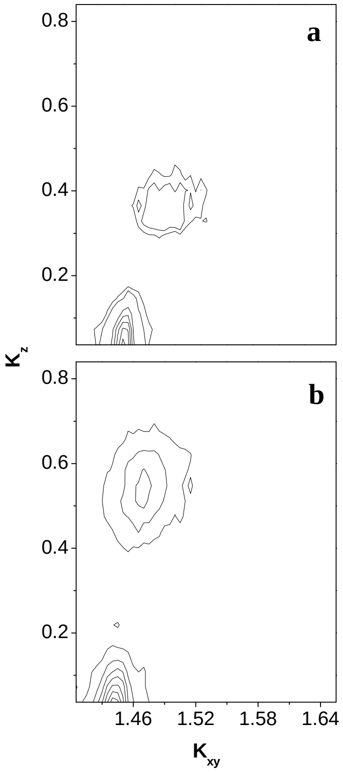

Figure 3.8. Intensity contours (arbitrary units) in the K_z/K_{xy} plane for (a) the monolayer described in Figure 3.7 (top), pH ∼6.2, and (b) a heneicosanoic acid monolayer with no divalent ions in the subphase but with pH raised to 9.3 by NaOH.

headgroup-cadmium ion interactions, we performed diffraction scans on a C_{21} acid monolayer with no $CdCl_2$ in the subphase but the pH raised to 9.3 by NaOH, at 9.2 °C and ∼0 dyn/cm surface pressure. Figure 3.8b shows the K_z/K_{xy} contour plot of the two peaks observed. They are almost identical to those in Figure 3.8. From an analysis of the peaks in Figure 3.8b we obtained a centered rectangular lattice for the monolayer (two molecules per unit cell) with $a = 8.75\text{Å}$, $b = 4.92\text{Å}$, $A = 21.50\text{Å}^2$, the chains tilted toward nearest neighbors by an angle of 21.9 °C from the vertical, and $A' = 19.95\text{Å}^2$, which are very similar to what was found for the monolayer with $CdCl_2$ in the subphase but no NaOH (Figure 3.8a and Table 3.2). We have already seen that the structure is similar to that of a pure C_{21} acid monolayer at ∼ 10 °C and ∼0 dyn/cm pressure[**79**]. Hence, we can conclude that the change in monolayer structure observed above the pH window is not due to sodium hydroxide at high pH but due to a discrete change in the nature of the headgroup-cadmium ion interaction. Table 3.2 shows that A decreases and ξ increases when the pH rises above the window from the respective values within the window. There are two possible processes which could account for the effect of pH on the interactions between the headgroups and ions. The first is that as the pH is raised, acid molecules are converted to soaps (salts). The fraction of cadmium soap to acid in transferred (LB) films has been found[**80**] to increase linearly from 0 to 1 over the pH range 4.8-6.5. In our Langmuir monolayer, however, these values fall below the pH window where interactions between the headgroups and ions do not play a significant role. The process of deprotonation and conversion of acid to soap does not explain the structural changes at high pH that occur after the organic monolayer is saturated with the soap. The second possibility is that as the pH is raised, aqueous ions undergo hydrolysis and specific soluble hydroxide complexes may be formed. It is difficult to predict what particular hydroxide species of cadmium forms directly under the organic monolayer since the concentration and pH at the interface are unknown. However, it may be the interaction with a particular species of cadmium hydroxide complex (for example $\mathrm{Cd_4(OH)_4^{4+}(aq)}$ which is dominant at high concentration of $\mathrm{Cd^{2+}(aq)}$ and pH range 8-12)[**81**] that forces the organic monolayer into a chiral structure. Different species of cadmium hydroxide dominate at different pH values[**81**], so the process of hydrolysis may explain the fact that the monolayer goes through a series of structures as the pH is raised. The effects of increasing pH are both acid to soap conversion and hydrolysis. To study the effect of each process on the structure of the organic monolayer, we dissolved a comparatively large amount of sodium chloride in addition to cadmium chloride in the subphase and increased the pH to 9.3. Sodium monovalent cations might be expected to screen the negatively charged headgroups and reduce the ratio of acid to cadmium soap. We observed no change. The film was found in the same high pH phase as without sodium. Alkali group I elements do not hydrate well as opposed to cadmium which can form many hydrolysis products[**81**]. This lends support to the possibility that there is a type of "hydration bridge" between the heads and cadmium ions within a specific pH range. It is interesting to compare the effects of pH to the effects of temperature6 on the headgroup-ion interaction in Langmuir monolayers. In particular, we were interested in the effect of raising temperature on a monolayer within the pH window. Figure 3.9 shows the in-plane diffraction scans on a monolayer of C_{21} acid with 10^{-4} M $CdCl_2$ in the subphase, the pH raised to 8.5 by NaOH, pressure ∼0 dyn/cm and temperatures ranging from 15 to 22 °C. The monolayer was found to be essentially unchanged from 9 to 15 °C, as is evident from a comparison of Figure 3.9 (top) (15 °C) with Figure 3.7 (middle) (9.2 °C). Along with this characteristic triplet we also found all the superlattice peaks at 15 °C (not shown in the figure). At 18 °C (Figure 3.9 (middle)) we found two broad, in-plane peaks and no peaks anywhere else. However, the data were not very reproducible at this temperature and we would sometimes start with a pattern as in Figure 3.9 (top) which changed rapidly, in subsequent scans, to the situation in Figure 3.9 (middle). This is probably due to hysteresis at a first-order transition. At 22 °C, the monolayer exhibited a stable and reproducible diffraction pattern (Figure 3.9 (bottom)). Only one broad, asymmetric in-plane peak was observed over the whole region from 0.7 to 1.7 Å^{-1} (see Table 3.2). This structure

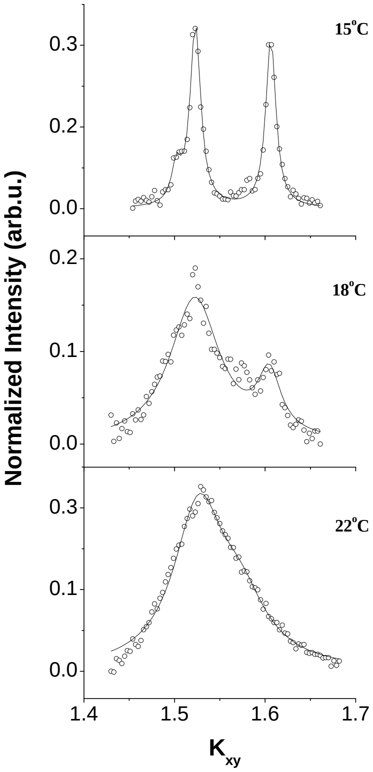

Figure 3.9. Normalized diffracted Intensity (arbitrary units) versus K_{xy} for a heneicosanoic acid Langmuir monolayer at pH ∼8.5 and ∼0 dyn/ cm surface pressure, with 10^{-4} M $CdCl_2$ in the subphase and different temperatures. Data taken at $K_z = 0$.

is very similar to that of the high-temperature Rotator-I phase of pure C_{21} monolayers at around 20 °C (ref [**82**]). This phase is formed by a partial disorder in the orientations of the chain backbone planes[**27**]. The effect of the cadmium ions is only to lower the effective temperature of the monolayer so that a monolayer with cadmium ions at 22 °C has the structure of a monolayer without the ions at 20 °C. In order to understand better the effects of pH and temperature on the molecules in a monolayer we estimated the (percentile) changes in the area per headgroup (A) and area per chain (A') with increasing pH and increasing temperature. These changes are compared in Table 3.3. From this table we see that, with increase in pH, the reduction in area per headgroup is consider-ably more than the reduction in area per chain. This preferential reduction indicates that increase in pH acts as an attractive interaction and affects the headgroups more than the chains. On the other hand, when temperature is increased, the increase in area per headgroup is less than the increase in area per chain, indicating that temperature affects the chain-chain interactions more than it affects the headgroups. The fact that an increase of pH contracts and an increase of temperature expands the monolayer lattice contrasts with the case of monovalent cations, where the effect of raising pH was seen to be similar to that of raising temperature[**31**].

3.2.2.2. Comparison with Zn ions. The nature of interaction of metal ions with acids is known to be correlated with the Pauling electronegativity of the metal

Table 3.3. Changes in the Areas Per Headgroup and Per Chain[a]

	pH(temp=9.2 °C)			temp(pH=8.5)		
	6.2	8.5	9.3	9.2 °C	18.0 °C	22.0 °C
$\Delta A(\%)$		-9.6	-11.32		0.11	0.95
$\Delta A'(\%)$		-3.6	-5.62		1.44	2.29

[a] For pH, the change is with respect to pH ∼6.2. For temperature, the change is with respect to 9.2 °C.

[**6, 27, 83**]. Metals with low electronegativity tend to form electrovalent bonds, i.e., interact through Coulomb attraction, while for metals with higher electronegativities the bond acquires an increasingly covalent character and the interaction becomes dominated by exchange forces. Cadmium is a metal with an intermediate value (1.69) on the Pauling electronegativity scale and it is expected to form partially covalent (polar) bonds with the headgroups in a fatty acid monolayer. The effect of only one other metal ion, calcium, on a fatty acid monolayer has been studied so far with GID [**32**]. Calcium is a metal with a low electronegativity (1.00) and, on comparing the previous work on calcium with our results, we find that it affects the monolayer in a way similar to what is observed with cadmium ions above the pH window. In order to gain a better correlation of the nature of headgroup-metal ion interactions with the electronegativity of the divalent metal, we performed GID studies on the effect of another divalent metal ion on C_{21} acid monolayers under conditions similar to those for cadmium. We chose zinc which has the electronegativity value of 1.65, close to but less than the electronegativity value of cadmium, and belongs to the same group (IIB). Zinc is also interesting for its two somewhat anomalous properties. First, the area per molecule of zinc fatty acid salts in LB films is too large to be correlated with its electronegativity[**6**]. Second, the first few monolayers have a hexatic structure before subsequent monolayers form the "bulk" crystal structure[**84**]. The in-plane positional correlations were observed to be short-range, but with long-range bond-orientational order. Those observations suggest that the intermolecular interactions of fatty acid salts of zinc are much weaker than of salts of cadmium in LB films. Figure 3.10a shows the scan for the monolayer with $CdCl_2$ in the subphase at pH ∼9.3. Figure 3.10b shows the scan for the monolayer with $Zn(Ac)_2 2$ in the subphase at pH ∼7.0, the maximum pH that can be reached before the monolayer becomes unstable, 10 °C, and the low pressure of ∼3 dyn/cm. Only these two in-plane peaks were observed for the entire scan range of 0.6-1.7 Å^{-1} and, except for slight shifts in the peak positions, no essential change in the diffraction pattern was observed in the pH range from ∼5 to 7. What is more important is that there were no superlattice peaks at low K_z, and the observed peaks were always in-plane. Analysis of the data in Figure 3.10b gave the structure of the monolayer to be composed of centered rectangular cells (two molecules per cell) with untilted chains. The structural parameters are presented in Table 3.4. The area per headgroup is only slightly smaller for a monolayer with cadmium than with zinc, but the lattice parameters are significantly different between the two ions. In general, parameters of the unit cell can vary such that the packing of hydrocarbon chains can be found between two modes of arrangement: herringbone (HB) and pseudoherringbone (PHB)[**27**]. The rectangular unit cell dimensions of 5.0Å × 7.5Å for cadmium are a fingerprint of the HB pattern whereas the dimensions 4.1Å × 9.2Å for zinc are close to that for

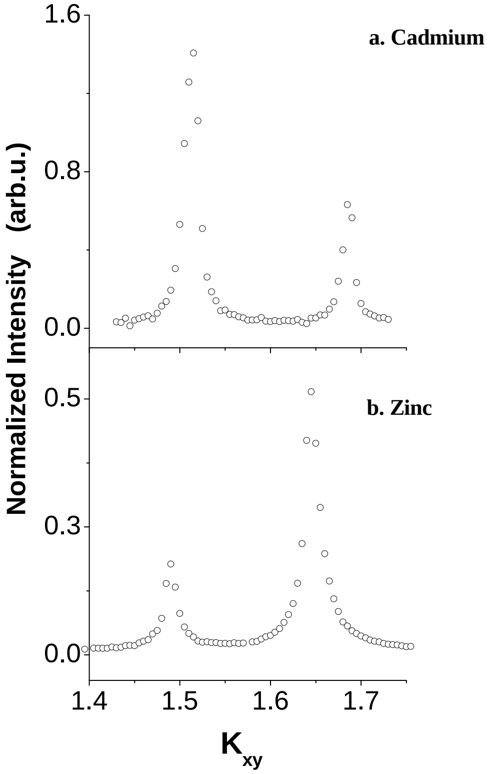

Figure 3.10. Normalized diffracted Intensity (arbitrary units) versus K_{xy} for a heneicosanoic acid Langmuir monolayer with (a) 10^{-4}M $CdCl_2$ at $\sim 9.2\,°C$ and $\sim$0 dyn/cm surface pressure, pH $\sim$ 9.3; (b) 5×10^{-4}M $Zn(Ac)_2$ at $\sim 10\,°C$ and $\sim$3 dyn/cm surface pressure, pH $\sim$ 7.0.

Table 3.4. Comparison of Structural Parameters with Different Ions in the Subphase

salt	conc(M)	pH	temp ($^\circ$C)	π (dyn/cm)	a(Å)	b(Å)	A(Å^2)	ξ	electronegativity
$Zn(Ac)_2$	5×10^{-4}	5-7	10	$\sim$3	9.22	4.08	18.80	0.26	1.65
$CdCl_2$	1×10^{-4}	> 9	9.2	$\sim$0	7.45	5.00	18.64	0.15	1.69

PHB packing. The PHB packing mode has a lower packing density than that of the HB structure. The PHB packing mode of the monolayer with zinc, therefore, may explain the lower in-plane cohesion as well as lower packing density in LB films of zinc fatty acid salts as opposed to cadmium salts. Table 3.4 also indicates that (a) the nature of headgroupdivalent ion interaction in a monolayer with cadmium ions in the subphase and above the pH window is similar to the interaction in a monolayer with zinc ions (with electronegativity value very close but lower than that of cadmium) in the subphase, under comparable external conditions; and (b) the strength of the attractive interaction, estimated from the area per headgroup, is lower for zinc than for cadmium.

CHAPTER 4

Effects of divalent ions: superlattices

4.1. Superlattice with lead salt in the subphase

The properties of an organic amphiphilic monolayer floating at the air-water interface can change significantly when metal ions are added to the subphase. With a cadmium salt dissolved in the subphase, formation of a monolayer lattice in the subphase has been observed using X-ray diffraction[**85, 55**]. Since the superlattice is seen only in the presence of subphase Cd_2^+ ions, it is tempting to conclude [**85, 55**] that the superlattice must be an ordered array of Cd_2^+ ions. However, there is no chemically specific evidence of the composition of the superlattice, and the unit cell is quite large (a 2 × 3 supercell of the Langmuir monolayer unit cell).We sought to learn more about this initial stage of bulk inorganic nucleation by studying fatty acid Langmuir films with Pb_2^+ ions in the subphase, using X-ray scattering. Lead is a heavy atom that scatters X-rays strongly and (unlike cadmium) has an experimentally accessible (L3) absorption edge; this latter fact allowed us to perform anomalous X-ray scattering studies that directly test for the presence of lead in the superlattice.

4.1.1. Experimental details

A dilute aqueous solution containing 10^{-5} M lead chloride (Sigma, quoted purity 99.999%) was dissolved in the subphase whose pH was not adjusted and measured to be ∼5.5. About 65 μL of a 0.87 mg/mL solution of heneicosanoic acid ($C_{20}H_{41}COOH$ or C_{21}, Sigma, quoted purity 99%) in chloroform was spread at the air-solution interface of the subphase. C_{21} is a saturated straight-chain molecule; its chemical diagram is given in ref [**27**], Figure 1a. The phase diagram of pure C_{21} is well known[**27**], so effects due to the lead ion can be easily discerned. A mechanical barrier compressed the monolayer to a pressure of about 0.5 dynes/cm (i.e., essentially zero pressure) at 10 °C, and the film was left to equilibrate for an hour. All scans were performed at constant pressure, at about 0.5 dynes/cm. Surface pressure (π) was measured with ∼0.2 dyn/cm accuracy. A slight overpressure of helium was maintained in the trough to reduce radiation damage and air scattering. To reduce radiation damage further, fresh subphase solution and monolayer were prepared after an hour of X-ray exposure.

4.1.2. Results – diffraction and anomalous scattering

In-plane diffraction scans revealed a total of 39 distinct peaks (Figure 4.1). This observation is qualitatively similar to that reported in ref [**85**] (in the presence

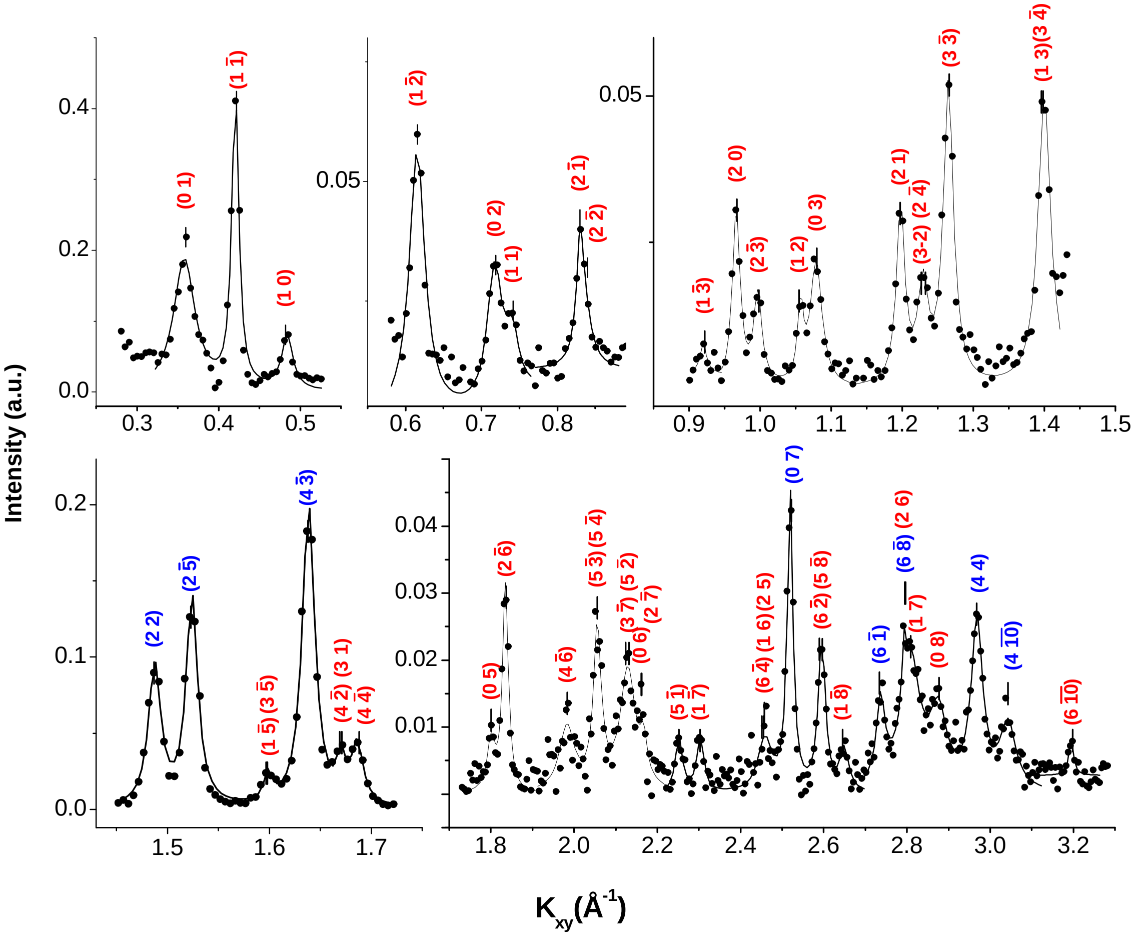

Figure 4.1. Grazing incidence synchrotron X-ray diffraction data from a heneicosanoic acid Langmuir monolayer with lead ions in the subphase. The lower-order peaks (2 2), (2 $\bar{5}$), and (4 $\bar{3}$) correspond to the reciprocal lattice of the Langmuir monolayer (this identification is made from Bragg rod scans; see Figure 4.2). The higher-order peaks (0 7), (6 $\bar{1}$), (6 $\bar{8}$), (4 4), and (4 $\bar{10}$) are also from the Langmuir monolayer. All other peaks are due to the superlattice.

of subphase Cd^{2+}), but there are many more peaks and the peak positions are different. The lowest observed peak is at 0.36 Å^{-1}, indicating the appearance of a much larger unit cell than that of a Langmuir monolayer.There are three relatively strong peaks in the K_{xy} region of ∼1.5 Å^{-1}, indexed[1] (2 2), (2 $\bar{5}$), and (4 $\bar{3}$) and so labeled in Figure 4.1 and marked in bold in Table 4.1. We performed scans along the Bragg rods at these peaks (i.e., we measured the scattered intensity above background as a function of K_z with K_{xy} held constant at the peak positions). The width of a Bragg rod is inversely proportional to the thickness of the monolayer[**27**]; specifically, the intensity profile along K_z can be approximated[**21**] by $I_{hk}(K_z) \approx I_0(\sin W/W)^2$ where $W = 1/2LK_z$ and L is the thickness. Fits to the Bragg rods of any of the three strong peaks (Figure 4.2b) yielded a thickness of 27 Å(Table 4.2), consistent with the length of the heneicosanoic acid molecule. This confirms that these strong peaks are primarily due to the packing of fatty acid molecules. In addition, the intensity maxima along the Bragg rods are at or near $K_z = 0$, which means that the acid molecules are untilted (normal to the plane of the interface). These diffraction peaks indicate an oblique unit cell with dimensions $a = 4.52$ Å, $b = 4.99$ Å, $\gamma = 121.9\,^{\circ}\text{C}$, and an area of 19.15Å^2, with

---

[1] We used a basis that results in integer (hk) for all peaks; if we had indexed in terms of the triangular lattice of the Langmuir monolayer, these peaks would have been (0 1), (1 $\bar{1}$), and (1 0), respectively

Table 4.1. Observed In-Plane Positions of Bragg Peaks in the GID Pattern[a]

		K_{xy}(Å^{-1})				K_{xy}(Å^{-1})				K_{xy}(Å^{-1})				K_{xy}(Å^{-1})	
h	*k*	calculated	observed	*h*	*k*	calculated	observed	*h*	*k*	calculated	observed	*h*	*k*	calculated	observed
0	1	0.3597	0.360	3	$\bar{2}$	1.2292	1.229	2	$\bar{6}$	1.8344	1.835	5	$\bar{8}$	2.5893	2.593
1	$\bar{1}$	0.4217	0.422	2	$\bar{4}$	1.2332		4	$\bar{6}$	1.9866	1.986	6	$\bar{2}$	2.5925	
1	0	0.4840	0.484	3	$\bar{3}$	1.2651	1.263	5	$\bar{4}$	2.0519	2.052	1	$\bar{8}$	2.6511	2.649
1	$\bar{2}$	0.6166	0.616	3	$\bar{4}$	1.3960	1.399	5	$\bar{3}$	2.0576		**6**	**$\bar{1}$**	**2.7291**	**2.730**
0	2	0.7194	0.719	1	3	1.3986		5	$\bar{2}$	2.1251	2.128	**6**	**$\bar{8}$**	2.7919	**2.794**
1	1	0.7412	0.742	**2**	**2**	**1.4825**	**1.484**	3	$\bar{7}$	2.1322		2	6	2.7972	
2	$\bar{1}$	0.8335	0.833	**2**	**$\bar{5}$**	**1.5210**	**1.521**	0	6	2.1582	2.161	1	7	2.8062	
2	$\bar{2}$	0.8434		1	$\bar{5}$	1.5937	1.598	2	$\bar{7}$	2.1623		**4**	**4**	**2.9650**	**2.962**
1	$\bar{3}$	0.9172	0.920	3	$\bar{5}$	1.5987		5	$\bar{1}$	2.2487	2.252	**4**	**$\overline{10}$**	**3.0421**	**3.042**
2	0	0.9680	0.967	**4**	**$\bar{3}$**	**1.6379**	**1.637**	1	$\bar{7}$	2.2964	2.299	6	$\overline{10}$	3.1974	3.196
2	$\bar{3}$	0.9933	0.993	4	$\bar{2}$	1.6671	1.667	1	6	2.4509	2.457				
1	2	1.0599	1.058	3	1	1.6719		2	5	2.4555					
0	3	1.0791	1.079	4	$\bar{4}$	1.6868	1.686	6	$\bar{4}$	2.4584					
2	1	1.1992	1.199	0	5	1.7985	1.800	**0**	**7**	**2.5179**	**2.521**				

[a] There are 39 distinct peaks in the in-plane diffraction pattern, and they are listed under the "observed" column. Bold labels indicate positions of peaks primarily due to the organic film. Some peak positions are so close to each other that they cannot be distinguished as separate peaks in our data, Figure 4.1 (note that the monolayers are powders in the plane). Studies of multiple films gave peak positions reproducible to ~ 0.002 Å^{-1}. The "calculated" column contains peaks calculated from the magnitudes of the (0 1), (1 $\bar{1}$), and (1 0) basis vectors; these magnitudes were refined by maximizing the overall agreement between all calculated and observed peaks.

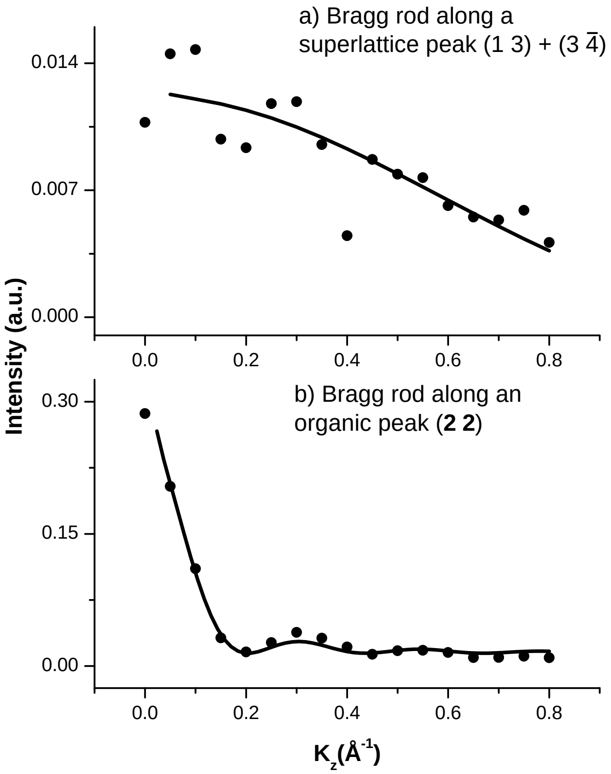

Figure 4.2. (a) Bragg rod scan of a representative in-plane peak along a superlattice “inorganic” peak (1 3) + (3 $\bar{4}$). We have obtained similar Bragg rod scans at other superlattice peaks: (0 2), (1 1), (1 $\bar{5}$) + (3 $\bar{5}$), and (4 $\bar{2}$) + (3 1). (b) Bragg rod scan of a representative in-plane peak along a peak due to the organic monolayer (2 2). We have obtained similar Bragg rod scans at the other two low-order “organic” peaks: (2 $\bar{5}$) and (4 $\bar{3}$). The intensities fall off more sharply in (b), indicating that the peak originates from a thicker film (~27 Å) compared to the Bragg rod in (a), which indicates a thickness of ~5 Å.

Table 4.2. Thickness Calculated from Fits to Bragg Rods[a]

hk	thickness(Å)	hk	thickness(Å)
(0 2)	4.8	**(2 $\bar{5}$)**	**27**
(1 1)	4.9	(1 $\bar{5}$)+(3 $\bar{5}$)	3.6
(1 3)+(3 $\bar{4}$)	4.9	**(4 $\bar{3}$)**	**27**
(2 2)	**27**	(4 $\bar{2}$) + (3 1)	2.5

[a] Bragg rods along these seven peaks were fitted with $I_{hk}(K_z) \approx I_0(\sin W/W)^2$ where $W = 1/2LK_z$ and L is the thickness. The organic peaks (shown in bold) indicate a thickness of 27 Å, consistent with the length of the molecule. Bragg rods for the five "inorganic" peaks studied yield a much smaller layer thickness, ∼5 Å or less.

one organic molecule per unit cell[2]. There are also five relatively strong peaks in the region $K_{xy} > 2.5\text{Å}^{-1}$, indexed (0 7), (6 $\bar{1}$), (6 $\bar{8}$), (4 4), and (4 $\bar{1}$0), that are higher order diffraction peaks from the same structure[3] (these are also marked in bold in Table 4.1). The Bragg rods along the remaining peaks (Figure 4.2a, Table 4.2) are consistently much wider than those along the three strong peaks (Figure 4.2b), which means that these peaks are from a much thinner layer (thickness ~5 Å). These weak in-plane reflections correspond to a superstructure with cell dimensions $a' = 15.35$ Å, $b' = 20.66$ Å, $\gamma = 122.25\,°\text{C}$, and an area of 268.1 Å^2. These parameters were refined by maximizing the overall agreement between all calculated and observed peaks. Since the area of the supercell is exactly 14 times that of the organic unit cell and since the organic lattice peaks are also peaks of the superlattice (i.e., a common indexing scheme can be employed), the two lattices must be commensurate. A schematic representation of the organic cell and the supercell in real space is shown in Figure 4.3. The relative orientation of the two lattices is determined by the fact that this is the only way they can be commensurate: the shortest real-space basis vectors of the organic cell ($\mathbf{a}$, $\mathbf{b}$) and inorganic cell ($\mathbf{a}'$, $\mathbf{b}'$) are related by the vector identities $\mathbf{a}' = 4\mathbf{a} + 2\mathbf{b}$

---

[2] The nonprimitive cell with two organic molecules, normally centered-rectangular (ref [**27**]), is a parallelogram in the presence of lead ions.

[3] In terms of the alternate indexing system mentioned earlier (footnote 1), these would have been (1 $\bar{2}$), (1 1), (2 $\bar{1}$), (0 2) and (2 $\bar{2}$), respectively

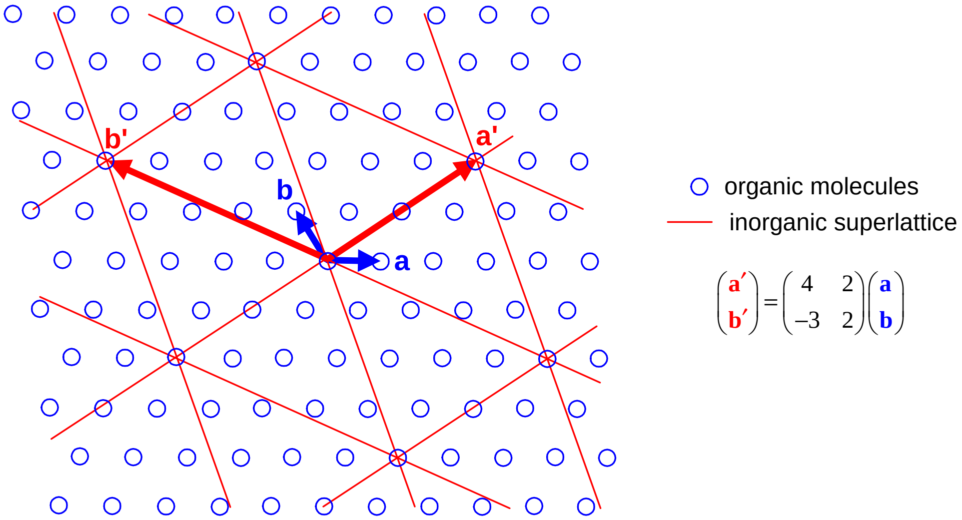

Figure 4.3. Real space lattices of the fatty acid monolayer and the superlattice. The heneicosanoic acid molecules are represented by circles; the lattice parameters are a = 4.52 Å, b = 4.99 Å, and γ = 121.9 °C, so that area=19.15 Å^2. The superstructure is shown by lines; the lattice parameters are a' = 15.35 Å, b' = 20.66 Å, γ' = 122.25 °C, and area$'$ = 268.1 Å^2. The lattices are commensurate: the basis vectors are related through $\mathbf{a}' = 4\mathbf{a} + 2\mathbf{b}$ and $\mathbf{b}' = -3\mathbf{a} + 2\mathbf{b}$, so that area$'$ = 14× area.

and $\mathbf{b}' = -3\mathbf{a} + 2\mathbf{b}$. Although we have observed and indexed a large number of diffraction peaks, these peaks do not tell us the type and arrangement of atoms within a single supercell. A determination of even a crude trial-and-error supercell structure from peak intensities would require some knowledge of its atomic composition. Rather than simply assuming that the lattice is an array of lead ions (cf. refs [**85**] and [**55**]), we sought to test for the presence of lead within the superlattice. If the superlattice peaks were solely due to lead ions, the contribution to the intensity of each weak peak should be proportional to the square of the lead form factor. Tuning the X-ray energy from 12.885 keV (below the L3 absorption edge of the lead atom) to 13.100 keV (slightly above the edge) reduces the lead form factor[**86**] from $f = 70.21 + 4.187i$ to $f = 62.18 + 10.13i$, and so the absolute intensity of a diffraction peak due to scattering from lead atoms should decrease by $\sim$20%. We have measured the intensities of 13 weak peaks with K_{xy} between 0.6 and 1.4 Å^{-1} at these two energies (data for some representative superlattice peaks and also some organic lattice peaks[4] are shown in Figure 4). Within an experimental error of $\sim$5%, we observed no change for any of these peaks. This

---

[4] Of course,we do not expect the scattering from organic molecules to be affected in any way as the energy passes through the lead absorption edge. Indeed the strong peaks, which are primarily due to scattering from the Langmuir monolayer, did not change. This confirms that our diffraction intensities are reproducible.

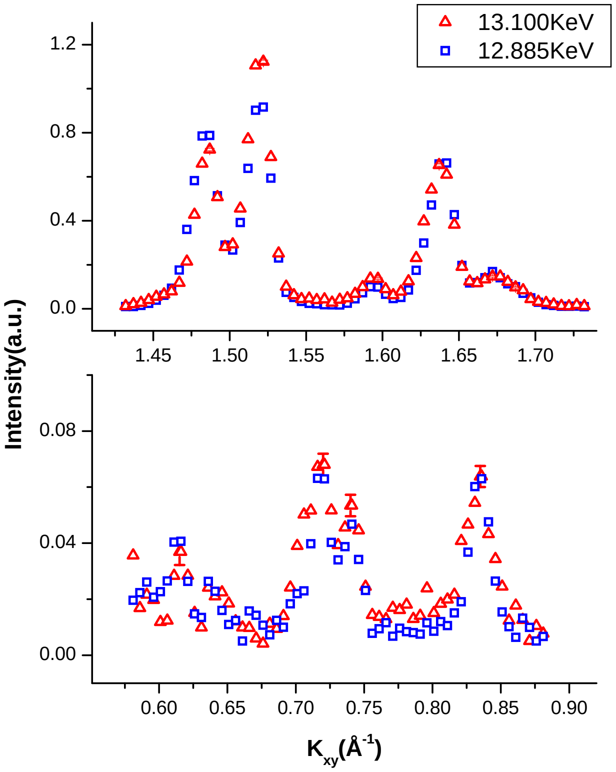

Figure 4.4. In-plane diffraction scan with X-ray energy below and slightly above the L3 absorption edge of lead: (a) three peaks from the organic monolayer plus weak superlattice peaks and (b) four representative superlattice peaks. We also looked at nine other superlattice peaks not shown here, with the same results. If the superlattice consisted of lead atoms only, a 20% change in the peak intensities would be expected. There was no observable change in intensity for any of the peaks studied.

unexpected result means that the simple picture of electrostatic or covalent bonding of individual metal ions to the amphiphile headgroups is inadequate. Since lead does not contribute measurably to the diffraction peak intensity, scattering from the superstructure must be dominated by other atoms. In principle, superlattice reflections can arise from a periodic superstructure within the organic monolayer. For example, small superstructures attributed to protruding ends of the fatty acid molecules because of periodic buckling have been observed in films on solid substrates by AFM [**6**]. Protrusions of the organic molecules have also been observed in polymer lipid monolayers at the air-water interface[**87**], although no superlattice has been reported. However, the Bragg rod widths we observe (Figure 4.2a) are not consistent with horizontal or vertical density modulations in the entire organic monolayer. The only reasonable possibility is that the superlattice peaks are due to a thin layer in the aqueous subphase. Since no superlattice is seen when no multivalent metal ions are added to the subphase (even at very high pH), different lattices are seen when different ions are added, and the results are insensitive to the exact water purity (we have used commercial distilled water on occasion), the lattice cannot be due to impurities in the water. However, it is well established [**88**] that metal ions undergo hydrolysis and hydration in aqueous solution, and a wide range of complex polynuclear oxo(hydroxo)-bridged structures can be formed. The observation of changes in the organic monolayer structure as a function of the subphase pH and subphase ion concentration [**31**] is further evidence that pH- and concentration-sensitive hydrolysis products, rather than isolated ions, are present at the interface. Thus, we expect that hydrolysis products and water molecules arrange themselves under the Langmuir monolayer, interacting with the carboxyl headgroups in such a way as to form a large commensurate superlattice. In this picture, the ratio of lead atoms to other atoms (hydroxyl ions, water) can be small enough that their presence is undetectable in our anomalous scattering studies. We suspect that the same thing happens in the presence of many other ions, such as cadmium[**85**] or silver[**89**], as well. Our results indicate that the process of ion-headgroup complexation may be more complicated than has been previously assumed. Further experiments with spectroscopic techniques that are sensitive to the chemical nature of the inorganic complexes, such as grazing incidence extended X-ray absorption edge fine structure (EXAFS), may be useful to identify the ionic species. Diffraction experiments on Langmuir films with other ions in the subphase are currently under way.

4.2. Superlattices with manganese and magnesium, and effects of other divalent ions

Studies of interactions between simple carboxylic headgroups and aqueous ion complexes may provide new insights into understanding template-directed inorganic nucleation phenomena. There are multiple reports of superlattice reflections in GID patterns of inorganic-organic Langmuir systems, but the interpretation of what they are due to is not entirely clear. The first GID study that directly observed a superstructure of ordered inorganic salt under a Langmuir monolayer was with cadmium ions in the subphase of an arachidic acid monolayer[**85, 55**]. In a similar study with lead under heneicosanoic acid[**57**], anomalous scattering data indicated that the interfacial superlattice is not solely or primarily an array of lead ions but may consist of lead hydrolysis products and water molecules. When calcium ions were dissolved in the subphase, no superlattice was observed[**32**]. To test the conventional interpretation that superlattice peaks are an indication of an ordered inorganic lattice, we have performed a GID study (including Bragg rod scans) on Langmuir films of heneicosanoic acid on a subphase with dilute solutions of Mn^{2+}, Mg^{2+}, Cu^{2+}, Ni^{2+}, Ba^{2+}, and Co^{2+} aqueous ions. This selection represents a wide range of ions with diverse physical properties such as Pauling electronegativity and the ability to hydrate or form hydrolysis products.

4.2.1. Experimental details

Aqueous solutions of chloride salts of manganese (tetrahydrate), magnesium (hexahydrate), nickel, barium, cobalt, and copper (Sigma, quoted purity 99.99% or better for all salts) were prepared at low concentrations (varied from 10^{-6} to 10^{-3} M). The pH was adjusted with sodium hydroxide (Sigma, quoted purity 99.998%) (pH varied from unadjusted up to 10) and measured in the beaker before the solution was poured into the trough. About 65 μL of a 0.87 mg/mL solution of heneicosanoic acid ($C_{20}H_{41}COOH$, or C_{21}, Sigma, quoted purity 99%) in chloroform was spread at the air-water interface. A mechanical barrier compressed the monolayer to a pressure slightly above 0 dynes/cm at 10 °C, and the film was left to equilibrate for an hour. Surface pressure (π) was measured with (0.5 dyn/cm accuracy. A slight overpressure of helium was maintained in the trough to reduce radiation damage and air scattering. To reduce observed effects of radiation damage further, a fresh subphase solution and monolayer were prepared after 2 h of X-ray exposure. In-plane diffraction data are presented after subtracting a linear background. For out-of-plane scans, the background was measured by scanning out-of-plane near but away from the maximum of the corresponding in-plane peak. The measured background was then subtracted from the out-of-plane scan obtained at the maximum of the in-plane peak.

4.2.2. Grazing incidence diffraction

All scans, regardless of the ion present, have two strong peaks in the K_{xy} region between $\sim$1.5 and $\sim$1.8 Å^{-1} (Figures 4.5 and 4.6). Bragg rods at these peaks have a width that corresponds to a monolayer thickness of 27 Å and have a profile similar to Bragg rods seen with heneicosanoic acid in the "S" phase on pure water[**27**]. This confirms that these strong peaks are primarily due to the packing of fatty acid molecules and we will refer to them as "organic peaks". (The structure factor for these reflections may contain a small contribution from the inorganic lattice.) In addition, the intensity maxima along the Bragg rods are at or near $K_z = 0$, which means that the acid molecules are untilted (normal to the plane of the interface). All ions presented in this study induced an untilted structure in the organic film at low pressures (where the molecules are tilted in the absence of ions). The Bragg rods along the additional peaks we have seen in the presence of manganese and magnesium (data to be shown later in this paper) fall off much slower, with an oscillatory modulation. Their width along the rod (drop-off of the overall envelope) is about 6.5 times wider than those along the two strong peaks, which means that these peaks are from a much thinner layer (thickness $\sim$ 4 Å). We will refer to these weak in-plane peaks as "inorganic peaks" or "superlattice peaks". The significance of the oscillations will be considered in section 5.

4.2.2.1. Ions of Type I – nickel, barium, cobalt, and copper. The in-plane scans for nickel, barium, and cobalt ions look similar to the diffraction pattern from a fatty acid in the high pressure S-phase on pure water (Figure **??**), although our observations are at essentially zero pressure. The peak positions are significantly different in the presence of copper, corresponding to the previously reported "X" phase[**32**]. We varied the pH from the equilibrium value to 10 in steps of 0.5 and temperature from 5 to 20 °C in steps of 5 °C, but no superlattice peaks have been observed for the type I ions. Lattice parameters for the organic structures are given in Table 4.3 for all ions.

4.2.2.2. Ions of Type II – manganese and magnesium. A total of 8 distinct peaks have been observed with manganese and 12 peaks with magnesium in the in-plane diffraction scans (Figure 4.6). These patterns are similar to those reported in refs [**57**] and [**55**] for lead and cadmium. For both ions, the organic peaks in the K_{xy} region of $\sim$1.5 Å^{-1} are indexed as (0 1), (1 $\bar{1}$), and (1 0). Relatively strong peaks in the region $K_{xy} > 2.5$ Å^{-1} indexed as (1 $\bar{2}$), (1 1), (2 $\bar{2}$), and (2 0) are higher order peaks from the same organic structure. The remaining peaks can be assigned with fractional indexes. The shortest real-space basis vectors of the organic cell ($\mathbf{a}$, $\mathbf{b}$) and inorganic cell ($\mathbf{a}'$, $\mathbf{b}'$) are related through the vector identities $\mathbf{a}' = \mathbf{a}$ and $\mathbf{b}' = 2\mathbf{b}$ (in the presence of manganese) and $\mathbf{a}' = 2\mathbf{a}$ and $\mathbf{b}' = 2\mathbf{b}$ (in the presence of magnesium). In other words, these are 1×2 and

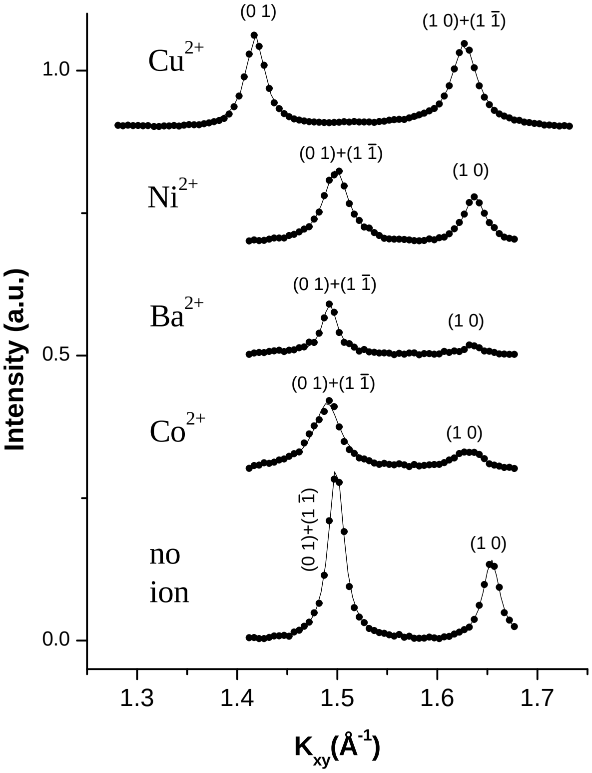

Figure 4.5. Normalized diffracted intensity (arbitrary units) versus K_{xy}, the in-plane component of momentum transfer vector, for heneicosanoic acid Langmuir monolayer at 10 °C with 10^{-4} M $CuCl_2$, $NiCl_2$, $BaCl_2$, $CoCl_2$ in the subphase at ∼0 dyn/cm surface pressure and pH raised to 8.5 with NaOH. These ions did not induce any "extra" superlattice peaks at these or other pH values (in the range 5-10) and concentrations (in the range 10^{-6} to 10^{-3} M in steps of 1 order of magnitude). The scan at the bottom was with the heneicosanoic acid on pure water in the S-phase and is shown for comparison.

Table 4.3. Lattice Parameters of the Organic Film in the Pressence of Various Metal Salts[a]

	Salt	a (Å)	b (Å)	γ (°)	A (Å^2)	ionic radius	electro-negativity
Type I	$CuCl_2$	4.23	4.94	115.3	18.91	73	1.90
	$NiCl_2$	5.00	4.58	123.1	19.20	69	1.91
	$BaCl_2$	5.01	4.58	123.2	19.23	135	0.89
	$CaCl_2$[b]	5.02	4.59	123.1	19.27	100	1.00
	$CoCl_2$	5.04	4.60	123.2	19.41	75	1.88
Type II	$MnCl_2$	4.97	4.48	123.7	18.52	67	1.55
	$MgCl_2$	4.89	4.51	122.8	18.54	72	1.31
	$CdCl_2$[b]	4.89	4.56	121.6	19.00	95	1.69
	$PbCl_2$[b]	4.99	4.52	121.9	19.16	119	2.33

[a] a, b, and γ refer to an oblique unit cell with one molecule. The area per organic molecule is designated by A. The ionic radius is given for an ion with neighbors in a 6-coordinate, octahedral geometry (see ref [**88**]). Electronegativities are from ref [**90**]. [b] We measured these lattice parameters in our recent experiments, but the original studies of fatty acid monolayers with $PbCl_2$, $CdCl_2$, and $CaCl_2$ in the subphase are refs [**57**], [**55**], and [**32**], respectively. Lattice parameters for type I ions are given for the S-phase except for $CuCl_2$ since it induced an X-phase.

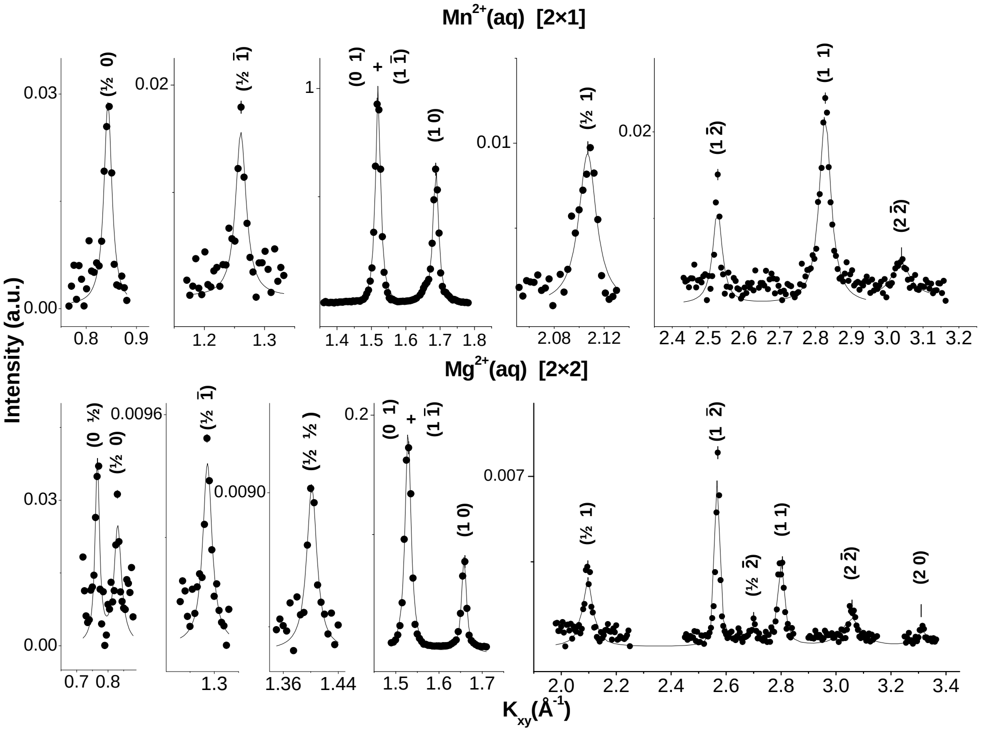

Figure 4.6. Normalized diffracted intensity (arbitrary units) versus K_{xy}, the in-plane component of the momentum transfer vector, for heneicosanoic acid Langmuir monolayer at 10 °C and ∼0 dyn/cm surface pressure, with 10^{-4} M $MnCl_2$ (top) and $MgCl_2$ (bottom) in the subphase and pH raised to 8.5 with NaOH. The lower-integer-order peaks (0 1), (1 0), and $(1\ \bar{1})$ correspond to the reciprocal lattice of the Langmuir monolayer (this identification is made from Bragg rod scans.) The higher integer-order peaks $(1\ \bar{2})$, (1 1), $(2\ \bar{2})$, and (2 0) are also from the Langmuir monolayer. All other peaks are from the 1 × 2 (top) and 2 × 2 (bottom) superlattice.

2×2 superstructures of the organic cell, respectively (Figure 3). The indices and corresponding lattice parameters of the organic and inorganic structures are given in Tables 4.3 and 4.4. Manganese and magnesium are listed as the same type because they induce superstructures in the fatty acid film.

4.2.2.3. Unit cell area. As can be seen from Table 4.3, areas per organic molecule in the presence of ions in the subphase range from 18.52 to 19.41 Å^2, and so the nature of ion-headgroup interactions varies between the two ion types and within each type. Differences in interactions of various aqueous ions with the fatty acids have also been measured by other techniques. Surface potential measurements and light scattering[**91**] showed that alkaline earth metals (Ba, Ca, and Mg) make electrostatic bonds with the headgroups and Pb, Cd, and Co interact by covalent bonding, and in an infrared reflection-absorption spectrometry study[**29**], Cd and Pb were reported to induce a more ordered structure than Ca did. One measure of the nature of a bond is Pauling electronegativity, or the power of an atom to "attract" electrons in a bond. Experiments on LB multilayers [**92**] found that the area per organic molecule decreased with increasing Pauling electronegativity of the ion. In our case, however, areas per molecule are not correlated with electronegativities of corresponding ions (Table 4.3). In LB films, ions may be bound to the headgroups as isolated species, but this is less likely when ions are dissolved

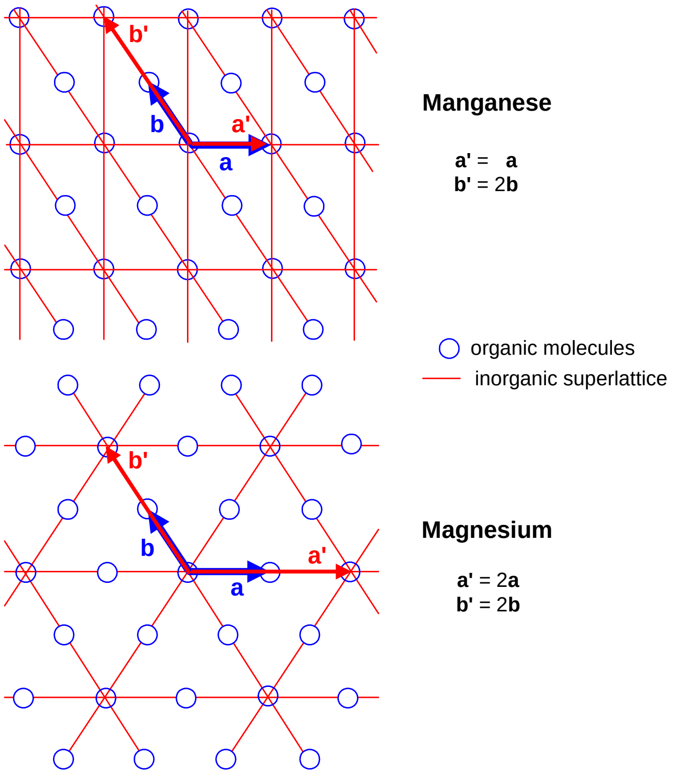

Figure 4.7. Real space lattices of the fatty acid monolayer and superlattices with $MnCl_2$ (top) and $MgCl_2$ (bottom). The heneicosanoic acid molecules are represented by circles.

Table 4.4. In-Plane Positions of Bragg Peaks in the GID Pattern[a]

Manganese				Magnesium							
		K_{xy}(Å^{-1})				K_{xy}(Å^{-1})				K_{xy}(Å^{-1})	
h	*k*	obser.	calc.	*h*	*k*	obser.	calc.	*h*	*k*	obser.	calc.
½	0	0.843	0.843	0	½	0.766	0.764	**1**	**$\bar{2}$**	**2.570**	**2.569**
½	$\bar{1}$	1.261	1.263	½	0	0.830	0.829	½	$\bar{2}$	2.699	2.699
0	**1**	**1.519**	*	½	$\bar{1}$	1.286	1.284	**1**	**1**	**2.799**	**2.799**
1	**$\bar{1}$**	**1.519**	*	½	½	1.402	1.400	**2**	**$\bar{2}$**	**3.058**	**3.057**
1	**0**	**1.687**	*	**0**	**1**	**1.529**	*	**2**	**0**	**3.312**	**3.316**
½	1	2.107	2.108	**1**	**$\bar{1}$**	**1.529**	*				
1	**$\bar{2}$**	**2.526**	**2.527**	**1**	**0**	**1.658**	*				
1	**1**	**2.827**	**2.828**	½	1	2.097	2.097				
2	**$\bar{2}$**	**3.043**	**3.038**	1	½	2.169	2.170				

[a] The "obs" column lists diffraction in-plane peak positions for henecosanoic acid with manganese and magnesium salts in the subphase. Bold type indicates positions of peaks primarily due to the organic film. Studies of multiple films gave peak positions reproducible to ±0.002 Å^{-1}. The calculated positions were determined from the observed magnitudes of three basis vectors (indicated by an asterisk) and using the lattices shown in Figure 3.

in the aqueous subphase. Aqueous metals undergo hydration and can form hydrolysis products in a basic aqueous solution. Reflectivity studies[**55**] on a fatty acid film with cadmium suggest that a hydrolysis product, $CdOH^+$, binds to the headgroup and not just plain Cd^{2+}. Anomalous scattering studies[**57**] on a fatty acid with lead also confirm that lead ions do not bind to the carboxylic headgroups as isolated species. Finally, the sensitivity of the organic monolayer structure to the subphase pH and subphase ion concentration[**93**] also indicates that the aqueous environment plays an essential role in the ion-headgroup interactions. When a Langmiur film with ions is deposited on a solid substrate, it is likely that water is lost during or after the transfer, thus changing the structure. In Langmuir films with ions, we do not find any straightforward correlation of areas per molecule with the physical attributes of corresponding ions. In Table 4.3 the areas increase with the ionic radius only for the type II ions. Type II ions induce superlattices, so they must interact with the headgroups via strong, covalent bonds. This is surprising at first because Pauling electronegativity of isolated Mg^{2+} is low and predicts an ionic bond. However, it is not the bare magnesium that interacts with the headgroup, but its aqua complex, for example, $[Mg(OH_2)]^{2+}$ [**88**], whose interaction with the carboxyl headgroup may be stronger than that of a bare magnesium ion. The remaining ions, Ni^{2+}, Ba^{2+}, Co^{2+}, and Cu^{2+} do not induce superlattices and thus most likely form aqua complexes that make ionic bonds with the headgroups.

Similarly, the electronegativity of isolated Co^{2+} predicts a covalent bond, but the electronegativity of the complex $[Co(OH_2)]^{2+}$ may be different from that of isolated Co^{2+}.

4.2.3. Detailed Bragg rod analysis

4.2.3.1. Bragg rods at organic peaks – finite thickness of the organic film. Fatty acid molecules in their untilted structure can be approximately treated as upright cylindrical rods of length L_{org}, and in this approximation, the intensity profile of a Bragg rod is given by $I_{hk}(K_z) \approx I_0 \sin(N \cdot W)^2 / \sin(W)^2$, where $W = d \cdot K_z/2$ and $L_{org} = d \cdot N$ (see section 2.3), and one expects secondary oscillations in such profiles. Thus, because of the finite thickness of the organic film, Bragg rod profiles at organic peaks will have a primary maximum of width w_{org} and small subsidiary peaks (Figures 4.9c,d and 4.8e,f). The primary and two or three subsidiary maxima are seen in Bragg rods of all organic peaks for films with all ions and also for C_{21} on pure water (Bragg rods are shown only for Mn and Mg). The oscillations are always consistent with a thickness of 27 Å, the length of the heneicosanoic acid molecule.

4.2.3.2. Bragg rods at inorganic (superlattice) peaks – periodic buckling. As in the organic Bragg rods, small secondary maxima (oscillations) are

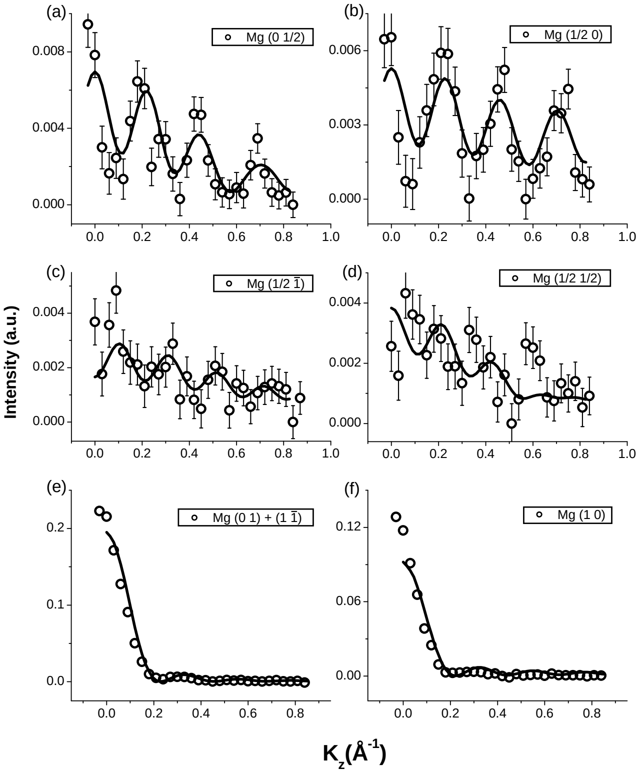

Figure 4.8. Bragg rod scans of six in-plane peaks on a film with $MgCl_2$: (top) Along superlattice "inorganic" peaks (0 1/2), (1/2 0), (1/2 $\bar{1}$), and (1/2 1/2). All four Bragg rods were fitted simultaneously; that is, one set of parameters produced all six curves (Table 4.5). However, a lesser statistical weight was assigned to the rod at (1/2 1/2) since the oscillations of this rod are intrinsically very weak. (bottom) Along peaks due to the organic monolayer (0 1) + (1 $\bar{1}$) and (1 0).

also clearly seen in Bragg rod profiles of the superlattice peaks for manganese and magnesium (Figures 4.9a,b and

4.8a-d), but these profiles lack the strong “primary maximum”. The spacing between oscillations is roughly the same for organic peaks and superlattice peaks, which is quite unexpected: a thin layer of ions would result in a featureless Bragg rod as in Figure 4.10a (right), and the width of such a broad peak, w_{inorg}, would indicate the thickness of the inorganic layer. There is no reason to expect that the ordered subphase layer will be as thick as the inorganic film. On the other hand, if there were no ordered inorganic layers under the Langmuir monolayer and the organic film had an out of-plane density modulation (“buckling”, as shown schematically in Figure 4.10 (left)) with the periodicity of the superlattice, an oscillation in the profile of superlattice Bragg rods would be seen as in Figure 4.10b (right). A superlattice of such “protruding” tail ends would now give rise to superlattice peaks and their corresponding Bragg rod profiles would have oscillations of width w_{pr}. Provided that the protrusions are small, the profiles would have small maxima with no “primary” maximum and the oscillations would have the same spacing as those in the Bragg profiles from the organic layer. All minima would have the same K_z positions in the Bragg rods of different superlattice peaks; the first minimum would occur at $K_z = 0$, and thus, no superlattice peak would be visible at exactly $K_z = 0$. The Bragg rods we observe do not look like either one

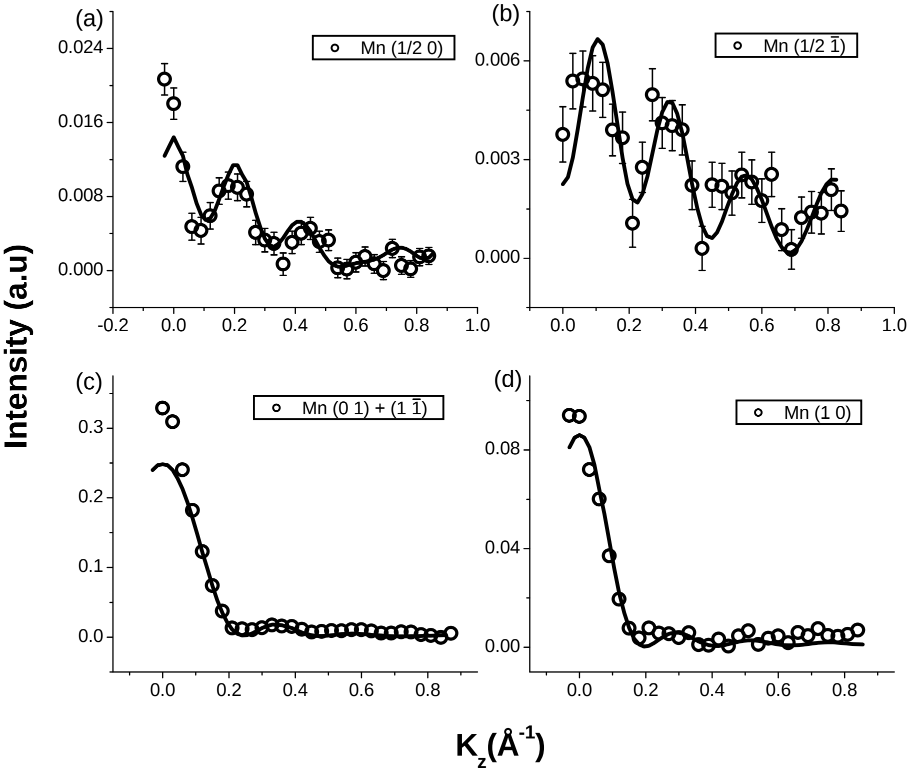

Figure 4.9. Bragg rod scans of four in-plane peaks on a film with $MnCl_2$: (top) Along superlattice "inorganic" peaks (1/2 0) and (1/2 $\bar{1}$) Notice that clear oscillations are present with a width of w_{pr} attributed to protruding chains of the fatty acid. The thin inorganic layer is responsible for the slow intensity falloff. Thus, the overall width w_{inorg} indicates the thickness of the inorganic layer L_{inorg}. (bottom) Along peaks due to the organic monolayer (0 1) + (1 $\bar{1}$) and (1 0). The width w_{org} of these Bragg peaks indicates the thickness of the organic layer L_{org}.

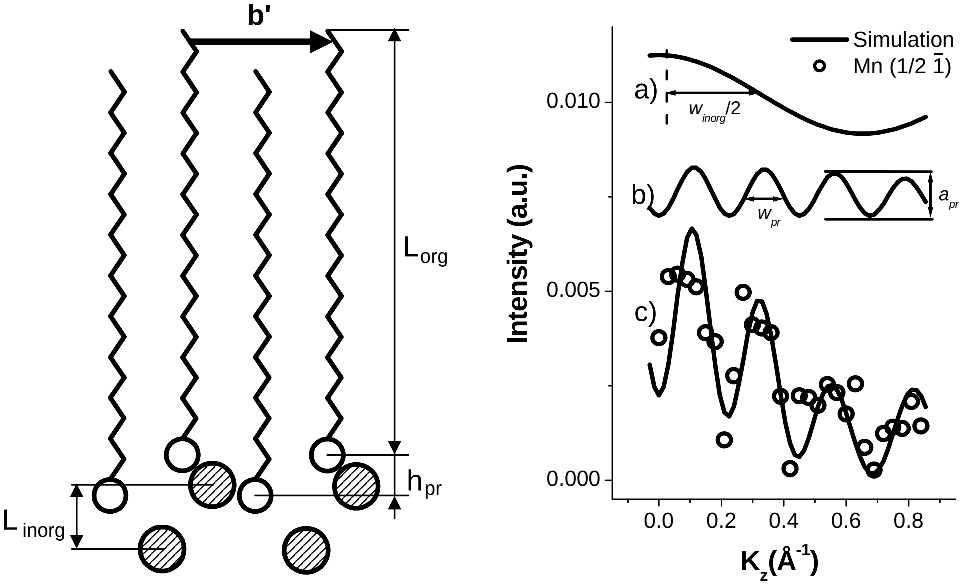

Figure 4.10. (Left) Model of periodic protrusions of aliphatic chains. In a cross-section along the supercell vector **b**, every other molecule is vertically displaced by an amount h_{pr}. Four subphase atoms are placed in a box under the organic film (only two subphase atoms per supercell are shown). Best fits to Bragg rods are obtained with the length of the organic molecule L_{org} ~27 Å, the thickness of the inorganic layer L_{inorg} ~4 Åand the vertical protrusion distance h_{pr} ~2.5 Å. (Right) simulations of Bragg rods: (a) with subphase atoms under an unbuckled organic film (the width, w_{inorg}, indicates the thickness of the inorganic layer, L_{inorg}); (b) with periodic protrusions of organic chains (buckling) and no subphase atoms under the organic film (the oscillation amplitude a_{pr} is affected by the amount of protrusions, h_{pr}, and if the protrusions are small, the width of the oscillations w_{pr} is roughly the same as the width of the primary maximum, w_{org}, of the organic Bragg rod); (c) with both an ordered inorganic layer and periodic protrusions of organic chains.

of the previous cases, but are a combination of both, as in Figure 4.10c (right). We must therefore conclude that the observed superlattice Bragg rods contain a contribution from an ordered inorganic lattice as well as buckling in the organic film. The profiles fall off slowly due to the narrow inorganic layer of size L_{inorg} and have an oscillatory modulation due to a periodic offset of organic chains relative to each other of size h_{pr}. The positions of minima will then depend on the arrangement of atoms within the inorganic layer. To fit the Bragg rods satisfactorily, we have calculated the intensity from the structure factor (see Eq. 2.15) of a model with out-of-plane modulations in the organic film and an ordered inorganic layer under the film. In case of manganese, one organic molecule at position (0, 1/2) in the superlattice unit cell ($\mathbf{a}'$, $\mathbf{b}'$ in Figure 3-top) was offset in the z-direction (normal to water surface) by an amount h_{pr}. In a 1×2 superlattice with two molecules per unit cell, one can equivalently choose to displace either molecule vertically. For magnesium, there are four molecules in the 2×2 superell ($\mathbf{a}'$, $\mathbf{b}'$ in Figure 3, bottom). Since the oscillations are present in every superlattice Bragg rod, the protrusions must also form a 2×2 superlattice, and this leaves only two possibilities: either only one molecule at position (1/2, 1/2) is offset upward or three molecules at positions (0, 0), (0, 1/2), and (1/2, 0) are offset upward. If there were no ions in the subphase, these possibilities would be equivalent since they are related by inversion about a horizontal mirror plane. With the ions, there is no inversion symmetry, and we chose to offset the molecule at (1/2, 1/2) because it gave a better fit to the profiles. Finally, inorganic molecules have to be placed into a 3-D box under the organic molecules defined by the edges of the supercell and by a coordinate z (positive in an upward direction from the water surface) whose origin was chosen at a headgroup of a vertically non-displaced acid molecule. We do not know how many and what molecules are present in the inorganic cell. We, therefore, arbitrarily placed four pseudo-atoms in the box and allowed their positions (x', y', z') to vary within the box to obtain the best Bragg rod fits. The movement of atoms was restricted so that they would preserve a presupposed centrosymmetry of the supercell. All Bragg rod profiles were fitted simultaneously for a particular set of positions and form factors. Fitted positions of the pseudo-atoms are listed in Table 4.5; however, it is important to emphasize that these are representational and may not correspond to positions of any actual atoms.Our model only shows that in order to fit the Bragg rods, there must be an ordered layer of subphase atoms and that the organic film must also buckle. The best fits were achieved with a chain-chain offset $h_{\mathrm{pr}} = 2.5$ Å, which is close to 2 times the C-C spacing in the hydrocarbon chain, and with an inorganic layer of thickness $L_{\mathrm{inorg}} \sim 4$ Å for either ion. Out-of-plane modulations of organic monolayers have also been observed in other studies at the air-water interface. For example, when a large hydrophilic

Table 4.5. Positions of Pseudo-atoms under the Organic Film[a]

	atom	x'/a'	y'/b'	z' (Å)	f'/f_c
Mn^{2+}(aq)	1	0.42	0.61	-3.0	2.6
	2	-0.42	-0.61	-3.0	2.6
	3	0.66	0.49	0.81	3.5
	4	-0.66	-0.49	0.81	3.5
Mg^{2+}(aq)	1	0.68	0.28	-2.4	2.4
	2	-0.68	-0.28	-2.4	2.4
	3	0.61	0.45	0.9	3.6
	4	-0.61	-0.45	0.9	3.6

[a] Four pseudo-atoms with atomic factor f' are placed in a box under the supercell (f_c is the atomic factor for carbon). Two edges of the box are defined by the lattice parameters of the supercell and the third edge along a vector normal to the surface. Positions of atoms are given by fractional coordinates x'/a' and y'/b' and coordinate z' (positive upward, zero at the headgroup of the organic molecule), and x', y', z', and f' are treated as parameters to obtain the best fits to Bragg rods.

polymer was attached to the headgroup of a phospholipid molecule, the lateral packing stresses were relaxed through an increase in out-of-plane protrusions and not by increasing the area occupied per lipid molecule[**87**]. These protrusions did not appear to be ordered. In another study[**94**], a monolayer of arachidic acid with cadmium salt dissolved in the subphase was shown to buckle with a characteristic wavelength $\sim$200 . This is much larger than the periodicity we observe. The large wavelength was attributed to a bending stiffness of the film, and not to individual ion-headgroup interactions. Buckling superstructures have also been observed on a solid substrate of LB films in AFM images[**95, 96**]. In the case of a cadmium salt, for example, the modulation appeared as a gradual, approximately sinusoidal ripple, with an amplitude of 1-2 Å, but the periodicity of the modulation was not commensurate with the organic lattice and the wavelength varied slightly between different domains with an average of 19 Å. Similarly, a buckling ripple was found in the fatty acid film with manganese, but the modulation was incommensurate with the lattice and with a period of 12 Å, and the organic molecules were tilted. Salts of calcium and barium induced 4×2 and 3×1, superstructures respectively in parts of the organic film, and the organic molecules were again tilted. In all these cases, the effects of ions on the organic film on a solid substrate are different from the effects at the air-water interface that we observe. Magnesium ion induced a 2×2 buckling superstructure and an untilted film on a solid substrate, and it is, perhaps coincidentally, the only ion that had the same effect on the organic film on a solid and on a water substrate. It is quite surprising that small ions can pull the headgroups together so strongly that the chains must relieve the in-plane packing stresses through out-of-plane protrusions. What is even more puzzling is that these small ions can interact with the headgroups strongly despite their normal tendency to form weaker, ionic bonds. Therefore it is reasonable to conclude again that ions do not bind to the headgroups as isolated species, but they form large aqueous species as a consequence of hydration and hydrolysis before they bind.

CHAPTER 5

Inorganic nucleation at an organic template

Langmuir monolayers are often used as simple models of biomineralization; they can guide the growth of oriented crystals of specific structure, size, and morphology. Although the assembly of nuclei is assumed to proceed through the process of molecular recognition at the interface, this assumption has so far been only supported by circumstantial evidence. In a multitude of non-structural studies [**45, 97, 46, 47, 48, 40, 49, 51, 43, 52, 53, 54**], it is assumed that the “hard” mineral has the same structure at the interface as it does in the bulk, and that the “soft” monolayer matrix at the surface of a concentrated solution has the same lattice spacings as have been reported for the monolayer on pure water. With these assumptions, an approximate commensurate relationship is identified. Such efforts are entirely reasonable in the absence of in situ evidence. However, in our studies we will show that neither the organic nor the inorganic lattice is rigid; they exert a mutual influence on each other to achieve precise registry at the initial stage of growth.

5.1. Experimental details

We spread Langmuir monolayers of heneicosanoic acid on supersaturated solutions of barium fluoride at just above zero pressure and 25 °C. The BaF_2 solutions were prepared at various concentrations from 3 mM (saturated) to 14 mM by mixing appropriate stoichiometric amounts of barium chloride and ammonium fluoride, a method similar to that in [**43**]. Supersaturated aqueous solutions of strontium fluoride were prepared at concentrations of 4.5mM and 7.5mM by mixing appropriate stoichiometric amounts of strontium chloride and ammonium fluoride, and solutions of calcium carbonate were prepared at concentrations of 7mM and 20mM by mixing stoichiometric amounts of calcium chloride (dihydrate) and sodium bicarbonate (Sigma, quoted purity 99.99% or better for all salts). The pH was adjusted to 8 with sodium hydroxide for all samples. The samples were irradiated by a beam of $\lambda = 1.5491$ Å in the GID geometry.

5.2. Macrostress

5.2.1. Barium fluoride

At low barium ion concentrations, only one organic in-plane peak corresponding to the untilted *LS*-phase is seen. It has been reported in previous studies [**56**] that dilute barium ions at 10 °C induce the high-pressure S-phase in the monolayer; similarly, in our present experiments, performed at 25 °C, they compress the monolayer to the high-pressure LS-phase even at zero pressure. The spacings of the LS-phase are not commensurate with those of BaF_2. As the solution concentration increases, the organic molecules phase-separate to form an entirely new coexisting phase. Three additional peaks appear, one in-plane and two out-of-plane (Figure 5.1a). In this new phase, the molecules are tilted at 29 ° to the surface normal; the new primitive unit-cell has lattice parameters $|\mathbf{a_o}| = 5.249$ Å, $|\mathbf{b_o}| = 5.188$ Å, $\gamma = 124.0\,^\circ$, and area $= 22.59$ Å^2/molecule. These three peaks can be identified as organic because the diffraction peaks have a width in the z-direction (Bragg rod width) consistent with the thickness of the fatty-acid monolayer. Moreover, the positions of these peaks do not change as a function of salt concentrations in the subphase (Figure 5.1b). However, the peak intensities change, indicating that the fraction of the monolayer in the new organic phase is increasing at the expense of the LS phase.

In contrast, the structure of BaF_2 at the interface depends on solution concentration. The inorganic peaks correspond to a cubic phase with lattice spacings not far from that of bulk BaF_2 , but at low concentrations, the peak positions are higher than the bulk positions (Figure 5.2a).

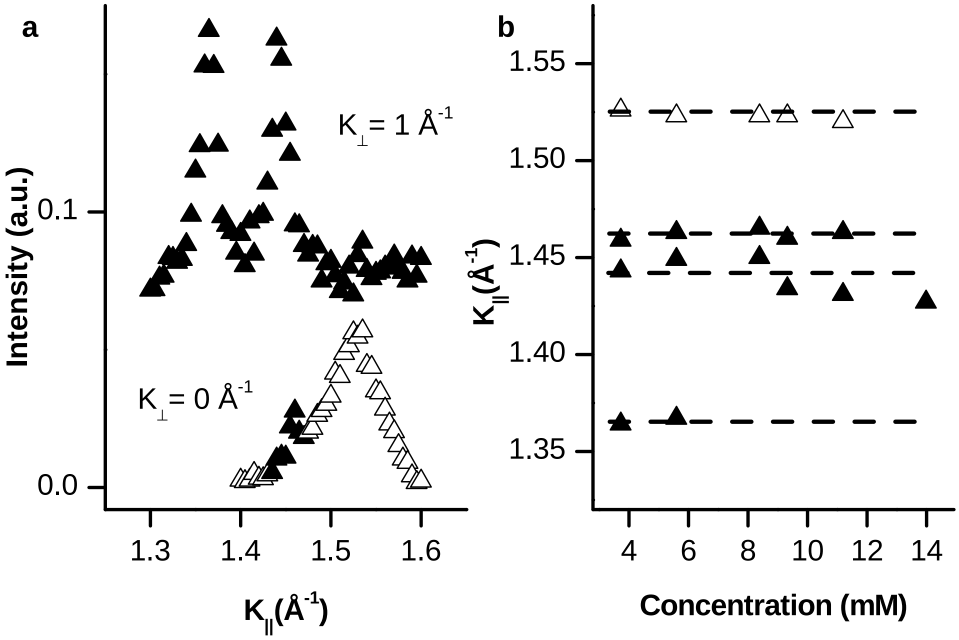

Figure 5.1. Reorganization of heneicosanoic acid monolayers. At low concentrations, only the *LS* peak (△) corresponding to an untilted structure is seen. (a) At the saturated concentration (= 3.7 mM), one in-plane and two out-of-plane organic peaks (▲) can also be seen, indicating a coexisting tilted structure. (b) At higher concentrations, the organic structure remains the same; the organic peak positions do not change with concentration. (The position of the peak at $K_{xy} \sim 1.36$ Å is smeared out by the growing {111} peak of BaF_2 and cannot be accurately determined at higher concentrations.)

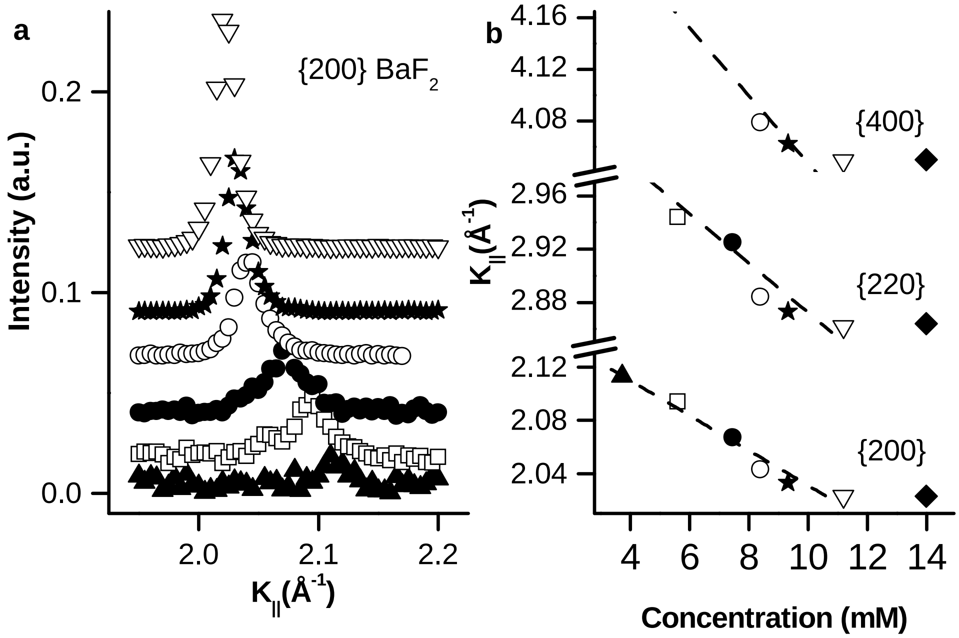

Figure 5.2. Strain relaxation in barium fluoride at the mineral-matrix interface. (a) A representative {200} diffraction peak ‘shifts’ as a function of concentration. The following symbols denote the concentration of the salt in the subphase (in mM): ♦14.0 ▽11.2, ★9.3, ∘8.4, •7.5, □5.6, ▲3.7. (b) Other $\{hk0\}$ peaks ‘shift’ positions as well. The line through the {200} data is a linear fit; the lines through the {220} and {400} data are calculated from the {200} fit. At lower concentrations, some higher-order peaks are too weak to observe.

Since other $\{hk0\}$ peak positions also depend on concentration (Figure 5.2b), the $\langle 100 \rangle$ face of the mineral changes in size, but always remains a square. In other words, the lattice of the mineral is strained, with the horizontal unit-cell spacing contracted from its bulk value of 6.20 Å by as much as 4%. The vertical spacing cannot be determined with sufficient precision [1]. Such strain can occur in thin films [**98**], and indeed, the broad Bragg rods of the $\{hk0\}$ peaks indicate that the inorganic layer is less than 14 Å thick when the solution concentration is 5.6 mM (Figure 5.3a). The lateral size of fatty-acid domains and the BaF_2 crystallites can be estimated from the widths of the respective peaks. The average size of the inorganic domains increases from $\sim$ 100 Å to $\sim$ 250 Å as the concentration increases from 5.6 mM to 14.0 mM. The size of the organic domains is $\sim$ 250Å and does not change.

The strain in the interfacial structure of BaF_2 decreases as the solution concentration increases (Figure 5.2), until the lattice spacing reaches the known bulk value at > 11 mM concentration. (We also see the $\{111\}$, $\{220\}$, $\{311\}$, $\{400\}$ and $\{331\}$ peaks of bulk BaF_2.) At higher concentrations, the diffracted intensity is not distributed along Bragg rods but rather along 'Debye' rings (Figure 5.3b).

---

[1] At low concentrations, the inorganic layer is thin and thus the diffraction peaks are smeared along the z-direction (Figure 5.3a). At higher concentrations the peaks are again smeared along 'Debye rings' (Figure 5.3b). In either case the spacings in the z-direction cannot be measured as precisely as those in the horizontal plane.

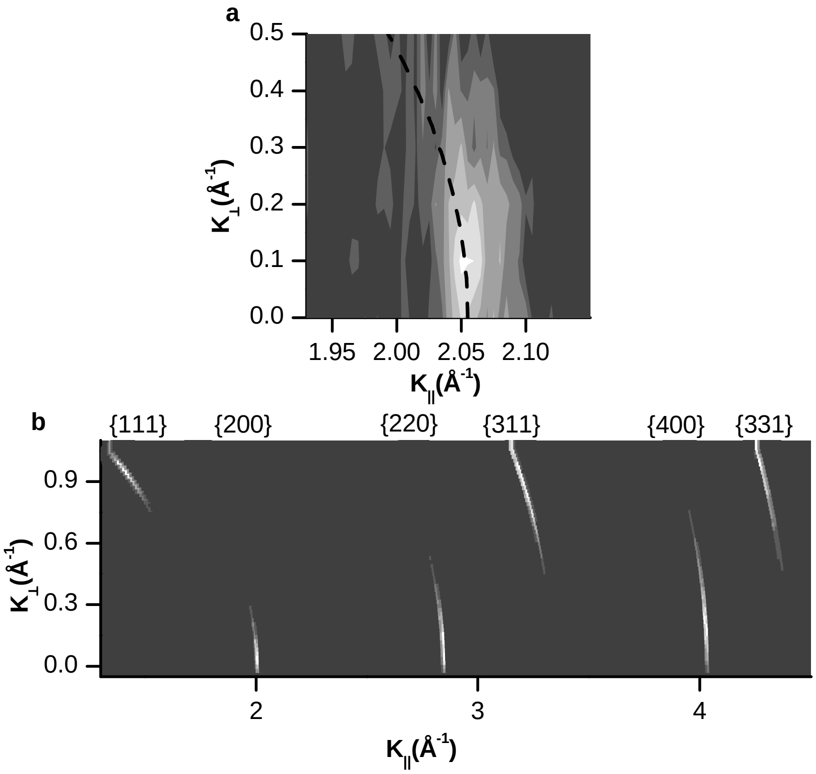

Figure 5.3. The growth of barium fluoride. (a) At a low concentration (5.6 mM), the diffracted intensity of the {200} diffraction spot is 'stretched' in the out-of-plane direction along a Bragg rod. The intensity would follow a 'Debye ring' (dashed line) if the mineral were a powder. (b) At higher concentrations (11.2 mM), the diffracted intensity is peaked along the Debye rings. The positions of the 'hot spots' indicate that the crystallites are preferentially oriented with the $\langle 100 \rangle$ face parallel to the plane of the water surface. This image was not obtained by an image plate or similar device, but was reconstructed from detector scans.

The mineral has grown from a thin layer to slightly misoriented bulk crystallites. Intensity variations along $\{hk0\}$ rings have their maxima at $K_z \sim 0$ Å^{-1} (in the plane of water), and intensities on the $\{hk1\}$ rings reach maximum at $K_z \sim 1$ Å^{-1} ; from that, it follows that the $\langle 100 \rangle$ face of bulk barium fluoride lies parallel to the plane of the matrix. We do not see evidence of other epitaxial orientations or any unoriented crystallites. Based on the intensity variations along the rings, the extent of misorientation is only $2.5\,^{\circ}$ at 11.2 mM. It should be noted that either without any monolayer (no template) or under a monolayer of heneicosanol (neutral headgroups), barium fluoride and barium chloride fluoride nucleate at the interface as non-oriented crystallites.

The effects observed as a function of concentration are also observed by varying the temperature. Crystallites should grow with decreasing temperature because the solubility of barium fluoride decreases, and the crystallites should shrink with increasing temperature because they partially re-dissolve. When the sample is cooled from 25 °C to 10 °C at a slightly oversaturated concentration, the BaF_2 spacings expand by 0.9%. The process is reversible; when the sample is heated back to 25 °C, the spacings contract by almost the same percentage. These results are consistent with the expected inverse relationship between strain and film thickness. To ascertain that the 'peak shifting' is not an artifact of a chemical reaction, for example, of incorporating either chlorine or ammonium ions into the interfacial structure (Vegard's law), we have also prepared the supersaturated solution of BaF_2 by mixing stoichiometric amounts of hydrofluoric acid with barium hydroxide. This method of sample preparation, used only on occasion because of safety concerns when working with hydrofluoric acid, reproduced the trends reported here exactly.

Although scattering from the BaF_2 structure is too weak to observe at concentrations below 4 mM, we can extrapolate to zero concentrations to determine the structure at the earliest stage. A linear fit to the trend of the lattice contraction in Figure 5.2b intercepts the K_{xy}-axis at 2.16 Å^{-1}. The corresponding real-space parameters of the face-centered-square unit-cell (the face of the cubic BaF_2) are $|\mathbf{a_i}| = |\mathbf{b_i}| = 5.82$ Å and the area of the face is 33.85 Å^2. The area of the organic unit-cell (from data in Figure 5.1a) is 22.59 Å^2. The ratio of these numbers is 1.50, which strongly suggests that these structures are epitaxial. Indeed, the lattices are commensurate; i.e., they share a common supercell. The supercell basis vectors $(\mathbf{a_s}, \mathbf{b_s})$ can be defined in terms of either the organic $(\mathbf{a_o}, \mathbf{b_o})$ or inorganic $(\mathbf{a_i}, \mathbf{b_i})$ basis vectors:

$$\mathbf{a_s} = 4\mathbf{a_o} = 3\mathbf{a_i} + 2\mathbf{b_i}$$

$$\mathbf{b_s} = -2\mathbf{a_o} - 3\mathbf{b_o} = \mathbf{a_i} - 2\mathbf{b_i}$$

These relationships are accurate to better than 0.1%. The real-space lattices are shown in Figure 5.4.

5.2.2. Strontium fluoride

The structure of SrF_2 at the interface depends on time and solution concentration. A weak {200} peak of strontium fluoride appeared from a barely supersaturated solution (4.5mM) about 3 hours after the sample preparation but at a higher K-vector position than expected from an ideal crystal. Successive scans of this peak show that it is “shifting” toward the bulk position with time as shown in Figure 5.5a and 5.5b. The peak reached a stable position (but not quite that of the bulk) about 6 hours after the sample preparation. The in-plane peaks {220} and {400} have also “shifted” to higher than bulk positions. In other words, the mineral nucleates with a strained cubic lattice at the initial stage, with the horizontal unit-cell spacing contracted from its bulk value of 5.8 Å by 1.6%, and the strained structure relaxes toward the bulk unit-cell with time. This is the same effect of lattice contraction induced by the organic monolayer as we have recently reported for barium fluoride (5.1). At the same supersaturation, the average rate of SrF_2 peak-shifts (-2×10^{-4} Å^{-1}/min) is faster than that of previously observed BaF_2 peak-shifts (-5×10^{-5} Å^{-1}/min). The faster relaxation of the strontium fluoride structure at the interface is consistent with the known fact that, on average, the

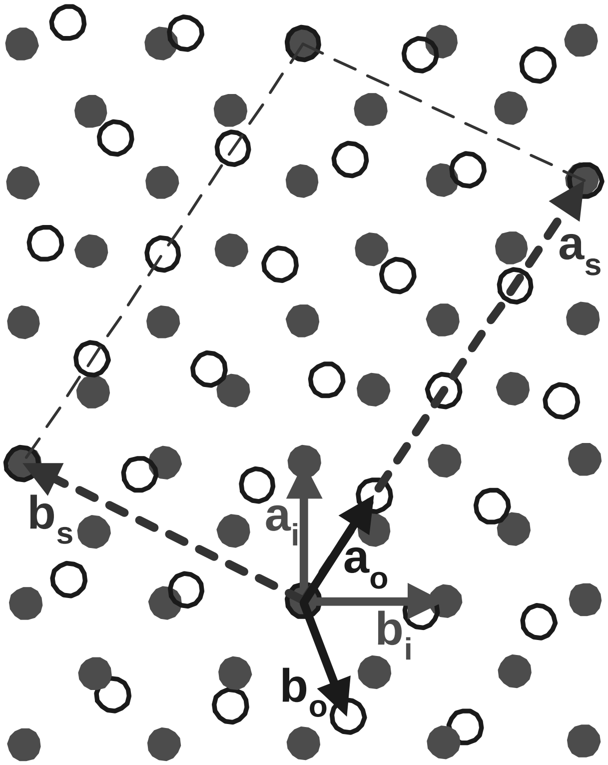

Figure 5.4. Real space lattices of the fatty-acid headgroups (○) and barium atoms (●) of the ⟨100⟩ face of barium fluoride. The lattices are commensurate because they share a common super-cell (outlined by the dashed line). See text for the definition of relationships among the super-cell ($\mathbf{a_s}, \mathbf{b_s}$), organic ($\mathbf{a_o}, \mathbf{b_o}$), and inorganic ($\mathbf{a_i}, \mathbf{b_i}$) basis vectors. The relative translation of the two lattices is arbitrary.

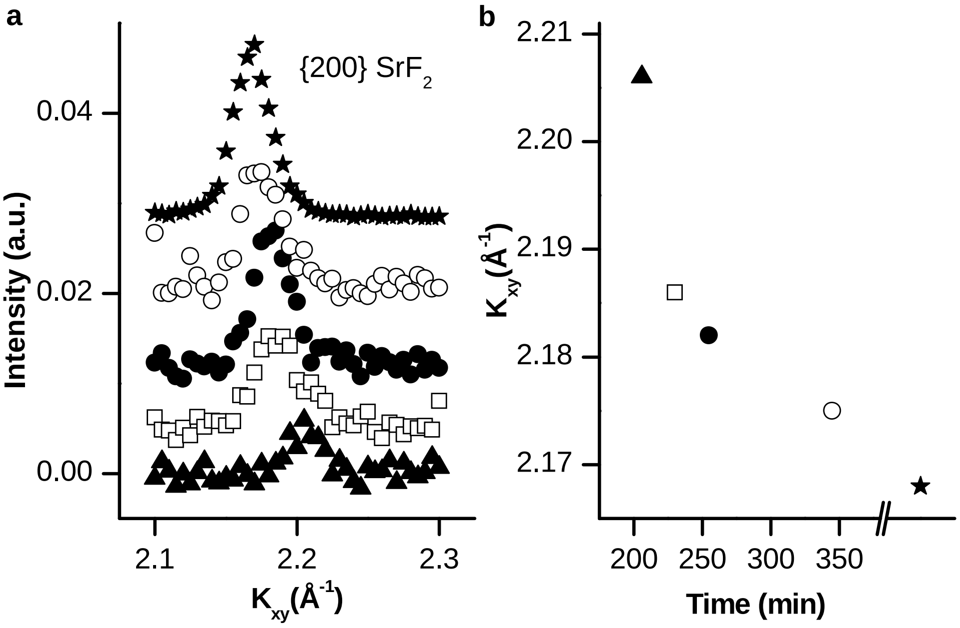

Figure 5.5. Macrostrain relaxation in strontium fluoride at the mineral-matrix interface. (a) A representative {200} diffraction peak "shifts" as a function of time at concentration of 4.5mM. The following symbols denote time after spreading the organic film (in minutes): ▲ 206, □ 230, • 255, ○ 345. The peak from a slightly more concentrated solution (7.5mM) denoted by "★" appears at the ideal, bulk position. (b) The mineral begins to grow strained by as much as 1.6% from its bulk structure.

nucleation rate of a bulk strontium fluoride [**99**] is faster than that of a bulk barium fluoride [**100**]. The relatively fast nucleation of strontium fluoride, unfortunately, does not allow us to see the reorganization of molecules in the organic layer, as we have seen in the Langmuir monolayer with barium fluoride, although we do see the LS-phase at undersaturated concentrations (not shown) as we have seen with other divalent ions [**56**] in dilute solutions. Because of the narrow metastable region of strontium fluoride, diffraction peaks (designated by a '★' in Figure 5.5) from a little more concentrated solution appear at their usual bulk position immediately after spreading the organic film. The contour plots in Fig. 5.6a and 5.6b at low supersaturation show that the {200} and {220} Bragg spots are smeared partly along a "vertical" line (Bragg rod), and partly along "Debye" rings. These two directions of smearing indicate that the bulk inorganic crystals grow from a thin inorganic layer to slightly misoriented crystallites. The width of the Bragg rods indicates that the inorganic layer is less than 20 Å thick when the solution concentration is 4.5 mM. At high supersaturation (7.5mM), the diffracted intensity is not distributed along Bragg rods but entirely along the "Debye" rings (Figure 5.7). Intensity variations along {hk0} rings have their maxima at $K_z \sim 0$ Å^{-1} (in the plane of water), and although our apparatus does not allow us to scan far enough to observe the maxima of the $\{hk1\}$ rings, it is apparent that the $\langle 100\rangle$ face of bulk strontium fluoride lies parallel to the plane of the organic matrix. We

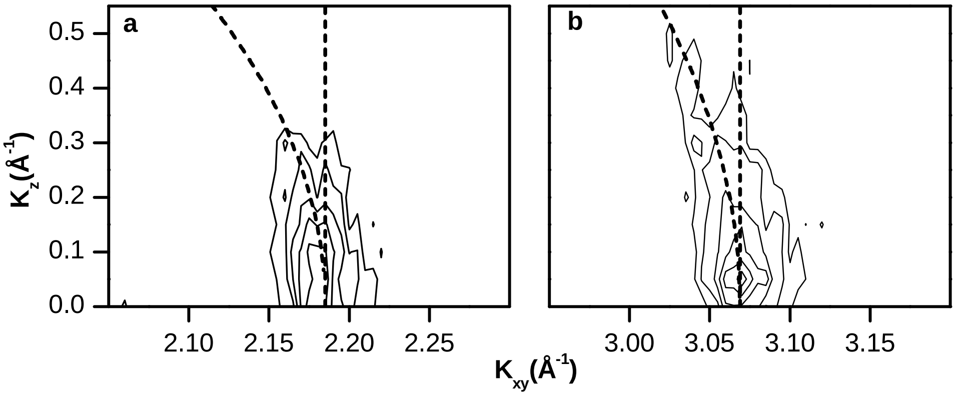

Figure 5.6. The growth of strontium fluoride. (a) At low supersaturation the diffracted intensity of the {200} diffraction spot is partially smeared out in the out-of-plane direction along a Bragg rod and partially along a “Debye” ring. The dashed lines along the two directions of smearing are guides to the eye. (b) As expected, similar smearing shows in the {220} peak.

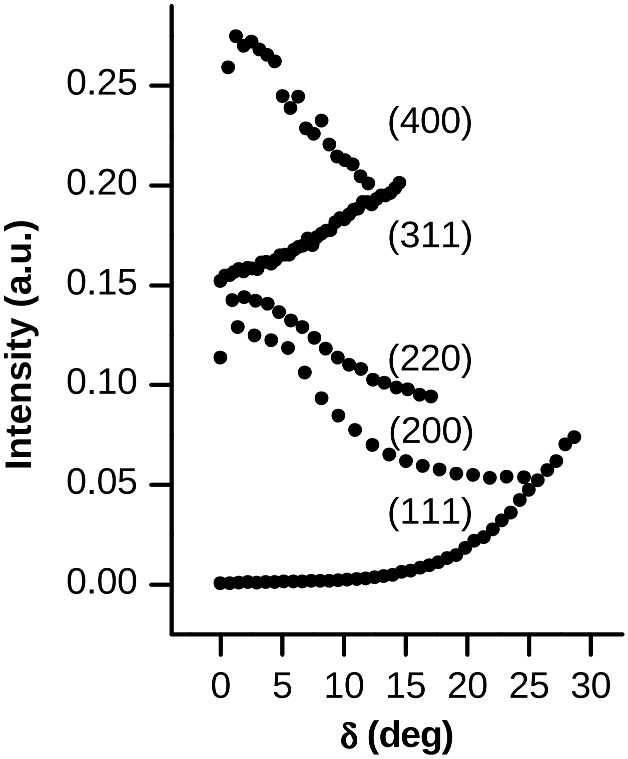

Figure 5.7. At high supersaturation, the diffracted intensity is entirely peaked along the Debye rings. The maxima of the intensity distribution indicate that the crystallites are preferentially oriented with the $\langle 100 \rangle$ face parallel to the plane of the water surface. The angle δ is defined as $\tan \delta = |K_z|/|K_{xy}|$; the total wave vector $K = \sqrt{K_{xy}^2 + K_z^2}$ is the "radius" of the Debye ring. Intensity values for data points of the $\{111\}$ curve have been divided by 50 and for the $\{200\}$ and $\{311\}$ curve by 5 so that they can be shown on the same scale.

do not see evidence of other epitaxial orientations or any unoriented crystallites. Based on the intensity variations along the rings, the extent of misorientation is only ±5 °C FWHM at 7.5 mM.

Motivated by numerous, non-structural studies of the oriented nucleation of the biologically important calcium carbonate, we have also looked for the face-selective nucleation of this salt, but have not found it. Consistent with the macroscopic studies, we also find that calcium carbonate nucleates at the air-water interface either in the form of vaterite or calcite, depending on calcium concentration in the subphase [**43**]. However, neither of the two polymorphs have a preferred crystallographic orientation; they both nucleate as powders, as shown in the representative in-plane diffraction scan of calcite in Figure 5.8. As expected from a powder, all allowed calcite peaks are visible, regardless of their crystallographic indices. Also as expected from unoriented crystallites, the intensity along Debye rings (not shown) fluctuates randomly. It is possible that a small number of calcium crystals is oriented but the crystals are too large to be easily detected by the x-rays; i.e., they are not sufficiently "powder averaged" in the plane of the monolayer. Other than that, we cannot explain the discrepancy between our in-situ and the other ex-situ studies at this time. The arrow in Fig. 5.8 points to a peak from the *LS*-phase of the organic monolayer that is also seen with other ions at undersaturated concentration. Although the organic *LS*-peak has disappeared at supersaturated

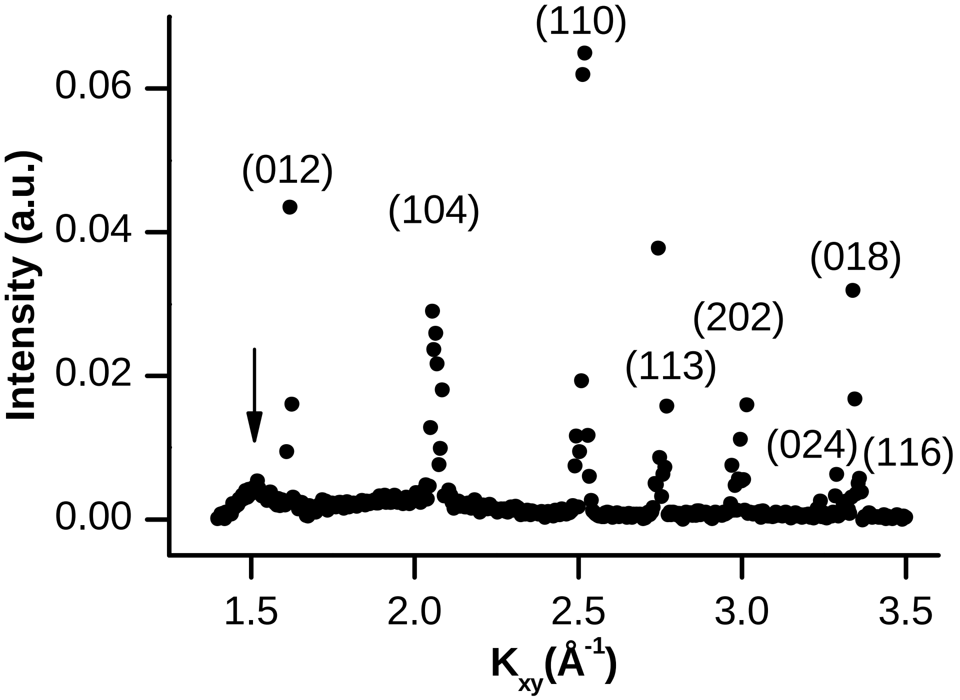

Figure 5.8. An in-plane diffraction scan of interfacial calcium carbonate. All allowed peaks are visible, regardless of their indices, indicating that there is no preferred crystallographic orientation of calcite.

concentrations of fluorides, it seems unaffected by supersaturated calcium carbonate.

5.3. Microstress

5.3.1. Barium fluoride

The main effect of growing barium and strontium fluoride at an organic template is the lattice parameter distortion, which results in shifts of the diffraction line positions. Together with peak shifts, line broadening is also observed with barium fluoride with decreasing concentration. We will analyze the broadening effects with barium fluoride, but not with strontium fluoride because the diffraction peaks strontium fluoride are weak and shift with time (as opposed to concentration), so their width cannot be ascertained with sufficient precision. As can be seen in Figure 5.9, the integral breadth of diffraction lines depends on the Bragg angle; from that, it follows that both size and strain effects must be contributing to the broadening of the peaks. We fit the trend using the equation for the overall broadening (see theoretical background) and extract the in-plane length L, and the maximum strain e as parameters of the fit. The domain size is about 200 Å at low concentrations, and as the crystallites grow at higher concentrations, the length of the domain size increases up to about 500 Å as shown in Figure 5.10b. Peaks at all concentrations are broader than the resolution limit of about 1000 Å. The non-

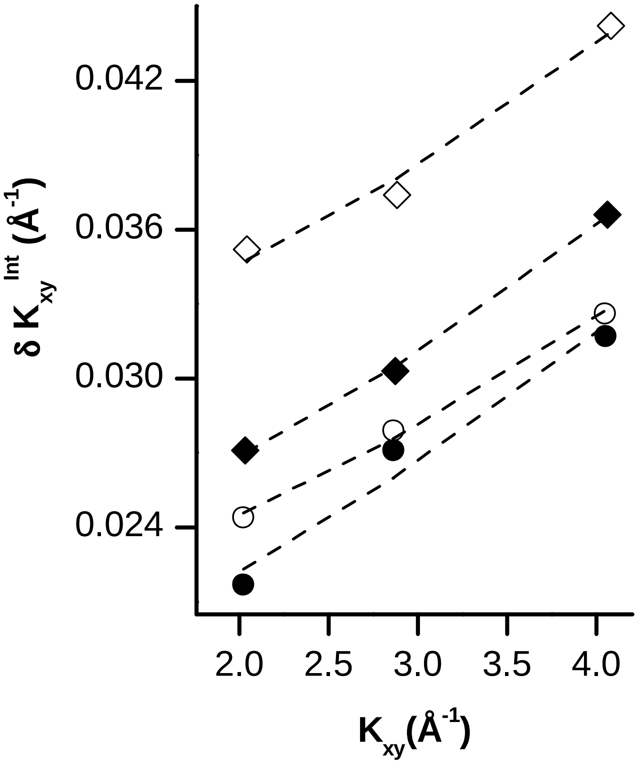

Figure 5.9. Integral breadths of the diffraction peaks from interfacial barium fluoride. The following symbols denote the salt concentration (in mM): • 14.0, ○ 11.2, ◊ 9.3, ⧫ 8.4. If the peak broadening were solely due to domain size, values of breaths would be independent of the scattering vector. Instead, the breadth depends on the momentum transfer vector, and also increases as the concentration decreases. The effect of this broadening is thus most likely caused by an increased number of structural defects when the salt begins to grow.

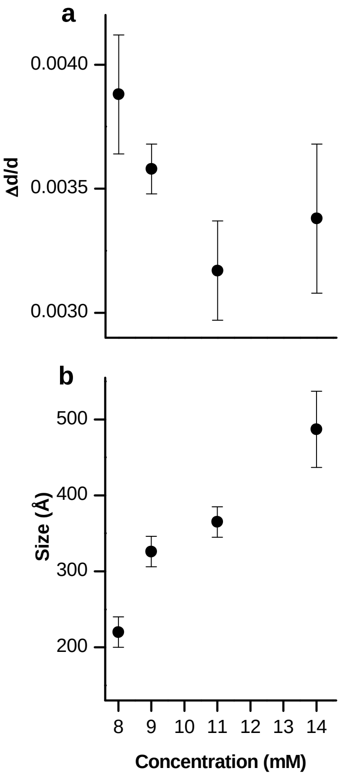

Figure 5.10. Microstrain relaxation in barium fluoride at the mineral-matrix interface. The microstrain in (a) and the domain size in (b) have been determined from fits to the broadening effects in Figure 5.9

uniform strain (microstrain) decreases as the domain size increases and as the peak positions approach their ideal, bulk values. At the lowest concentration, when the domain size is small, the maximum non-uniform lattice distortion is about 0.004 and drops off only slightly with increasing concentration as shown in Figure 5.10a. This trend is consistent with the expectation that the structure takes on its usual, non-strained form as the crystallites grow. Our observations reveal global strain effects (peak shifts) correlated with increasing microstrain (peak broadening) at the organic-inorganic interface. The peaks shifts indicate a uniform deviation of atoms from their ideal positions (lattice contraction), and the peak broadening indicates that the position of atoms fluctuates about their new, contracted lattice points. Strain in solid materials can be caused by many different crystal defects, but given the nature of our sample, it is most likely that both macro and micro strain effects at the organic-inorganic interface are caused by point defects probably by entrapment of water or hydroxyl ions by the crystal at the initial stage of growth.

CHAPTER 6

Conclusions

One of the goals of research in materials engineering is to attain the capability of assembling individual molecules into highly ordered architectures. Langmuir monolayers are uniquely suited to achieve such goal in a practical way; structures of these thin films can be manipulated into highly ordered architectures by mere addition of ions into the subphase. It has been known that divalent ions tend to 'stabilize' the monolayer, whereas monovalent ions tend to have little effect, and our studies show why: adding monovalent ions into the subphase (by raising the pH) disorders the monolayer in a similar way that increasing temperature would, but adding divalent ions compresses the monolayer into high-pressure, well-ordered phases in a similar way that squeezing the barrier would.

We have seen that divalent ions dissolved in the aqueous subphase induce a variety of structures in the Langmuir film and can be divided into two types. The first type appear to merely compress the film, while ions of the second type, in addition to compressing the monolayer, generate superlattice structures. Ions of type II are presumed to interact with the headgroups strongly (covalently), but not as isolated species; rather, our anomalous scattering studies indicate they act in the form of large hydrated complexes or hydrolysis products. Aqua ion-headgroup interactions are so strong in the case of Mn and Mg that the organic film buckles with a periodic out-of-plane modulation commensurate with the lattice.

In addition to studies of monolayers on dilute salt solutions, we have also prepared the films on supersaturated solutions, in which the salts begin to nucleate at the organic template (a model biomineralization process). Our results confirmed a long suspected assumption: there can exist an epitaxy at an organic-inorganic interface. We found that both the organic matrix and the nucleating structure undergo rearrangements to allow the atomic planes of the 'hard' mineral to continue those of the 'soft' organic substrate. Not only can an exact relationship exist between parameters of the organic and inorganic lattices, but also the coincidence of parameters allows selective nucleation – of the several possible species (barium fluoride, barium chloride fluoride, barium hydroxide) and crystallographic orientations, the fatty-acid monolayer exclusively selects out crystals of barium fluoride with well-oriented $\langle 100 \rangle$ crystallographic faces for nucleation. An exact coincidence between the structures of different materials is normally rare, but it can occur if the interfacial lattices deform. Strained epitaxial growth is well known in thin film studies under ultrahigh vacuum, but we have now seen that it can happen in template-directed growth from solution as well.

The beauty of molecular organization in Langmuir monolayers, when ions are added to the aqueous subphase, is that it is a spontaneous process. Molecules organize into various architectures on their own, without any “outside” force. Such “self-assembly” of organic molecules can direct nucleation of inorganic material via structural matching, and explains how nature can incorporate minerals into the organic world of living organisms. Materials engineers can exploit self-assembly to construct films of various molecular architectures by using salts or other inorganic compounds. The future research on molecular organization and the ensuing structures will help direct the design of amphiphiles and allow preparation of thin films with useful properties.

References

[1] Lin, B. PhD thesis, Northwestern University, **1990**.

[2] Shih, M.; Bohanon, T.; Mikrut, J.; Zschack, P.; Dutta, P. *Phys. Rev. A* **1992**, *45*, 5734.

[3] Böhm, C.; Leveiller, F.; Jacquemain, D.; Möhwald, H.; Kjaer, K.; Als-Nielsen, J.; Weissbuch, I.; Leiserowitz, L. *Langmuir* **1994**, *10*, 830.

[4] Schwartz, D. *Surf. Sci. Rep.* **1997**, *27*, 241.

[5] Ghaskadvi, R.; Carr, S.; Denim, M. *J. Chem. Phys.* **1999**, *111*, 3675.

[6] Zasadinski, J.; Viswanathan, R.; Madsen, L.; Garnaes, J.; Schwartz, D. *Science* **1994**, *263*, 1726.

[7] Bloch, J.; Yun, W. *Phys. Rev. A* **1990**, *41*, 844.

[8] Mann, S.; Archibald, D. D.; Didymus, J. M.; Douglas, T.; Heywood, B. R.; Meldrum, F. C.; Reeves, N. J. *Science* **1993**, *261*, 1286–1292.

[9] Ställberg-Stenhagen, S.; Stenhagen, E. *Nature* **1945**, *156*, 239.

[10] Lundquist, M. *Chem. Scr.* **1971**, *1*, 197.

[11] Overback, G.; Möbius, D. *J. Phys. Chem.* **1993**, *97*, 7999.

[12] Schwartz, D.; Knobler, C. *J. Phys. Chem.* **1993**, *97*, 8849.

[13] Hönig, D.; Möbius, D. *J. Phys. Chem.* **1991**, *95*, 4590.

[14] Xue, J.; Jung, C.; Kim, M. *Phys. Rev. Lett.* **1992**, *69*, 474.

[15] Rasi, T.; Shen, Y.; Kim, M.; Jr., P. V.; Bloch, J. *J. Phys. Rev. A* **1985**, *31*, 537.

[16] Rasi, T.; Shen, Y.; Kim, M.; Grubb, S. *Phys. Phys. Lett.* **1985**, *55*, 2903.

[17] Guyot-Sionnest, P.; Hunt, J.; Shen, Y. *Phys. Rev. Lett.* **1987**, *59*, 1597.

[18] Sauer, B.; Chen, Y.; Zografi, G.; Yu, H. *Langmuir* **1988**, *4*, 111.

[19] Dutta, P.; Peng, J.; Lin, B.; Ketterson, J.; Prakash, M.; Georgopoulos, P.; Ehrlich, S. *Phys. Rev. Lett.* **1987**, *58*, 2228.

[20] Kjaer, K.; Als-Nielsen, J.; Helm, C.; Laxhuber, L.; Möhwald, H. *Phys. Rev. Lett.* **1987**, *58*, 2224.

[21] Kjaer, K.; Als-Nielsen, J.; Helm, C.; Tippman-Krayer, P.; Möhwald, H. *J. Phys. Chem.* **1989**, *93*, 3200.

[22] Lin, B.; Shih, M.; Bohanon, T.; Ice, G.; Dutta, P. *Phys. Rev. Lett.* **1990**, *65*, 191.

[23] Bohanon, T.; Lin, B.; Shih, M.; Ice, G.; Dutta, P. *J. Chem. Phys.* **1990**, *41*, 4846.

[24] Kenn, R.; Böhm, C.; Bibo, A.; Peterson, I.; Möhwald, H.; Als-Nielsen, J.; Kjaer, K. *Phys. Chem.* **1991**, *95*, 2092.

[25] Schlossman, M.; Schwartz, D.; Pershan, P.; Kawamoto, E.; Kellogg, C.; Lee, S. *Phys. Rev. Lett.* **1991**, *66*, 1599.

[26] Shih, M.; Durbin, M.; Malik, A.; Zschack, P.; Dutta, P. *J. Chem. Phys.* **1994**, *101*, 9132.

[27] Kaganer, V.; Möhwald, H.; Dutta, P. *Rev. Mod. Phys.* **1999**, *71*, 779.

[28] Yazdanian, M.; Yu, H.; Zografi, G. *Langmuir* **1990**, *6*, 1093.

[29] Gericke, A.; Hühnerfuss, H. *Thin Solid Films* **1994**, *245*, 74.

[30] Ulman, A. *An Introduction to Ultrathin Organic Films from Langmuir-Blodgett to Self-Assembly;* Academic Press: New York, 1991.

[31] Datta, A.; Kmetko, J.; Richter, A.; Yu, C.-J.; Dutta, P. *Langmuir* **2000**, *16*, 1239.

[32] Shih, M.; Bohanon, T.; Mikrut, J.; Zschack, P.; Dutta, P. *J. Chem. Phys.* **1992**, *96*, 1556.

[33] Addadi, L.; Beniash, E.; Weiner, S. In *Supramolecular organization and materials design*; Jones, W., Rao, C., Eds.; Cambridge UP: Cambridge, UK, 2002; page 1.

[34] Mann, S. In *Inorganic materials*; Bruce, D. W., O'Hare, D., Eds.; Wiley: Chichester, England, 1992; page 238.

[35] Mann, S. *Nature* **1993**, *365*, 492–505.

[36] Mann, S. *Biomineralization: Principles and Concepts in Bioinorganic Materials Chemistry;* Oxford UP, 2001.

[37] Rapaport, H.; Kuzmenko, I.; Berfeld, M.; Kjaer, K.; Als-Nielsen, J.; Popovitz-Biro, R.; Weisbuch, I.; Lahav, M.; Leiserowitz, L. *J. Phys. Chem. B.* **2000**, *104*, 1399–1428.

[38] Weissbuch, I.; Popovitz-Biro, R.; Lahav, M.; Leiserowitz, L. *Acta Cryst.* **1995**, *B51*, 115–148.

[39] Lahav, M.; Leiserowitz, L. *J. Phys. D: Appl. Phys.* **1993**, *26*, B22–B31.

[40] Heywood, B. R.; Mann, S. *Chem. Mater.* **1994**, *6*, 311–318.

[41] Litvin, A.; Valiyaveettil, S.; Kaplan, D.; Mann, S. *Adv. Mater.* **1997**, *9*, 124.

[42] Mann, S.; Heywood, B.; Rajam, S.; Walker, J. *J. Phys. D: Appl. Phys.* **1991**, *24*, 154.

[43] Walker, J. B.; Heywood, B. R.; Mann, S. *J. Mater. Chem.* **1991**, *1*, 889.

[44] Xu, G.; Yao, N.; Aksay, I.; Groves, J. *J. Am. Chem. Soc.* **1998**, *120*, 11977.

[45] Backov, R.; Lee, C. M.; Khan, S. R.; Mingotaud, C.; Fanucci, G. E.; Talham, D. R. *Langmuir* **2000**, *16*, 6013–6019.

[46] Heywood, B. R.; Mann, S. *Adv. Mater.* **1992**, *4*, 278–282.

[47] Heywood, B. R.; Mann, S. *Langmuir* **1992**, *8*, 1492–1498.

[48] Heywood, B. R.; Mann, S. *J. Am. Chem. Soc.* **1992**, *114*, 4681–4686.

[49] Li, B.; Liu, Y.; Lu, N.; Yu, J.; Bai, Y.; Pang, W.; Xu, R. *Langmuir* **1999**, *15*, 4837–4831.

[50] Lu, L.; Cui, H.; Li, W.; Zhang, H.; Xi, S. *Chem. Mater.* **2001**, *13*, 325.

[51] Lu, L.; Cui, H.; Li, W.; Zhang, H.; Xi, S. *J. Mater. Res.* **2001**, *16*, 2415–2420.

[52] Yang, J.; Meldrum, F. C.; Fendler, J. H. *J. Phys. Chem.* **1995**, *99*, 5500–5504.

[53] Yang, J.; Fendler, J. H. *J. Phys. Chem.* **1995**, *99*, 5505.

[54] Zhao, X.; Yang, J.; McCormick, L.; Fendler, J. *J. Phys. Chem.* **1992**, *96*, 9933–9939.

[55] Leveiller, F.; Bohm, C.; Jacquemain, D.; Mohwald, H.; Leserowitz, L.; Kjaer, K.; Als-Nielsen, J. *Langmuir* **1994**, *10*, 819–829.

[56] Kmetko, J.; Datta, A.; Evmenenko, G.; Dutta, P. *J. Phys. Chem. B* **2001**, *105*, 10818.

[57] Kmetko, J.; Datta, A.; Evmenenko, G.; Durbin, M. K.; Richter, A. G.; Dutta, P. *Langmuir* **2001**, *17*, 4697.

[58] Weissbuch, I.; Berfeld, M.; Bouwman, W.; Kjaer, K.; Als-Nielsen, J.; Lahav, M.; Leiserowitz, L. *J. Am. Chem. Soc.* **1997**, *119*, 933–942.

[59] Majewski, J.; Popovitz-Biro, R.; Kjaer, K.; Als-Nielsen, J.; Lahav, M.; Leiserowitz, L. *J. Phys. Chem.* **1994**, *98*, 4087–4093.

[60] Kaganer, V.; Peterson, I.; Kenn, R.; Shih, M.; Durbin, M.; Dutta, P. *J. Chem. Phys.* **1995**, *102*, 9412.

[61] Robinson, I. *Handbook on Synchrotron Radiation*, Vol. 3; North-Holland: New York, 1991.

[62] Woolfson, M.; Cambridge UP: New York, 1996; chapter 9; 2 ed.

[63] Kimmel, G.; Dayan, D.; Oxfod UP, 1999; chapter 29, page 698.

[64] Langford, J.; Oxfod UP, 1999; chapter 5, page 59.

[65] Klug, H. P.; Alexander, L. E. *X-ray Diffraction Procedures for Polycrystalline and Amorphous Materials;* Wiley: New York, 1974.

[66] Shih, M. *Synchrotron x-ray studies of monolayers at air-water interface and on solid substrates* PhD thesis, Northwestern University, **1992**.

[67] Adam, N.; Miller, J. *Proc. R. Soc. A* **1933**, page 401.

[68] Betts, J.; Pethica, B. *Trans. Faraday. Soc.* **1956**, *52*, 1581.

[69] Jacquemain, D.; Grayer, S. W.; Leveiller, F.; Lahav, M.; Leiserowitz, L.; Deutsch, M.; Kjaer, K.; Als-Nielsen, J. *J. Am. Chem. Soc.* **1990**, *112*, 7724.

[70] Helm, C.; Laxhuber, L.; Lösche, M.; Möhwald, H. *Coll. Polym. Sci.* **1986**, *264*, 46.

[71] Small, D. *The Physical Chemistry of Lipids, Handbook of Lipid Research*, Vol. 4; Plenum Press: New York, 1986.

[72] Mantsch, H.; Weng, S.; Yang, P.; Eysel, H. *Mol. Struct.* **1994**, *324*, 133.

[73] Kaganer, V.; Loginov, E. *Phys. Rev. E* **1995**, *51*, 2237.

[74] Unger, G. *J. Phys. Chem.* **1983**, *87*, 689.

[75] Koryta, J.; Dvorák, J.; Kavan, J. *Principles of Electrochemistry;* Wiley: New York, 1993.

[76] Lynch, M.; Pan, Y.; Laughlin, R. *J. Phys. Chem.* **1996**, *100*, 357.

[77] Piper, S. *J. Chem. Soc.* **1929**, page 234.

[78] Vineyard, G. *Phys. Rev. B* **1982**, *8*, 4146.

[79] Durbin, M.; Malik, A.; Richter, A.; Ghaskadvi, R.; Gog, T.; Dutta, P. *J. Chem. Phys.* **1997**, *106*, 8216.

[80] Petrov, J.; Kuleff, I.; Platikanov, D. *J. Coll. Interface Sci.* **1982**, *88*, 29.

[81] Baes, C.; Mesmer, R. *The Hydrolysis of Cations;* Wiley: New York, 1976.

[82] Barton, S.; Thomas, B.; Flom, E.; Rice, S.; Lin, B.; Peng, J.; Ketteron, J.; Dutta, P. *J. Chem. Phys.* **1988**, *89*, 2257–2270.

[83] Pauling, L. *The Nature of the Chemical Bond;* Cornell UP: New York, 1960.

[84] Viswanathan, R.; Madsen, L.; Zasadzinskin, J.; Schwartz, D. *J. Coll. Interface Sci.* **1995**, *269*, 51.

[85] Leveiller, F.; Jacquemain, D.; Lahav, M.; Leiserowitz, L.; Deutsch, M.; Kjaer, K.; Als-Nielsen, J. *Science* **1991**, *252*, 1532.

[86] Kissel, L. *Radiat. Phys. Chem.* **2000**, *59*, 185.

[87] Majewski, J.; Kuhl, T.; Kjaer, K.; Gerstenberg, M.; Als-Nielsen, J.; Israelachvili, J.; Smith, G. *J. Am. Chem. Soc.* **1998**, *120*, 1469.

[88] Richens, D. *The chemistry of aqua ions;* Wiley: New York, 1997.

[89] Weissbuch, I.; Baxter, P.; Kuzmenko, I.; Cohen, H.; Cohen, S.; Kjaer, K.; Howes, P.; Als-Nielsen, J.; Lehn, J.; Leiserowitz, L.; Lahav, M. *Chem.-Eur. J.* **2000**, *6*, 725.

[90] James, A.; Lord, M. *Macmillan's Chemical and Physical Data;* Macmillan: London, 1992.

[91] Yazdanian, M.; Yu, H.; Zografi, G.; Kim, M. *Langmuir* **1992**, *8*, 630.

[92] Schwartz, D.; Viswanathan, R.; Garnaes, J.; Zasadzinski, J. *J. Am. Chem. Soc.* **1993**, *115*, 7374.

[93] Datta, A.; Kmetko, J.; Yu, C.-J.; Richter, A.; Chung, K.; Bai, J.; Dutta, P. *J. Phys. Chem. B* **2000**, *104*, 5797.

[94] Fradin, C.; Braslau, A.; Luzet, D.; Alba, M.; Gourier, C.; Daillant, J.; Grübel, G.; Vignaud, G.; Legrand, J.; Lal, J.; Petit, J.; Rietord, F. *Physica B* **1998**, *248*, 310.

[95] Garnaes, J.; Schwartz, D.; Viswanathan, R.; Zasadzinski, J. *Nature* **1992**, *357*, 54.

[96] Schwartz, D.; Viswanathan, R.; Zasadzinski, J. *J. Chem. Phys.* **1994**, *101*, 7161.

[97] Frostman, L. M.; Ward, M. D. *Langmuir* **1997**, *13*, 330–337.

[98] Chernov, A. A. *Modern Crystallography III: Crystal Growth*, Vol. 36 of *Solid-State Sciences;* Springer-Verlag: New York, 1980.

[99] Bochner, R.; Abdul-Rahman, A.; Nancollas, G. *J. Chem. Soc., Faraday Trans. 1* **1984**, *80*, 217–224.

[100] Barone, J.; Svrjcek, D.; Nancollas, G. *J. of Cryst. Growth* **1983**, *62*, 27–33.